2023

Targeting EZH2 to Improve Outcomes of Lung Squamous Cell Carcinoma

Tanner DuCote
University of Kentucky, tannerjducote@uky.edu
Digital Object Identifier: https://doi.org/10.13023/etd.2023.399

STUDENT AGREEMENT:

I represent that my thesis or dissertation and abstract are my original work. Proper attribution has been given to all outside sources. I understand that I am solely responsible for obtaining any needed copyright permissions. I have obtained needed written permission statement(s) from the owner(s) of each third-party copyrighted matter to be included in my work, allowing electronic distribution (if such use is not permitted by the fair use doctrine) which will be submitted to UKnowledge as Additional File.

I hereby grant to The University of Kentucky and its agents the irrevocable, non-exclusive, and royalty-free license to archive and make accessible my work in whole or in part in all forms of media, now or hereafter known. I agree that the document mentioned above may be made available immediately for worldwide access unless an embargo applies.

I retain all other ownership rights to the copyright of my work. I also retain the right to use in future works (such as articles or books) all or part of my work. I understand that I am free to register the copyright to my work.

REVIEW, APPROVAL AND ACCEPTANCE

The document mentioned above has been reviewed and accepted by the student's advisor, on behalf of the advisory committee, and by the Director of Graduate Studies (DGS), on behalf of the program; we verify that this is the final, approved version of the student's thesis including all changes required by the advisory committee. The undersigned agree to abide by the statements above.

Tanner DuCote, Student

Christine Brainson, Major Professor

Isabel Mellon, Director of Graduate Studies

Targeting EZH2 to Improve Outcomes for Lung Squamous Cell Carcinoma

---

DISSERTATION

A dissertation submitted in partial fulfillment of the
requirements for the degree of Doctor of Philosophy in the
College of Medicine
at the University of Kentucky

By

Tanner J. DuCote
Lexington, Kentucky

Co- Directors: Dr. Christine Fillmore Brainson, Assistant Professor of Toxicology and Cancer Biology

and Dr. Jill Kolesar, Professor of Pharmacy Lexington, Kentucky

2023

ABSTRACT OF DISSERTATION

Targeting EZH2 to Improve Outcomes for Lung Squamous Cell Carcinoma

Only 20% of patients diagnosed with lung squamous cell carcinoma (LSCC) respond to immunotherapy. Anti-PD1 immunotherapy is most commonly prescribed to these patients; however, most will become refractory. It is important to understand the mechanisms underlying this problem to increase durability and survival. Building upon the work of other groups, our lab has demonstrated that the inhibition of the histone methyltransferase, EZH2, is crucial to maintaining an immunologically responsive microenvironment. Based on our data, we hypothesize that combining EZH2 inhibitors with anti-PD1 therapy will increase response and durability.

To study non-small cell lung cancers (NSLC) our lab uses a variety of 2D and 3D *in vitro* models derived from mouse and human tissues. The experiments performed combine interferon-γ (IFNγ) with pharmacological EZH2 inhibitors to determine the combinatorial effects on gene expression of major histocompatibility complex I and II (MHC I/II). Following treatment, assays such as qPCR and flow cytometry were performed, which revealed an increase in both gene and protein expression of MHC I and II. Expression of MHC I and II is critical to antigen presentation and T cell activation; therefore, it is important to study in the context of immunotherapy. Moreover, it has been demonstrated by other groups that high EZH2 expression correlates to a decrease in MHC I and II expression in different models of cancer, and that expression of MHC II predicted response to immunotherapy by increasing progression free survival.

Additionally, two *in vivo* models of LSCC were used to define the effects of combining an EZH2 inhibitor with anti-PD1 immunotherapy. The mouse models employed in our studies are generated through the biallelic deletion of the two tumor suppressors *Lkb1* and *Pten* (LP) in an autochthonous manner or through a syngeneic subcutaneous graft. Both models recapitulate the histology seen in human disease as evidenced by the presence of large pockets of infiltrating neutrophils. These tumor-associated neutrophils (TANs) demonstrate immunosuppressive effects on the microenvironment within the tumor milieu through the production of enzymes and immune modulating cytokines that are detrimental to T cell activation.

Following positive identification of tumor burden by MRI or palpation, the mice are placed on treatment regimen that combines anti-PD1 immunotherapy with EZH2 inhibitors. Upon subsequent MRI analysis and tumor volume calculation, we determined that the combination therapy was superior to each single agent in the autochthonous model. Furthermore, we observed that the drug EPZ-6438 contains anti-cancer activity as a single agent in the syngeneic graft model. This finding is exciting as a therapeutic option for patients who are not eligible for immunotherapy or in the case of a patient having severe adverse reactions to immunotherapy. Lastly, we performed scRNAseq on tumors from our in vivo study and identified increases in gene sets involved with IFNγ signaling and immune activation. We also identified different populations of neutrophil within tumors, demonstrated by increases of tumor eliminating phenotypes and decreases in tumor promoting populations.

Keywords: EZH2, epigenetics, immunotherapy, lung cancer

Tanner Jude DuCote

(Name of Student)

06/6/2023

Date

Targeting EZH2 to Improve Outcomes of Lung Squamous Cell Carcinomas

By
Tanner DuCote

Dr. Christine F. Brainson
Co-Director of Dissertation

Dr. Jill Kolesar
Co-Director of Dissertation

Dr. Isabel Mellon
Director of Graduate Studies

06/6/2023
Date

DEDICATION

To my Aunt Jenny

ACKNOWLEDGMENTS

We all know that getting through a PhD is not possible without the help of so many others. I would first like to thank Dr. Brainson for being an amazing mentor. Dr. Brainson is one the most amazing scientists I've ever had the pleasure of meeting. Her attention to detail, her rigor, and her passion have made me not only a better scientist, but also a better person. I would also like to thank my committee members Drs. Bondada, Gao, and Kolesar for their support and guidance throughout this entire process.

I would also like to thank my current lab members Daniel, Kassie, Christian, Dave, Avery, and Erika for giving me lots to laugh about as well as roll my eyes at. Kassie, may your gears always be ground. Avery, I hope that you will never run out of Wordles, Deluxe Waffles, and Semantles. Dave, may the mobsters forever be on your side. Christian, I wish you endless amounts of grass and Frank's Red hot sauce. You all have made my final year in graduate school somewhat bearable. I would also like to thank the G.O.A.T, Xiulong Song (said in basketball announcer voice), for being the one of the most helpful people I ever have had the pleasure of working with. Thanks for your long hours in Xiulong Land helping me with my experiments, and I hope that you will be able to make your very own moon landing someday! Additionally, I would like to thank previous members of the lab Aria, Fan, Abby, Yanming, and Alex for your friendship and fun times. To all of the friends that I have made in grad school, thank you for your friendship throughout the years. There are way too many of you to list without writing another dissertation.

I would also like to thank my family and friends back home in Louisiana, I couldn't have done this without you. To my parents, I would like to thank you both for being the most supportive parents in the world. I could not have gotten this far without your loving support. I would also like to thank my sisters for their constant encouragement and believing in me. Lastly, I would like to thank Jared for leaving Louisiana and moving to

Kentucky with me without question. You have been absolutely the most supportive partner in all of this, and you will never know how much it all has meant to me.

TABLE OF CONTENTS

LIST OF FIGURES

CHAPTER 1. INTRODUCTION

1.1 Lung Cancer Subtypes and Models

Lung cancer is the leading cause of cancer related death every year worldwide and even more so in Kentucky [1]. Kentucky leads the nation in lung cancer death at 66.1%, which is likely because the state also leads the nation in individuals that smoke (28%) [2]. Other factors that contribute to this are exposure to radon and arsenic contaminated drinking water due to eastern Kentucky's reliance on coal mining and private water wells [3-5]. Lung cancer can be categorized as small cell lung cancer, which presents as an aggressive type of neuroendocrine tumor or NSCLC which is described as tumor that arise from the lung epithelium such as bronchi and alveoli [6, 7]. Moreover, we can further divide NSCLC into two main subtypes of NSCLC termed adenocarcinoma and squamous cell carcinoma. There are distinct cellular phenotypes, markers, genetics, and epigenetics of these lung cancer subtypes, which we will describe below.

The most common NSCLC subtype is adenocarcinoma, which accounts for about 45% of all NSCLC diagnoses [2]. Lung adenocarcinomas (LUAD) resemble the glandular or acinar architecture of the distal lung. Markers for LUAD include TTF1, KRT7 and SPC, which are proteins expressed by alveolar type 2 cells (AT2) cells of the adult distal lung [8]. Whole exome sequencing has shown that major alterations driving LUAD are *KRAS*, *EGFR*, *p53*, *KEAP1*, and *STK11* [8]. Targeting therapies include small molecule inhibitors that target activating mutations in tyrosine kinases, other protein kinases, and GTPases.

Lung squamous cell carcinoma (LUSCC) is the second most common subtype of NSCLC which comprises about 18% of all cases diagnosed [2]. However, in Kentucky this subtype occurs more frequently, accounting for about 31% of all cases of NSCLC diagnoses due to factors previously mentioned [2]. Histology of LUSCC includes cells that organized into a fully stratified epithelium. Additionally, a feature of these tumors is the

production of keratin pearls, which are depositions of keratins in concentric circles around abnormal squamous tissue. Markers for LUSCC include SOX2, p63, and KRT5 [8]. Unlike LUAD, which is usually driven by alterations in oncogenes, LUSCC is usually driven by the loss of tumor suppressor genes, *PTEN*, *CDKN2A*, and *STK11* (*LKB1*) making them less targetable for small molecule inhibitors.

Cancer is a disease driven by genetic mutations, which tend to converge on shared pathways within cancer subtypes. Oncogenes generally drive tumorigenesis through the constitutive activation of specific proteins, most often kinases. These kinases phosphorylate proteins which then become activated and signal for the out of control cell growth and division. Oncogenes commonly found mutated in NSCLC are *EGFR*, *KRAS*, *PIK3CA,* which we now have small molecule inhibitors for to use therapeutically [9-12]. Moreover, there are tumor suppressor genes that generally maintain homeostasis within the cells. Tumor suppressor genes control signaling that generally make up checkpoints that limit a cell's ability to grow and divide should something go wrong. Additionally, when these systems are compromised through inactivating mutations, these checkpoints no longer exist. Furthermore, the cell will continue to grow and divide without regulation and can contribute to further alterations. Tumor suppressor mutations commonly mutated in NSCLC are *p53*, *PTEN*, and *CDKN2A* [13].

To study lung cancer *in vivo* we use genetically engineered mice to recapitulate diseases found in humans. Genetically engineered mouse models that we use for these studies are generated using the Cre-lox system. Cre recombinase is a nuclease that recognizes sites on DNA called loxP sites flanking a specific site [14]. Once Cre recognizes a loxP site, it is then excised from the DNA generating a knock-out of your gene of interest. For our models we use a Cre recombinase encoded within an adenovirus as a vector for delivery abbreviated as AdCre [15]. Using this technique allows us to either

activate mutations through the deletion of stop cassettes or delete the gene of interest altogether.

To study LUAD, there are many models to choose from. Given that KRAS and EGFR are commonly mutated oncogenes, mouse models have been designed by creating activating mutations seen from genomic profiling. Moreover, due to p53 being inactivated in many cases, deletions of p53 have been incorporated into many of these models. In this study we used mice with alterations in $KRAS^{G12D}$*/p53-null* combined with other mutations such as $KRAS^{G12D}$*/Lkb1-null* [16, 17]. In addition to models with alterations in KRAS, LUAD mouse models have been developed with alterations in $EGFR^{T790M/L858R}$ and $PIK3CA^{E545K}$*/p53-null* [18, 19].

To study LUSCC in a laboratory setting, many different mouse models of lung cancer have been developed. Given that LUSCC is mainly driven by the inactivation of many tumor suppressors, models have been designed through the deletion of certain alleles. Models have been designed by deleting genes such as PTEN and CDKN2A. Additionally, Sox2 is known to be upregulated in many LUSCC tumors; therefore, amplification of Sox2 has been incorporated into mouse models. Furthermore, deletion of Lkb1 in KRAS driven lung cancer was shown to switch from LUAD to LUSCC [16]. Therefore, a model was designed through the ablation of both alleles of *Lkb1* and *Pten*, generating LUSCC tumors [20]. Another model, developed by Mollaoglu et al., was designed by creating alterations in the *Sox2*, *Nkx2-1*, and *Lkb1* (SNL) [21]. Lastly, another model was created with alterations in *Cdkn2a*, *Sox2*, and *Pten*, (Sox2PC) [22]. These models resemble LUSCC tumors that are seen clinically; therefore, these models allow us to test different treatment modalities to potentially use in the clinic.

1.2 Polycomb Repressive Complex 2 and Lung Cancer

The topological organization of DNA within the nucleus dictates which regions will be open for transcription. This concept is known as epigenetics. For cells to function properly and maintain their transcriptional programming epigenetic maintenance is essential for the cell. One of the ways this programming is maintained is through a group of proteins known as the Polycomb Repressive Complex 2 (PRC2). The members of PRC2 include EED, SUZ12, and the catalytic subunit EZH2 [23]. EZH2 is a histone methyltransferase that binds to regulatory regions of DNA to repress genes [23]. The catalytic mark of this process is tri-methylation of histone three at lysine 27 (H3K27me3) [23]. The methylation process occurs through the donation of methyl groups of S-adenosyl methionine (SAM) in the SET domain of EZH2 to specific lysines in histones. This methylation condenses the chromatin structure and leads to the silencing of genes [23].

EZH2 has demonstrated both an oncogenic role as well as the ability to act as a tumor suppressor in different contexts. In KRAS driven adenocarcinoma, PRC2 has been shown to act in an oncogenic manner [24]. This was showing that deletion of EED in a model of LUAD with activated KRAS, led to slower development of tumors. Additionally, Zhang et al. showed that in LUAD with high EZH2 expression, treatment with EZH2 inhibitors could decrease tumor volume. Furthermore, EZH2 has been known to be oncogenic when activating mutations occur in diffuse B cell lymphoma with higher expression leading to poorer prognosis [25, 26]. Conversely, when p53 is deleted in tandem with PRC2 inactivation through the deletion of EED, PRC2 acts as a tumor suppressor and delays tumor growth [27]. Interestingly, Chen et al. showed that LUAD had higher expression of EZH2 but lower H3K27me3 compared to LUSCC [28]. Similarly, in LUSCC tumors I saw an overall higher expression of EZH2, but lower H3K27me3 when compared to LUAD [Fan's paper]. Although this correlation is the opposite of what would

be expected, this phenomenon is observed in both human and mouse models of LUSCC [19].

In addition to LUAD and LUSCC being subtypes of NSCLC, a third type of tumor that contains a mixed lineage can arise called adenosquamous carcinoma (ADSCC). Usually, LUAD arise from AT2 and club cells, a switch has been identified through the loss of Lkb1 [16]. This switch allows cells expressing markers of both basal and alveolar cells. Being that the cells are of the same genetic background, the likely mechanism of this heterogeneity is through epigenetics. This has been identified in a stepwise $KRAS^{G12D}$/*Lkb1-null* mouse model of ADSCC [16]. Moreover, Zhang and Fillmore et al. found that loss of PRC2 concurrently happened during the transition from LUAD to LUSCC due to the de-repression of genes controlling a squamous fate [29]. Furthermore, the authors discovered that cells such as club cells and bronchioalveolar stem cells (BASCs) are cells that generally give rise to LUAD but appear poised to switch lineages easily [29].

1.3 Tumor Microenvironment

Tumors of all types are not just comprised of malignant epithelial cells, but instead are very heterogeneous entities [30]. Non-immune cells within the tumor microenvironment (TME) consist of endothelial cells, necessary for angiogenesis due to an increase in VEGF production, and for the delivery of oxygen and nutrients, as well as mesenchymal cells which can also be referred to as cancer associated fibroblasts (CAFs) [30]. CAFs permit the tumor to progress by expressing cytokines and other molecules that can lead to epithelial to mesenchymal transition [31]. This process can eventually lead to anoikis, allowing the tumor cells to extravasate into circulation and spread to distant sites for metastasis. Moreover, immune cells are also frequently seen within the TME [32]. Cells

such as macrophages, neutrophils, dendritic cells, and T cells can behave in ways that either promote tumor growth or conversely, tumor eliminating phenotypes [8, 32].

The immune system can be divided into two main groups: the innate compartment, and the adaptive compartment. The innate compartment, which is comprised in a large part cells of myeloid lineage that respond immediately to an infection and tissue injury and are less specific. This group consists of cells such as macrophages, neutrophils, and dendritic cells which can all perform antigen presentation to activate cells of the lymphoid compartment [33]. Moreover, the lymphoid compartment is comprised of cells that need to be recruited and stimulated to become activated making this a very specific response. Cells that comprise the lymphoid compartment include T cells and B cells which can be further divided into multiple subsets.

Neutrophils are polymorphonuclear cells derived from a common myeloid progenitor [34]. These innate immune cells are known as the first responders and contain granules that contain cytolytic compounds that are excreted to kill pathogens [34]. These cytolytic compounds also can damage surrounding healthy tissues, as these compounds are non-specific. Neutrophils are also very oxidative in nature due to the production of myeloperoxidase, and superoxide to kill pathogens [35]. Additionally, neutrophils produce molecules that promote tumor growth and development through the production of matrix metalloproteinase 9 [36, 37]. Neutrophils have different stages of maturation which can determine how they function in the TME [38].

Another innate immune cell population within tumor stroma is macrophages. Macrophages are cells derived from myeloid progenitor cells and can be circulating or tissue resident [39]. These cells are phagocytic and are responsible for cleaning up dead or damaged tissue and most importantly antigen presentation [37]. Additionally, dendritic cells are located within the TME and present antigens for immune surveillance and

destruction of malignant epithelial cells. Dendritic cells are the main antigen presenting immune cell and highly express major histocompatibility complex II (MHC II) [37, 40]. Moreover, dendritic cells surveil the TME through a process called micropinocytosis [41].

Macrophages and neutrophils can be split into two main phenotypic populations, macrophages and neutrophils that promote the elimination of the tumor through the production of pro-inflammatory cytokines and chemokines such as TNF-α [42, 43]. On the contrary, there are also populations of macrophages and neutrophils that promote the growth of tumors. These cells produce immunosuppressive cytokines and chemokines such as TGF-β as well as enzymes like arginase, which depletes arginine that essential for T cell activation [42, 44]. Furthermore, an important job of cells within the TME to recruit more immune cells through the production of chemokines [45]. Some chemokines attract tumor eliminating immune cells and their production can be modulated epigenetically [45, 46]. Due to immune cell function and the heterogeneity of TME among different tumors, it would be naïve to think that there are only two classes of these neutrophils. It is likely that these immune cells fall on a spectrum of phenotypes and that their function is likely contextual to each individual TME. Moreover, it has recently been shown that as many as five and six classes of neutrophils and five classes of macrophages that are phenotypically distinct from one another [47, 48].

Another type of immune cell involved in tumor promotion or clearance are T cells. T cells are members of the lymphoid compartment of the immune system described as adaptive immunity. T cells can be classified as CD4+ and CD8+, which determines their activity. The job of CD4+ T cells is to activate other immune cells to assist in immune response, whereas CD8+ T cells function to directly kill cells it deems pathogenic [49]. These tumor-eliminating T cells are recruited to the TME by the production of the chemokines CXCL9/10/11 [45]. CD4+ T cells can be further divided into helper and

effector T cells, as well as an immunosuppressive FOXP3+ T regulatory cells (Tregs) [50, 51]. In addition to T cells, another type of cell located within the TME which is also a member of the adaptive immune system are plasma cells. Plasma cells are differentiated B cells that secrete antibodies and have also been demonstrated to predict poor prognosis when present in the TME [52].

MHC antigens are part of the antigen presentation machinery used to inform T cells what targets to look for. MHC molecules interact with the T cell receptor (TCR) and co-stimulation occurs with CD4, CD8, as well as B7 and CD28 [53]. There are two types of MHC molecules, there are class one molecules which present endogenous antigens to CD8+ T cells [54]. This is likely from a virus infected cell or cancer cells that are expressing tumor specific antigens. MHC class I molecules are expressed on almost all nucleated cells within the body; however, some tumors can downregulate their expression to evade immune surveillance [54]. MHC I is a heterodimer of an alpha chain and β2 microglobulin which creates a cleft where antigen derived peptides are loaded within the endoplasmic reticulum [54].

MHC class two molecules present exogenous antigens likely picked up from the phagocytic or pinocytic process to CD4+ T cells [54]. MHC II expression is much more limited and is generally restricted to antigen presenting cells such as dendritic cells, macrophages, neutrophils, and B cells [54]. MHC II can, however, also be expressed in some normal cell lineages such as a subpopulation of alveolar type II (AT2) cells and other lung epithelial cells [55, 56]. MHC II is a heterodimer made of an alpha chain and a beta chain which also contains a peptide binding cleft where antigenic peptides derived from the phagolysosome are loaded in the endosome [54]. Due to the antigen presentation function of these molecules, it can be hypothesized that these proteins may also be important in the recognition and ultimate elimination of tumors within an individual.

There are many genes that contribute to the expression of both MHC I and II genes [57]. MHC genes are the most polymorphic genes within our genomes and contain many alleles that contribute to a great diversity from person to person [58]. This polymorphism and having multiple alleles is important in self antigen recognition and T cell education [58]. The genes responsible for MHC I expression include *HLA-A, HLA-B*, and *HLA-C*, as well as *B2M* [57]. Moreover, there are other proteins that assist in peptide loading such as TAP, calnexin and calreticulin [54]. For MHC II, the genes that encode these proteins are *HLA-DR, HLA-DP*, and *HLA-DQ* [57]. Before antigen derived peptides can be loaded into the cleft of MHC II a peptide called CLIP derived from the invariant chain must be removed. This process is catalyzed by the protein HLA-DM which binds to HLA-DR, DP, or DQ and opens up the binging cleft releasing CLIP [54].

It has been observed that in both the LP and SNL models the predominant innate immune cells present within the TME are neutrophils, which recapitulates what I saw in tissue taken from patients with this disease [59-61]. Furthermore, these tumor-associated neutrophils (TANs) have been identified to have a negative correlation with infiltrating CD8+ T cells [61]. This phenomenon leads us to propose that these TANs are suppressing tumor elimination by decreasing the numbers of cytotoxic lymphocytes. Lastly, another phenomenon involving neutrophils and lymphocytes is their ratio (NLR) circulating in the blood. It has been determined that a high NLR is predictor of poorer prognosis than patients with a low NLR in a variety of types of cancer [62].

It has been reported that tumors positive for MHC II expression demonstrate a more durable response to the anti-PD1 ICI in patients with melanoma [63]. Furthermore, it can be hypothesized that upregulation in MHC I as well as MHC II could promote tumor elimination through the increased ability of CD8+ T cells to recognize peptides being displayed on the surface of malignant epithelial cells, targeting them for degradation [54].

In addition, once a CD8+ T cells becomes activated it begins to secrete IFNγ [49]. IFNγ is a canonical activator of MHC molecules, as well as other immune related proteins such as PD-L1 [64]. Given that MHC I is expressed on virtually every nucleated cell in the body, this suggests that MHC I is already poised for expression [54]. Other groups have identified the role of EZH2 in maintenance of MHC I and II expression in different models of cancer [25, 65]. Given that EZH2 controls expression of both MHC I and II, and the presence of IFNγ in an activated TME, this could allow for a target of therapeutic inhibition that could promote the expression of these two important molecules (Figure 1.1).

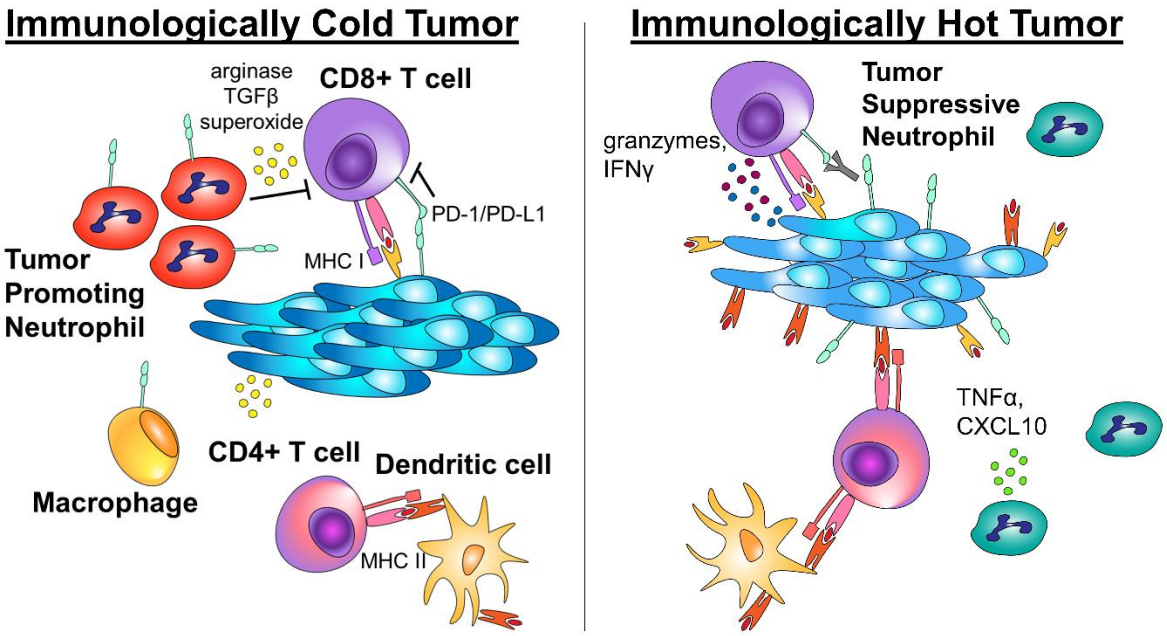

Figure 1.1 Schematic of Immunologically Hot and Cold Tumors
Immunologically cold tumors inhibit T cell activation through expression of PD-L1, arginase expression and high levels of oxidative stress, while in contrast immunologically hot tumors allow for T cell recruitment, activation and tumor elimination.

1.4 Immunotherapy

Once T cells become activated, they begin to upregulate the expression of immune checkpoint molecules such as PD-1 and CTLA-4 [66, 67]. The PD-1/PD-L1 axis works to regulate T cell activation by ramping down their activity which can cause T cell exhaustion [66, 67]. This particular pathway can be exploited clinically by creating antibodies that bind to these proteins and inhibit PD-1 from binding to PD-L1, thereby allowing T cells to become activated once again. These drugs are known as immune checkpoint inhibitors (ICI) are designed to target CTLA-4, PD-1 as well as PD-L1 [66]. After the CHECKMATE 017 clinical trial revealed that ICI were superior to docetaxel chemotherapy alone, ICI were approved by the FDA to treat LUSCC and have been used widely throughout the clinic [68]. Furthermore, these drugs have now been approved to be used in the first line setting for late-stage NSCLC. The efficacy of these drugs varies from patient to patient, and while ICI work well, unfortunately, the objective response rate is rather poor [69]. Clinically, PD-L1 expression is generally used as a prognostic indicator, where higher expression leads to better performance with anti-PD1 and anti-PD-L1 therapies. Aguilar et al. showed that the response rate in patients whose tumors have 90-100% PD-L1 positivity was about 60%, whereas patient response rates with PD-L1 positivity between 60-89% was decreased by almost half [70].

Additionally, tumor mutation burden (TMB) and microsatellite instability (MSI) also correlated with overall better response rates with ICI treatment [71]. One reasoning behind higher TMB and MSI predicting response is likely due to the production of tumor associated neoantigens [72]. Neoantigens arise due to the changes in amino acid sequence because of numerous alterations in the tumor genome [72]. These antigens are specific to the tumor and can allow for the immune system to see these proteins as foreign, targeting them for destruction. Although there is great progress in therapeutic options for

patients suffering with NSCLC, there still are important advances to be made to increase the response rate and durability of ICI. Moving forward, to increase patient durability and response rate, it is now widely thought that it is going to be combinations of therapies to target a patient's tumor. Currently, chemotherapy is being combined with ICI for NSCLC patients. It was observed that in a clinical trial that combining ICI and chemotherapy resulted in longer progression free survival than with ICI alone [73].

1.5 Immunotherapy Combined with Epi-drugs

Epidrugs are an exciting new class of drugs that target epigenetic machinery. This would allow us to target gene expression without having a drug to target a specific genetic alteration. EZH2 is a histone methyltransferase and is the catalytic component of the Polycomb Repressive Complex 2 (PRC2) which methylates histone 3 at lysine 27 (H3K27me3) [23]. This mark causes the chromatin to be more compacted, thereby repressing transcription of the genes located in these regions of DNA. Other groups have identified that EZH2 may play an important role in the maintenance of immune cell phenotypes. One group has identified that EZH2 plays a role in the expression of FoxP3, which is a transcription factor essential to the function Tregs [74, 75]. DuPage et al., showed that the ablation of EZH2 in Tregs results in dysfunction of this particular immune cell through FoxP3 downregulation [74, 75]. This suggests that EZH2 inhibition could be a likely way of diminishing these immunosuppressive cells from functioning properly in the TME [75]. Moreover, this would allow for the activation of CD8+ T cells, allowing these cytotoxic cells to infiltrate the TME and destroy malignant epithelial cells [75].

Furthermore, the Sharma group identified that EZH2 inhibition could synergize with anti-CTLA-4 ICI in a model of urothelial carcinoma [76]. With inhibition of EZH2 in combination with anti-CTLA4, they found higher percentages of infiltrating CD8+ IFNγ+ T

cells, as well as an increase in Granzyme B+ and TNF-α+ CD8+ T cells [76]. In addition to this finding, they also observed a decrease in FoxP3+ T cells [76]. Similarly to ICI, EZH2 inhibition can also be exploited in the clinic. In January of 2020 the FDA approved the EZH2 inhibitor tazemetostat for relapsed or refractory follicular lymphoma [77]. More excitingly, this drug is being combined with the anti-PD1 ICI pembrolizumab in clinical trials for urothelial carcinoma and patient accrual remains active. Taken together, with these data, EZH2 inhibitors combined with anti-PD1 ICI, could be a viable therapeutic strategy going forward for LUSCC.

Given all of this, I hypothesized that inhibition of EZH2 could boost anti-PD1 immunotherapy response in squamous lung cancer through the de-repression of antigen presentation machinery. To test this hypothesis, I performed a variety of *in vitro* and *in vivo* studies to determine that EZH2 inhibitors allow for an up-regulation in multiple genes that are important in the expression of MHC class I and II. For the in vitro studies, I used both 2D and 3D murine and human cell lines of NSCLC.

CHAPTER 2. MATERIALS AND METHODS

2.1 Mouse Models

Mouse models were: KRASG12D/p53-null lung adenocarcinoma [78], KRASG12D/p53-null/Ezh2-heterozygous and KRASG12D/p53-null/Ezh2-null lung adenocarcinoma [79], PIK3CAE545K/p53-null lung adenocarcinoma [18], EGFRT790M/L858R lung adenocarcinoma [19], KRASG12D/Lkb1-null mixed lineage tumors [80, 81] and Lkb1-null/Pten-null squamous cell carcinoma [60]. Adult mice were allowed to inhale Cre- or FlpO-encoding virus to initiate autochthonous lung tumors. Experimental animals are inoculated with 2.9-5 x 10^7 PFU adeno-CMV-Cre (University of Iowa). Historical banked tissues from previous studies were also used.

Tumor burden was measured via magnetic resonance imaging (MRI) 40 weeks post infection. Once tumors were detected, animals were randomized and placed onto one of four treatment arms. To inhibit EZH2, we used two potent pharmacological inhibitors GSK126 and EPZ6438. GSK126 was formulated by adding solid GSK126 (MedChem Express/Xcess Bio) to Captisol®, chopped very finely, then added to sterile saline pH 4.6, and the solution was sonicated. Anti-PD1 clone RMP1-14 (BioXCell #BP0146 or #BE0146) and IgG2a isotype control (BioXCell #BP0089) were diluted with InVivoPure pH 7.0 dilution buffer (BioXCell #IP0070) or InVivoPure pH 6.5 dilution buffer (BioXCell # IP0065) to a concentration of 1.25 µg/µL. Animals were administered GSK126 at 300mg/kg i.p. twice per week, 5-7mg/kg anti-mouse PD1 i.p. immunotherapy three times per week, or a combination of both GSK126 and anti-PD1. Placebos used for treatment arms were Captisol® in sterile saline and rat IgG2a isotype antibody. Treatment regimen was 4-6 weeks and animals were monitored for tumor burden every two weeks via MRI. To prepare formulation of the EZH2 inhibitor EPZ6438 (MedChem Express #HY-13803/CS-1758), EPZ6438 was added to a solution of 0.1% Tween 80 and 0.5% sodium

carboxymethylcelluose and the solution was sonicated. EPZ6438 was administered 250mg/kg by gavage twice daily for 14 days. All experiments were approved by the Dana-Farber Cancer Institute for our collaborators or University of Kentucky Institutional Animal Care and Use Committees (IACUCs).

2.2 Patient Samples

Patient tissue was obtained from the Markey Cancer Center Biospecimens Procurement and Translational Pathology Shared Resource Facility (BPTP SRF). A tissue microarray was prepared from patient biopsies from de-identified excess tissue. The array consists of three core biopsies from each patient, and there are a total of 83 adenocarcinoma, 102 squamous cell carcinoma, 14 adenosquamous and mixed histology tumors and 17 poorly differentiated tumors, including 2 large cell carcinoma, 1 giant cell carcinoma, 1 pleomorphic carcinoma, and 1 sarcomatoid carcinoma.

2.3 Histology and Immunohistochemistry

All tissues were fixed with 10% neutral-buffered formalin overnight. They were then transferred to ethanol, embedded in paraffin, and sectioned at 4μm. CD3 immunohistochemistry was performed by the Biospecimens Procurement and Translational Pathology Shared Resource Facility at the Markey Cancer Center. Antigen Retrieval was performed in Biocare Medical decloaking chamber at 95˚C for 30 minutes with Dako Target Retrieval Solution, pH 9 (S236784-2). Endogenous peroxidase activity was quenched with Dako peroxidase block (K800021-5). Primary antibody for CD3 (Dako IR503 ready-to-use) was added and incubated at room temperature for 45 minutes. Amplification was performed with Dako Envision anti-rabbit-HRP for 30 minutes at room temperature (K4003). Detection was performed with DAB for 10 minutes (Dako K346711-2). Slides were then counterstained with Harris's hematoxylin. Slides were scanned with

the Aperio slide scanner at 40x and 6 tumor containing regions of 355mm^2 were selected and the HALO® classifier Multiplex IHC v3.0.4 was used to quantify the positively stained cells within the regions.

2.4 Histology and HALO Nuclear Phenotyper Algorithm

Mice were euthanized and lungs were fixed with 10% buffered formalin overnight, then stored in 70% ethanol. Tissues were embedded in paraffin and sectioned at the Markey Cancer Center Biospecimens Procurement and Translational Pathology Shared Resource Facility (BPTP SRF). Histology slides were scanned at 20-40x with an Aperio slide scanner and images were used for further analysis. HALO AI nuclear phenotyper algorithm was trained for 556,930 iterations using a total of 34,427 nuclei from 47 different samples. The accuracy of the final nuclear phenotyper algorithm was verified by pathologists at the Markey Cancer Center. For each murine lung sections, the tumor areas with approximately 100µm surrounding area were hand-annotated for analysis. For the KRAS/Lkb1-null tumors, adenocarcinoma and squamous cell carcinoma regions were manually sub-annotated+. To validate that the sub-cutaneous grafts contained similar cellular proportions to lung tumors, we used our previously described nuclear phenotyper shown in Figure 3.7C.

2.5 Cell lines

Cell lines were maintained according to University of Kentucky biosafety guidelines. All human cell lines were cultured in RPMI 1640 (Gibco, #11875-093), supplemented with 8% fetal bovine serum (VWR), penicillin/streptomycin (Gibco, #15140-122), and 4mM GlutaMAX™ (Gibco, #35050-061) at 37˚C and 5% CO_2. All cell lines were tested regularly for mycoplasma with MycoAlert™ PLUS Mycoplasma Detection Kit (Lonza) and prophylactic treatment with Plasmocin (InvivoGen, #ant-mpt) was used routinely. Cell lines

were verified by STR analysis with CellCheck9 by IDEXX laboratories before beginning of experiments and used within 10 passages of authentication.

2.6 Flow cytometry analysis and sorting

For all 2D flow cytometry experiments, cells were trypsinized from culture plates and incubated with antibodies at 1:100 dilution in PBS + 10% FBS (PF10) for 15 minutes at room temperature. The cells were then resuspended in 300µL of PF10 + 4',6-diamidino-2-phenylindole (DAPI) (1:250). Antibodies for human cell analysis: EpCAM-FITC (BD Biosciences, #347197), PD-L1-PE (eBiosciences, #12-5983-42), CD49f- Alexa Fluor® 647 (BD Biosciences, #562473), NGFR-PECy7 (BioLegend, #345110), CD49f-FITC (Invitrogen, #11-0495-82), HLA-DR-APCCy7 (BioLegend, #307618), and HLA-A,B,C-APC (BioLegend, #311410). Antibodies used for mouse studies: I-A/I-E-PerCP-Cy5.5 (BioLegend #107626), H-2K^{d}/H-2D^{d}-Alexa Fluor® 647 (BioLegend #114712), NGFR (Cell Signaling #8238S), anti-Rabbit-FITC (Millipore #F2765), PD-L1-PE (BioLegend #124308), Sca1-APCCy7 (BioLegend #108126), EpCAM-PECy7 (BioLegend #118216), CD49f-FITC (Invitrogen #11-0495-82). All antibodies were bound at room temperature for 10 minutes at a dilution of 1:100, with the exception of Sca1 that is used at 1:50. Syngeneic grafts were dissected, minced, dissociated with collagenase/dispase (SIGMA 10269638001, 6mg/mL) for 45 minutes at 37°C and filtered through 40µm cell strainers. Antibodies used for staining were: anti-PD1-BV421 (BioLegend #135218), anti-CD8-BV711 (BioLegend #100747), anti-CD4-BV786 (BioLegend #100552), anti-CD45-FITC (BioLegend #103108), anti-CD3-BB700 (BioLegend #100328), anti-Rat-IgG2A-PECF594 (BioLegend #405432), Ly6G-BV786 (BioLegend #127645), F4/80-PECF594 (BioLegend #123146), CD11b-PECy7 (BioLegend # 101216) with the live-dead stain Zombie UV™ (BioLegend 423107). AnnexinV staining was performed with the Biolegend AnnexinV-FITC, 7AAD kit

(#655942) on bone marrow samples (described below) according to the manufacturer's instructions.

2.7 BM histopaque gradient, Cytospin and Staining

Following euthanasia, mouse legs were removed at the acetabulum and placed into magnesium/calcium free PBS (Cytiva, #SH30256.02). The bones were cleaned and flushed into a 1.5ml tube using magnesium/calcium free PBS. The remaining cells were pelleted via pulse centrifugation then were subject to red blood cell lysis in 250µl of red blood cell lysis buffer. Following, red blood cell lysis the cells were washed with 1ml of calcium/magnesium free PBS then pelleted with pulse spin centrifugation. Cells were then plated for apoptosis at 500,000 cells in 12 well plates in DMEM/F12 media (ThermoFisher, 11330032) with an additional 4 mM Glutamax (ThermoFisher, 35050061), 5 µg/mL ITS (insulin/transferrin/selenium, SIGMA, I3146) and 8-9% fetal bovine serum (VWR, 97068-085). Remaining cells were resuspended in 1 ml of calcium/magnesium free PBS. For Histopaque gradient, in a 5mL flow cytometry tube, 1.5ml of Histopaque 1119 (SIGMA #RNBK6705) was added at room temperature and 1.5ml of Histopaque 1077 (SIGMA #RNBL3022) at room temperature was carefully pipetted on top. Samples were then added on top of the Histopaque layers slowly to persevere the interface between the layers. The tubes were then spun at 25°C at 1000x g for 25 minutes with no brake. Following centrifugation, the buffy coat was collected into a 1.5mL tube and washed with 1ml of magnesium/calcium free PBS. The cells were resuspended in 1mL of magnesium/calcium free PBS and 150uL was taken to perform cytopsin. For cytopsin, 150µL cell suspension was pipetted into funnel and slides were spun at 550 rpm for 1 minute. The areas where cells had adhered were then circled with a wax pen and 150µL of paraformaldehyde or formalin was added for 15 minutes. The fixing agent was tapped off and then 150µL of PBS with 0.1% Triton-X was added for 15 minutes. The slides were

stained using hematoxylin for 1 minute. The slides then proceed from 70% ethanol for 1 minute, 95% ethanol for 1 minute, 100% ethanol for 3 minutes, Xylene for 3 minutes, Xylene 3 minutes, and finally Xylene for 3 minutes. The slides were then allowed to dry and the cover slip was added using Cytoseal (Thermo #527665).

2.8 Western Blot

Cells were lysed with RIPA buffer (50 mM Tris, 150 mM NaCl, 0.5% Deoxycholate, 1% NP-40, 0.1% SDS, 1 mM DTT, and 1% protease/phosphatase inhibitor) and supernatant was cleared by centrifugation. Protein concentration was determined using the Pierce BCA assay kit (Thermo, 23227). Between 40mg and 120mg of each protein sample was boiled in Laemmli buffer with 10% β-Mercaptoethanol and equal percentages of each sample were run on 4-15% polyacrylamide gels (BioRad, 4561086). Resolved proteins were wet-transferred to nitrocellulose membranes (Amersham), which were then blocked in a 5% BSA (VWR, 9048-46-8) solution made in 1x TBST buffer (20 mM Tris base, 0.15 M NaCl, 0.1% Tween, adjusted to pH 7.6). Membranes were then incubated with antibody solutions prepared in 5% BSA overnight. Antibodies used were (H3K27me3 Cell Signaling C26B11 1:500, EZH2 Cell Signaling 5246S 1:200, B2M Millipore MABF1968 1:1000, HLA-DR,DQ,DP AbCAM ab7856 1:1000, Total Histone H3 AbCAM ab1791 1:5000). After washing, secondary antibodies were added (Novus anti-Rabbit-HRP and anti-Mouse-HRP), incubated, and washed. Bands were visualized with West Plus Pico ECL (Thermo) and exposed to Hyperfilm™ ECL™ film (Amersham). Protein molecular weights were determined with Precision Plus Protein™ Kaleidoscope™ Prestained Protein Standards (BioRad).

2.9 MRI of genetically engineered mouse models

Animals were anaesthetized via inhalation of isoflurane and kept warm on heated waterbed, vital signs were monitored via cardiac and respiratory cycle (SA instruments), and recorded every 10 minutes while the animal was under anesthesia. The SA instruments pneumatic respiratory monitor was used to remove breathing artifacts by gating on the respiratory cycle. The Bruker ClinScan system used to scan the animals had 12 cm of actively shielded gradients, maximum strength 630 mT/m, and a slew rate of 6300 T/m/s. This instrument is a 7T system with 2x2 array coil and 2D gradient echoT1-weighted sequences. The parameters used for imaging are as follows: 18 slices, TR = 170 ms, TE = 2.4 ms, α=38°, Navg=3, FOV 26 x 26 mm^2, 1mm thickness, matrix size 256 x 256, for a voxel size of 0.102 x 0.102 x 1.0 mm. In 2021, the system was upgraded to a Bruker Biospec system. For this upgraded machine, the Bruker IntraGate software was used to remove respiratory and cardiac motion with parameters: 18 slices, TR = 8.96ms ms, TE = 3.4 ms, α=10°, oversampling = 28, FOV 26 x 26 mm2, 1mm thickness, matrix size 192 x 192, 10 minutes. Models were then built on Slicer 3D software version 4.11.20200930 to calculate tumor volume.

2.10 Tumor Cell 3D culture

Murine tumoroids generated from tumors of our mouse models were seeded in DMEM/F12 media (ThermoFisher, 11330032) with an additional 4mM Glutamax (ThermoFisher, 35050061), 5µg/mL ITS (insulin/transferrin/selenium, SIGMA, I3146) and 8-9% fetal bovine serum (VWR, 97068-085). Tumoroids were seeded and maintained in growth factor reduced and phenol red-free Matrigel (Corning, 47743-722) in transwells with 0.4 µm pore size (Corning). Human tumoroids were seeded in DMEM/F12 media (ThermoFisher, 11330032) with an additional 4mM Glutamax (ThermoFisher, 35050061), 20ng/mL FGF7 (VWR 10771-958), 50ng/mL FGF10 (VWR 10772-106), 40ng/mL Noggin

(VWR 10772-456), 500nM A83-01 (R&D systems 2939), 5uM Y-27632 (Abmole Y-27632), 500nM SB202190 (SIGMA S7067), B27 Supplement (Gibco 1750-44), 1.25mM N-acetylcysteine (SIGMA A9165), 5mM Nicotinamide (SIGMA N0636), and penicillin/streptomycin (Invtirogen 15140-122)[82]. Tumoroid cultures were established in the presence of plasmocin (Invivogen Ant-mpt-1). Tumoroids were seeded with cells from our *Lkb1/Pten -/-* model and allowed to become established before starting treatment. Tumoroids were placed on six different treatment arms: DMSO as vehicle control, GSK126 (5μM), EPZ6438 (5μM), IFN-γ (20ng/mL), or combination of GSK126 (5μM) and IFN-γ (20ng/mL) or EPZ6438 (5μM) and IFN-γ (20ng/mL). Tumoroids were fed every two days for 11 days total, adding in IFN-γ on day nine.

2.11 ChIPseq

To perform ChIP analysis, we followed the ChIP Cell Fixation protocol provided by Active Motif. Cells were fixed by adding 1/10th volume of freshly prepared solution of 11% Formaldehyde (SIGMA #F-8775), 0.1M NaCl (Fisher Scientific #S271-10), 1mM EDTA pH 8.0 (Invitrogen #AM9261), 50mM HEPES pH 7.9 (SIGMA #H0887), diluted in H_2O to the dissociated cell in media, and incubated for 15 minutes at room temperature. The samples were then quenched by adding a 1/20th volume of 2.5M Glycine (SIGMA #G-7403). Next, the samples were washed with cold 0.5% IGEPAL® CA-630 (SIGMA #I8896) in PBS pH 7.4 and centrifuged at 800g for 10 minutes at 4˚C. The supernatant was removed and the cell pellets were washed in cold 0.5% IGEPAL®-PBS and centrifuged for another 10 minutes at 4˚C. Cells were then resuspended with 100mM PMSF in ethanol, and centrifuged once again. Supernatant was removed and pellets were snap frozen with liquid nitrogen and stored at -80˚C. These samples were sent to Active Motif for ChIP-sequencing using the antibodies H3K27me3 (Active Motif 39155, 4μL antibody per 40μg

chromatin), H3K4me3 (Active Motif 39159, 4µL antibody per 40µg chromatin) or H3K27ac (Active Motif 39133 4µL antibody per 40µg chromatin). Quality control and read alignment was performed by ActiveMotif. Briefly, the 75-bp single-end sequence reads were mapped to the human reference genome hg38 using the bwa samse with default settings. Reads that had >2 mismatches and multimapping reads were removed followed by PCR deduplication. The resulting bam files were normalized to account for the differences in the sequencing depth. Samples within each antibody group were reduced by random sampling to the number of unique alignments present in the smallest sample. Since the 5'-ends of the aligned reads represent the ends of the ChIP/IP-fragments, the tags were extended in silico using Active Motif software at their 3'-ends to a length of 200bp. To identify the density of fragments along the genome, the genome was divided into 32-nt bins and the number of fragments in each bin was determined. The MACS2 version v2.1.0 peak finding algorithm was used to identify regions of ChIP-seq enrichment over background, with p-value threshold of enrichment 1E-07 for all datasets. Genomic regions known to have low sequencing confidence were removed using blacklisted regions defined by the ENCODE project. The selected peak intervals were annotated to the nearest transcription start sites (TSS) using the KnownGene hg38 TSS annotation. To compare peak metrics, overlapping intervals were grouped into merged regions, defined by the start coordinate of the most upstream interval and the end coordinate of the most downstream interval. In locations where only one sample has an interval, this interval defines the merged region. Peak distribution patterns were obtained using seqplots across all merged intervals from −5 kb to +5 kb to include distal promoters and regulatory regions. Heatmaps were generated for visualization of tag distributions, which are mapped across target regions. The average values for all target regions in heatmaps were calculated and plotted in histograms. Peaks unique to each genotype or conserved in multiple genotypes were annotated by GREAT[83] to associate each genomic region with all genes whose

regulatory domain it overlaps. The resulting gene lists were used to identify significantly enriched gene signatures from GSEA curated signature gene sets.

2.12 Single cell RNA sequencing

Lungs were harvested from mice and dissociated by finely mincing with scissors and titurating with a 5mL serological pipette filled with Ca2+/Mg2+-free PBS. In order to enrich for immune cell populations, they were then stained with EpCAM-PECy7 (BioLegend #118216) and CD31-APC (Biolegend Cat# 102510), bound to beads and run through Miltenyi LS columns (#130-042-401) on a magnet. The flow through was collected and cells were captured for reverse transcription by a 10x Genomics Chromium controller. Reverse transcription was performed using the 10X Genomics Single Cell 3' v3 Kit. Libraries were prepared and sequenced by Beijing Genomics Institute, and the sequencer-produced Chromium single-cell data and then the Cell Ranger toolkit version 3.1 (10X Genomics) was used to de-multiplex samples from raw sequencing reads to gene-count matrices with alignment to the mm10 genome (v93). In order to perform the downstream analysis, such as cell type identification and differential gene expression analysis, Seurat (V3) R package[84] was employed to aggregate the gene-counts matrices from all samples and provide the analytical insight. A five-step process was performed using Seurat package: (1) For quality control and data pre-processing, we discarded genes expressed in fewer than three cells and discarded the low-quality cells that had less than 100 genes expressed or percentage of mitochondrial transcripts > 7. The count matrices were then log-transformed. (2) For sample merging and feature selection, we combined the log-transformed matrices of each sample and applied the variance-stabilizing transformation (vst) method to remove cell-to-cell variation. The top 1500 genes were selected for sample integration. (3) For dimension reduction and clustering, we applied "PCA" to reduce the dimensionality of the merged data to 50 principal components, and

then performed a shared nearest neighbor (SNN) modularity optimization-based algorithm to identify clusters of cells. We utilized the UMAP [85] technique to visualize the clustering results as shown in Figure 4.17A. (4) Cell cluster identities were called by examining highly expressed genes in each cell cluster (Supp Table 2). (5) For differential gene expression analysis for each cell population, we used a DEG (Differential Expressed Gene) identification method in Seurat, namely “MAST”[86], to identify the up/down-regulated sets of genes between treatment groups in the three major populations, neutrophils, macrophage/dendritic cells, and tumor cells. In the Figure 6B, the distribution of cell clusters across genotypes was assessed by z-test and p values were adjusted for multiple hypothesis testing.

2.13 RNA Isolation

To perform RNA isolation Absolutely RNA Miniprep kits were used (Agilent #400805). Cell pellets were re-suspended in lysis buffer plus 0.7% β-mercaptoethanol and stored at -80˚C. An equal volume of 70% nuclease free ethanol was added to each sample and the solution was added to a column. Columns were washed once with low-salt wash buffer once and DNase digestion was performed for 15 minutes at 37˚C. The column was then washed once with high-salt buffer, followed by two more low-salt washes. The RNA was eluted with elution buffer for 2 minutes at 55˚C and stored at -80˚C.

2.14 RT-qPCR and Sequencing

Concentration of RNA samples was quantified by NanoDrop 8000™ spectrophotometer (Thermo Fisher #ND-8000-GL). To perform cDNA synthesis, random hexamers (50ng/μL) and dNTPs (10mM) were mixed in a 1:1 ratio and 2μL was placed in each PCR tube. Next, 1000ng of RNA was added and volume was brought up to 12μL, placed in C1000 Touch™ thermal cycler (BioRad), and run for 5 minutes at 65˚C. A master

mix of reagents was made for each sample (5x reverse transcription buffer, 50mM $MgCl_2$ (Invitrogen #AM9530), 0.1M dithiothreitol, 40U/μL RNaseOUT™ (Invitrogen #100000840), 200U/μL SuperScript™ III (Invitrogen #56575). The cDNA protocol continued on thermal cycler as follows: 25˚C for 10 minutes, 50˚C for 50 minutes, 70˚C for 15 minutes. After the 70˚C step, 1μL of RNase H (Ambion #AM2293) was added to each tube and protocol continued for 20 minutes at 37˚C. After polymerization, cDNA is diluted 1:5 before performing qPCR and stored at -80˚C. To perform qPCR master mixes were made for each gene of interest using TaqMan™ Fast Advanced Master Mix (Invitrogen #4444964) and TaqMan™ qPCR Assays, then run on QuantStudio 3 (applied biosystems #A28567). Data were analyzed by calculating *Gene of Interest*($Ct_{reference}$-$Ct_{exprimental}$)-*Gapdh*($Ct_{reference}$-$Ct_{experimental}$) and the data were graphed on the log_2 scale. Library preparation and sequencing were performed by the Beijing Genomics Institute (BGI Group) using DNBseq to a depth of 24 million 100bp paired-end reads. Sequencing reads were trimmed and filtered using Trimmomatic (V0.39) [87] to remove adapters and low-quality reads. Reads from human samples were mapped to Ensembl GRCh38 transcript annotation (release 98), and mouse samples to Ensembl GRCm38 (mm10) transcript annotation (release 82), using RSEM [88]. Gene expression data normalization and differential expression analysis were performed using the R package edgeR [89].

2.15 Statistics and reproducibility

Statistical analyses were carried out using GraphPad Prism version 9 or Microsoft Excel. For murine data in Chapter 3, all tumors of a given subtype present on a slide were analyzed together. For the human data, results from three independent core biopsies were averaged. The n listed in the figures are biological replicates, which were individual mice or humans.

Unless otherwise stated, all numerical data are presented as mean ± standard error of the mean. For grouped analyses, one-way ANOVA with Holm-Šídák's multiple comparisons correction was used. A p value (or adjusted p value) less than 0.05 was considered statistically significant.

CHAPTER 3. USING ARTIFICIAL INTELLIGENCE TO IDENTIFY TUMOR MICROENVIRONMENT HETEROGENEITY IN NON-SMALL CELL LUNG CELL

3.1 Introduction

The complexity of the tumor microenvironment is vast, with numerous cellular and structural patterns that are distinct in each cancer. Even within non-small cell lung cancer (NSCLC), a wide variety of histological variants leads to numerous possible diagnoses, each with its own preferred treatment regimen [9, 90]. Among the different subtypes of NSCLC, adenocarcinoma (ADC) and squamous cell carcinoma (SCC) are the most commonly diagnosed. Pathological assessment of patient biopsies has long been the standard for diagnosis, and pathologists are skilled at identifying the multitude of cell types, in addition to the malignant epithelial cells, that can be found in carcinomas [91-93]. While the role of the pathologist will never be replaced, a method for less highly trained researchers to quickly and accurately assess the types of cells within a histological sample would greatly benefit the field. As the NSCLC treatments move towards the use of immunotherapy as a first line therapy for most cancers [9], assessment of the tumor microenvironment (TME) is critical.

ADC and SCC TMEs are very heterogeneous and contain numerous types of cells that are often collectively referred to as 'stroma'. Commonly identified cell types in NSCLC TME include mesenchymal cells, plasma cells, macrophages, neutrophils, and lymphocytes [47, 91, 92, 94]. Although cells such as CD8+ T cells in the TME can be tumor eliminating, it is generally accepted that tumors reprogram the microenvironment to

favor tumor promoting cells. In particular, mesenchymal cells, such as cancer associated fibroblasts (CAFs), can produce a variety of cytokines, including TGF-β that can create an immunosuppressive TME by repressing CD8+ T cells and increasing regulatory T cells [95, 96]. Similarly, tumor-associated neutrophils are also thought to be predominately immunosuppressive, in particular through production of arginase and reactive oxygen species [97, 98]. A high neutrophil to lymphocyte ratio (NLR) typically predicts poor overall survival and poor responses to immunotherapies [62, 99]. However, current strategies to study the NLR of patients with cancer involves blood samples, but these may not represent the immune microenvironment at the site of the tumor.

ADC and SCC differ in their histology as well as genetic profiles, leading to divergent treatment options, with ADC possessing mutations allowing for more targeted therapies [1-3]. Among the many genetic alterations present in NSCLCs, mutations in genes such as *KRAS, TP53,* and *EGFR* are some of the most common. Mutations in *KRAS* and *EGFR* are more frequent in ADCs, with *KRAS* mutated in ~32% and *EGFR* in ~27% of tumors. However, mutations in these targetable genes are much less frequent in SCCs that instead have frequent mutations in *TP53* (90%), *PIK3CA* and *PTEN* (15%) [90, 100]. In order to produce large amounts of histologically and genetically similar tumors, researchers have designed genetically engineered mouse models (GEMMs) of lung cancers to mimic patient genetics and have used these models for systematic characterization of lung cancer TMEs. Data have shown that murine lung adenocarcinomas tend to attract macrophages [60, 80, 101], but if there are alterations in EGFR, LKB1 or late stage KRAS, neutrophils may be recruited to these tumors [48, 102, 103]. In murine squamous lung cancers neutrophils predominate and are thought to drive a transition from ADC to SCC states [59, 60, 80, 104].

Current methods to characterize the TME include flow cytometry, single cell RNAseq, mass cytometry, and other multiplexed immunohistochemistry approaches [47, 61, 92, 105]. Flow cytometry and standard single cell RNAseq are robust methods, but require a relatively large amount of live starting material that must be dissociated prior to experimental assessment. Dissociating tissues can lead to loss of fragile cell populations and erases spatial information. Spatial scRNAseq can overcome this hurdle, but is expensive to implement. Other options include spatial profiling through multiplexed immunohistochemistry, including imaging mass cytometry techniques such as fluidigm or spatial proteomics [106, 107]. These are powerful approaches, but require specialized equipment, a large investment of money for reagents, and trained personnel to interpret results [105]. Therefore, developing a TME quantification method that is more cost effective, faster to implement, and retains the sample is imperative to further research efforts and to provide clinicians a tool to help guide treatment for their patients.

In this study, we utilize the HALO® Artificial Intelligence (AI) nuclear phenotyper software by Indica Labs to identify differences in the TME in both human and murine NSCLC tissues. We investigated five murine models, including *Kras*^{G12D}*/p53-null*, *Pik3ca*^{E545K}*/p53-null*, *EGFR*$^{T790M/L858R}$*, Kras*^{G12D}*/Lkb1-null*, and *Lkb1-null/Pten-null*, to determine how the presence of these mutations alters the tumor microenvironment. We confirmed the accuracy of the algorithm with both correlation to IHC staining and by testing on lymphocyte-rich lymph node sections. We confirmed accumulations of macrophages in murine adenocarcinomas and neutrophils in murine squamous cell carcinomas in addition to further identifying differences in these tumors. In human samples, we uncovered extremely strong negative correlations between both mesenchymal cells and neutrophils with lymphocytes, and higher proportions of mesenchymal cells predicted poor overall survival.

3.2 Identification of Predominant Cell Types Within Lung Cancer GEMMs

In order to profile lung cancer TME components using H&E-stained sections, we developed an algorithm that could reliably identify cell types in both patient and murine samples based on nuclear morphology. We used the HALO® AI nuclear phenotyper software and trained the software in iterations to identify six distinct cell types: epithelial cells, mesenchymal cells, plasma cells, macrophages, neutrophils, and lymphocytes. Overall, 556,930 iterations were run, using 34,427 nuclei from 19 human samples and 33 murine samples. Representative images of human squamous cell carcinoma (Figure 3.1A) and murine squamous cell carcinoma (Figure 3.1B) show all six subtypes of cells identified by the algorithm. Neutrophils, overlaid in light blue, were identified by their polymorphonuclear or segmented nuclei. Plasma cells, shown in orange, contained a characteristic perinuclear “hof” that is a light area adjacent to the nucleus. Tumor cells, or epithelial cells, overlaid in red, were identified by their generally large cell size, pleomorphic nucleus and dark nucleoli. Mesenchymal cells, in dark blue, had elongated and spindle-shaped nuclei. Lymphocytes, in green, were characterized by small cytoplasm containing a small but often dark and rounded nucleus. Lastly, macrophages, in yellow, were identified by their round nuclei and diffuse cytoplasmic area.

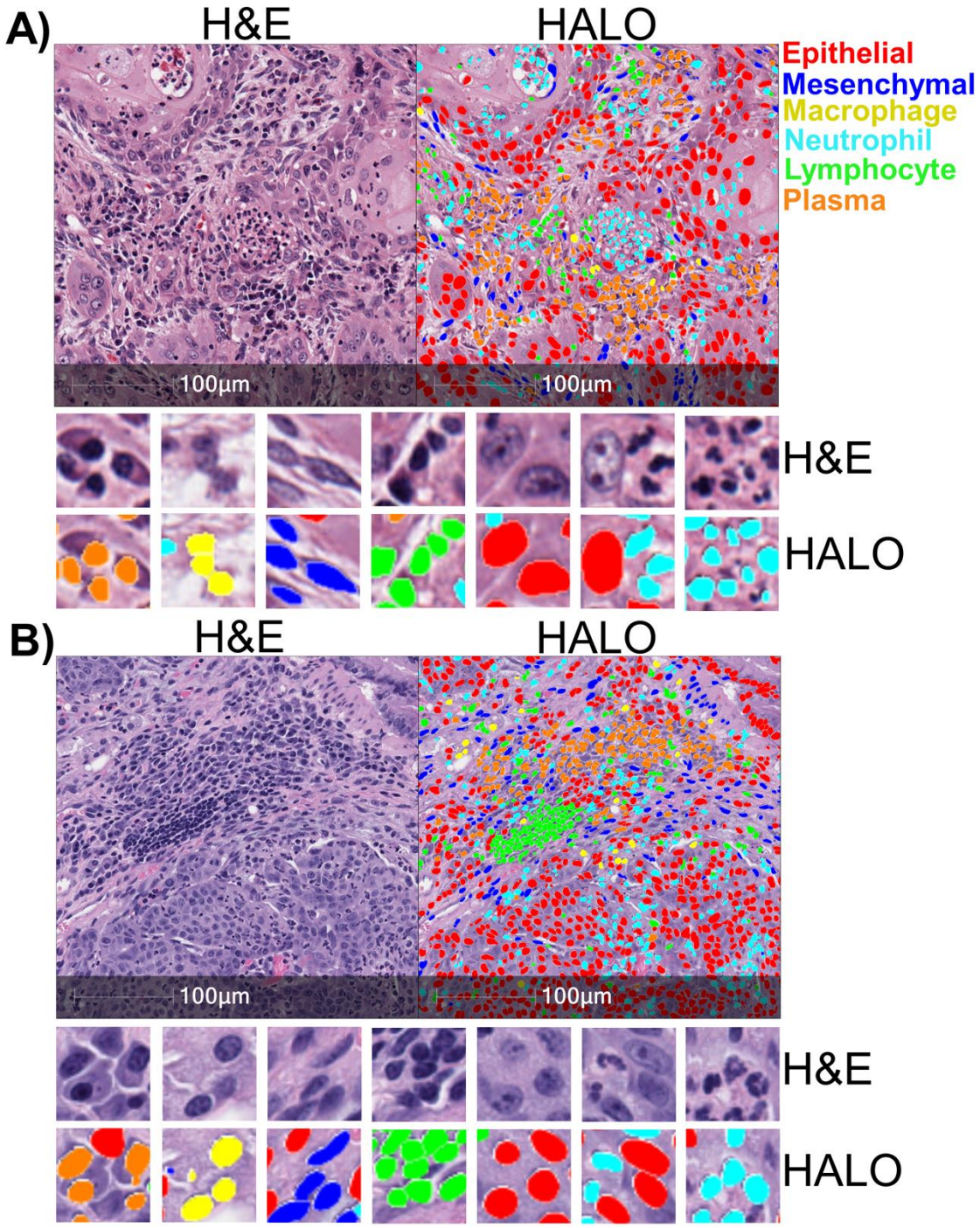

Figure 3.1: Artificial Intelligence identifies nuclear phenotypes in human and mouse lung cancers

A) H&E-stained sample from a patient with squamous cell carcinoma (left). Same H&E-stained image with different cell types identified by the HALO AI nuclear phenotyping algorithm overlaid with corresponding colors (right). Zoomed images show more detail of

the different cell types identified in the tumor immune microenvironment. B) H&E-stained sample from *Kras*^{G12D}*/Lkb1-null* mouse with squamous cell carcinoma (left), with the cell types identified by the HALO AI algorithm (right). Cell types are color-coded: epithelial/tumor cells (red), mesenchymal cells (dark blue), neutrophils (light blue), plasma cells (orange), lymphocytes (green), and macrophages (yellow).

To examine the concordance of the nuclear phenotyper algorithm with a traditional immunohistochemistry (IHC) approach, we compared identification of lymphocytes using the algorithm to IHC staining of the T cell marker CD3 and observed a strong overlap in cell identification by the two methods (Figure 3.2A). We recently reported that when one copy of the gene encoding the histone methyltransferase EZH2 is deleted in *Kras*^{G12D}*/p53-null* murine tumors, there are more abundant lymphocytes in the tumors [79]. Using tumors that were EZH2 wild-type, heterozygous and null, we compared directly the abundance of lymphocytes in the tumors as measured by the nuclear phenotyper algorithm and by CD3 IHC quantification (Figure 3.2B+C). With both methods, we observed that EZH2 heterozygous tumors had statistically more lymphocytes as a percentage of total cells. The concordance of the two methods was also strong (Figure 3.2D). To further validate the ability of the algorithm to accurately identify lymphocytes and plasma cells, we examined murine lymph nodes. The lymph nodes of a murine sample can be seen with an abundance of lymphocytes, and lower numbers of the other cell types, which is expected for typical lymph node (Figure 3.3A). In contrast, the nuclear phenotyper identifies numerous other cell types, including abundant epithelial cells when a metastatic tumor is present in the lymph node tissue (Figure 3.3B). Taken together, these data indicate that the HALO® AI nuclear phenotyper is an easy and reproducible way to identify changes to the tumor microenvironment.

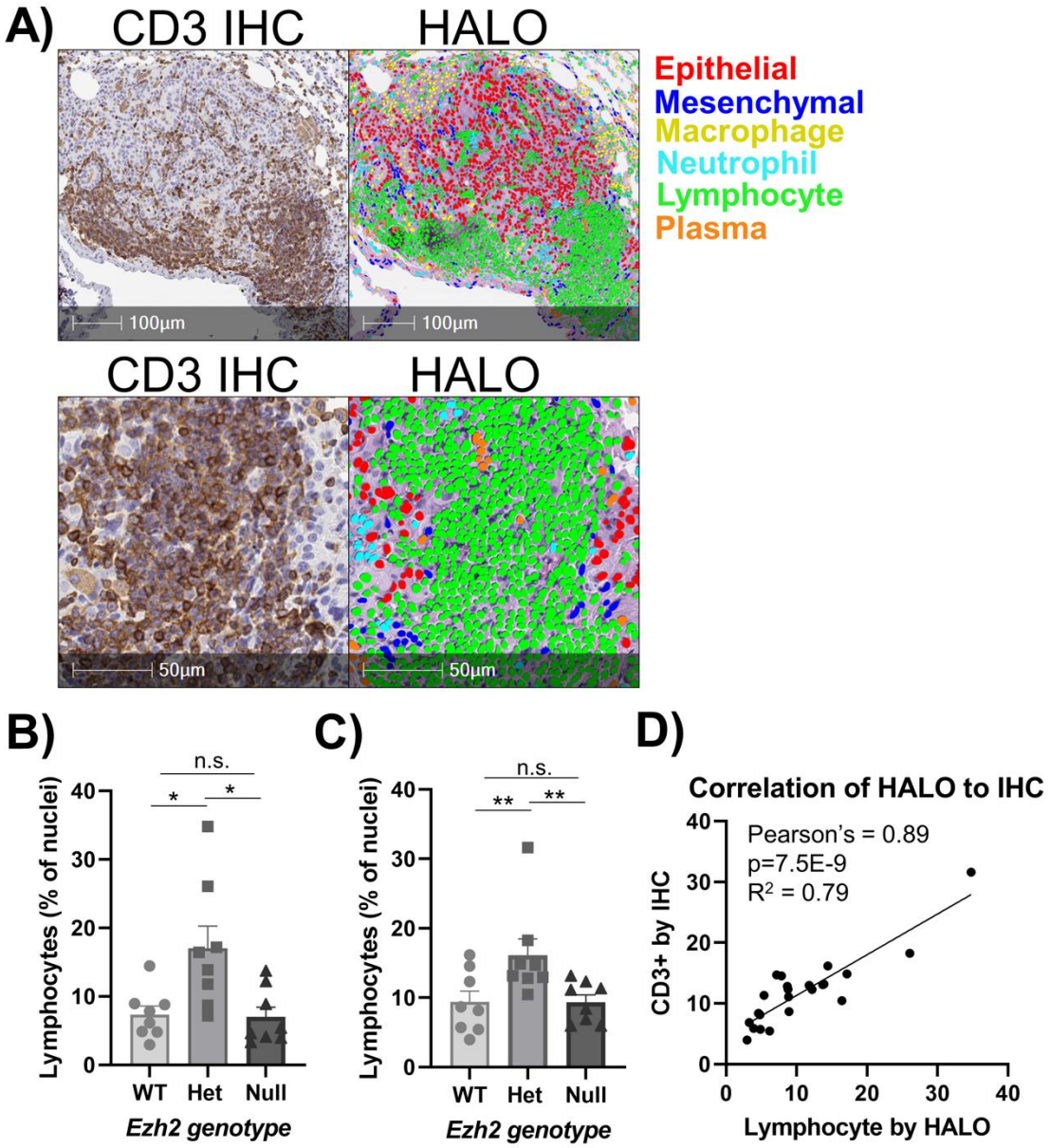

Figure 3.2: HALO AI nuclear phenotyper algorithm accurately identifies cell types

A) Representative CD3 IHC staining of lung tumor with abundant tumor-infiltrating lymphocytes. Lymphocytes in the IHC are stained with anti-CD3 antibody and stained brown (left) with HALO AI nuclear phenotyping algorithm overlaid on the H&E-stained section (right). B) Bar graph depicting the percentage of lymphocytes identified by IHC quantification, mean +/- SEM is graphed. C) Bar graph depicting the percentage of lymphocytes identified by the HALO AI nuclear phenotyper algorithm, mean +/- SEM is

graphed. D) Correlation of percentages of CD3+ cells versus lymphocytes identified by HALO AI are graphed with Pearson's correlation coefficient and R^2 values indicated on graph, n=8 mice per *Ezh*2 genotype and 24 mice total, * indicates $p<0.038$ and ** indicates $p<0.013$ by one-way ANOVA with multiple comparisons and Holm-Šídák's multiple comparisons test.

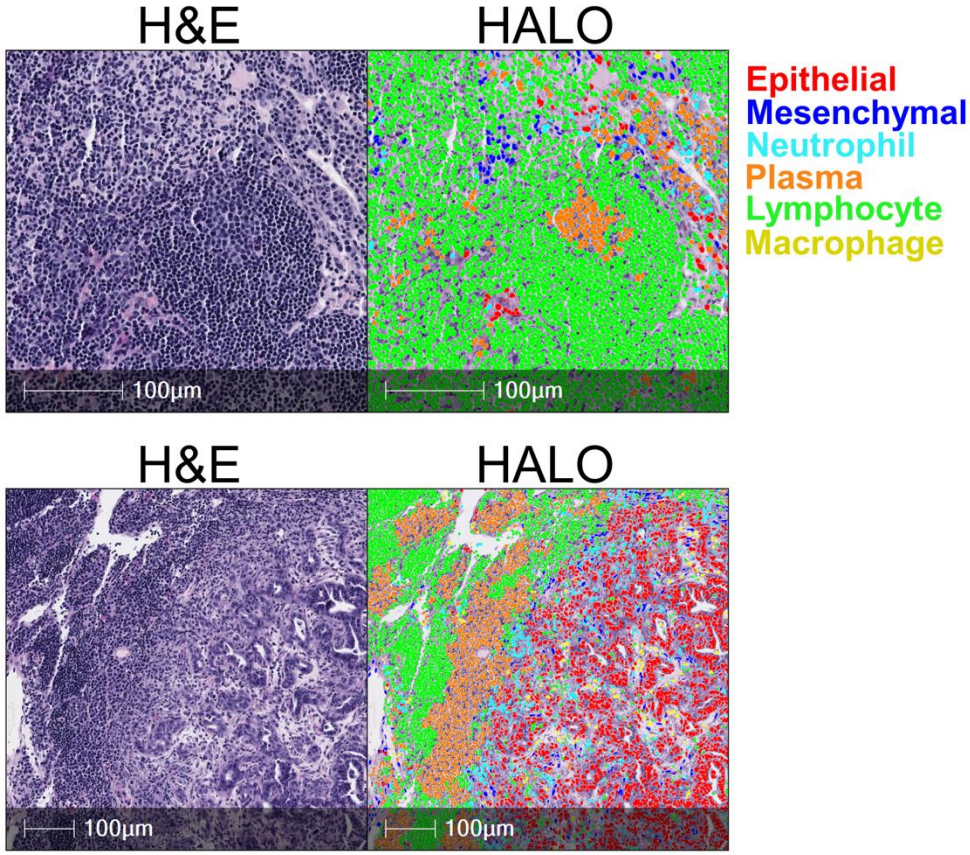

Figure 3.3 HALO AI nuclear phenotyper algorithm accurately identifies cell types

A) H&E-stained section of murine lymph node (left), with different cell types identified by the HALO AI nuclear phenotyper algorithm (right). B) H&E-stained section of murine lymph node with metastasized adenocarcinoma (left), with different cell types identified by the HALO AI nuclear phenotyper algorithm (right).

To further investigate the capabilities of the HALO® AI nuclear phenotyper algorithm, we examined H&E-stained tumors from four distinct lung cancer models: *KRAS^{G12D}/p53-null* lung adenocarcinoma [78, 108], *PIK3CA^{E545K}/p53-null* lung adenocarcinoma [18], *EGFR$^{T790M/L858R}$* lung adenocarcinoma [19], *KRAS^{G12D}/Lkb1-null* mixed lineage tumors [80, 109]. Consistent with numerous previous reports [60, 80, 101], all four models had large populations of macrophages at the site of the tumors. When considering the other abundant populations, tumors from the *KRAS^{G12D}/p53-null* model had the highest percentage of neutrophils relative to the other two models (Figure 3.4A); the *PIK3CA^{E545K}/p53-null* model had the highest percentage of mesenchymal cells (Figure 3.4C); the *EGFR$^{T790M/L858R}$* mutant model had the largest proportion of lymphocytes present (Figure 3.4B); and the *KRAS^{G12D}/Lkb1-null* had the most plasma cells (Figure 3.4D).

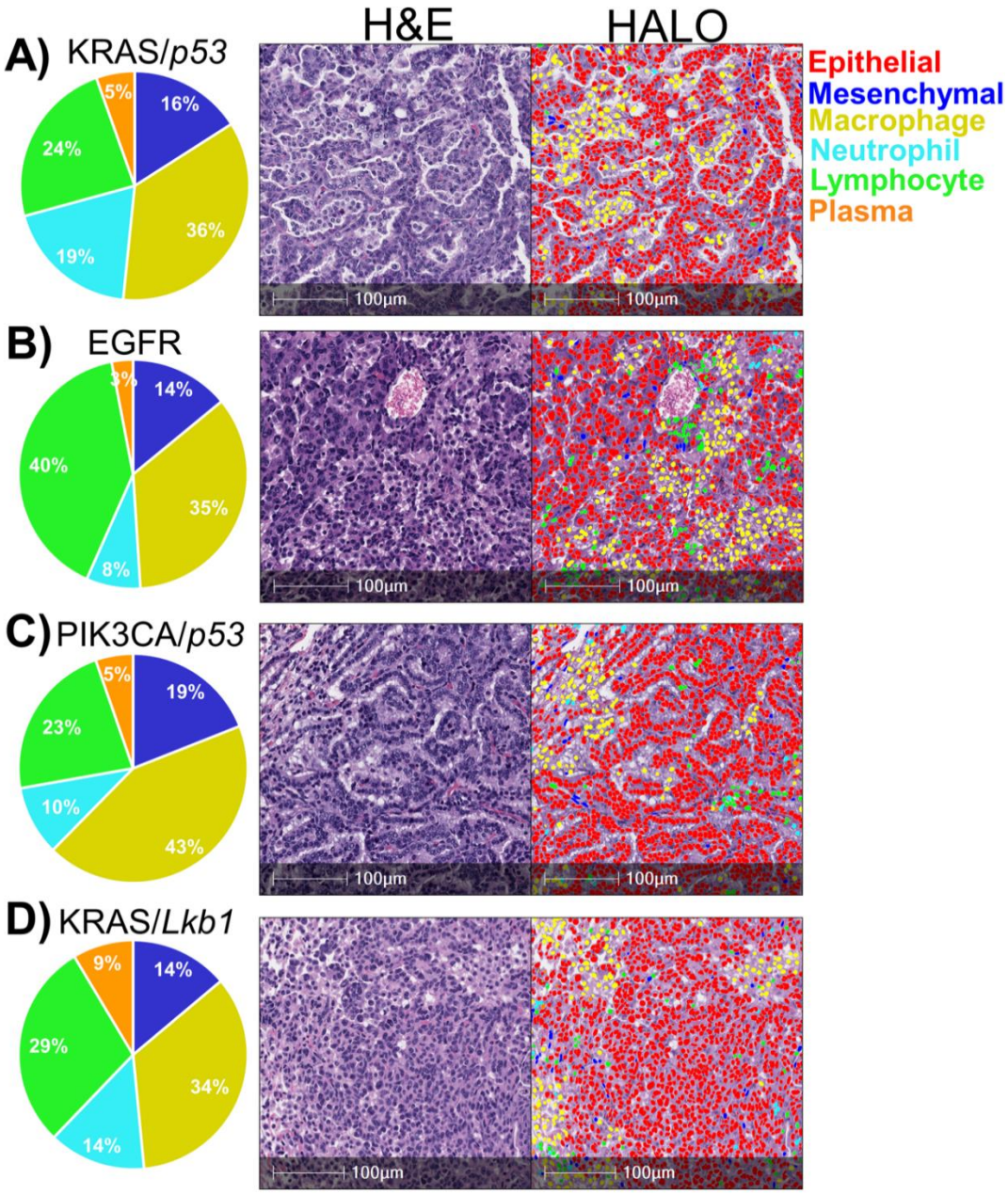

Figure 3.4: Diverse genotypes of murine lung adenocarcinomas have predominant macrophage infiltration

A-D) Representative H&E-stained sections with different cell types identified by the HALO® AI nuclear phenotyping algorithm. Pie charts represent percentages of non-epithelial cells. A) $KRAS^{G12D}$/*p53-null* lung adenocarcinomas, n=8. B) $EGFR^{T790M/L858R}$ lung adenocarcinomas, n=6. C) $PIK3CA^{E545K}$/*p53-null* lung adenocarcinomas, n=6. D) $KRAS^{G12D}$/*Lkb1-null* adenocarcinomas, n=9.

In addition to the KRAS^{G12D}/*Lkb1-null* mouse model generating adenocarcinomas, it is also capable of creating tumors of adenosquamous and fully squamous histology [80, 109]. Again, consistent with several reports [59, 80, 104], the algorithm showed that squamous areas from the KRAS^{G12D}/*Lkb1-null* model predominately recruit neutrophils (Figure 3.5A). We then explored the SCC model generated through biallelic deletion of the tumor suppressors *Lkb1-null* and *Pten-null* [60]. Tumors from this model recruit a considerable number of neutrophils, indicated by the presence of large pockets of polymorphonuclear cells (Figure 3.5B). Likewise, when we compared immune cell composition from squamous tumor models, neutrophils are predominating; however, among all the adenocarcinoma models it is macrophages that predominate (Figure 3.5C). The distinct tropisms of the adenocarcinoma and squamous cell carcinomas were particularly evident when the two tumors were juxtaposed, showing macrophages recruited toward the adenocarcinoma histology and neutrophils toward the squamous tumor (Figure 3.6).

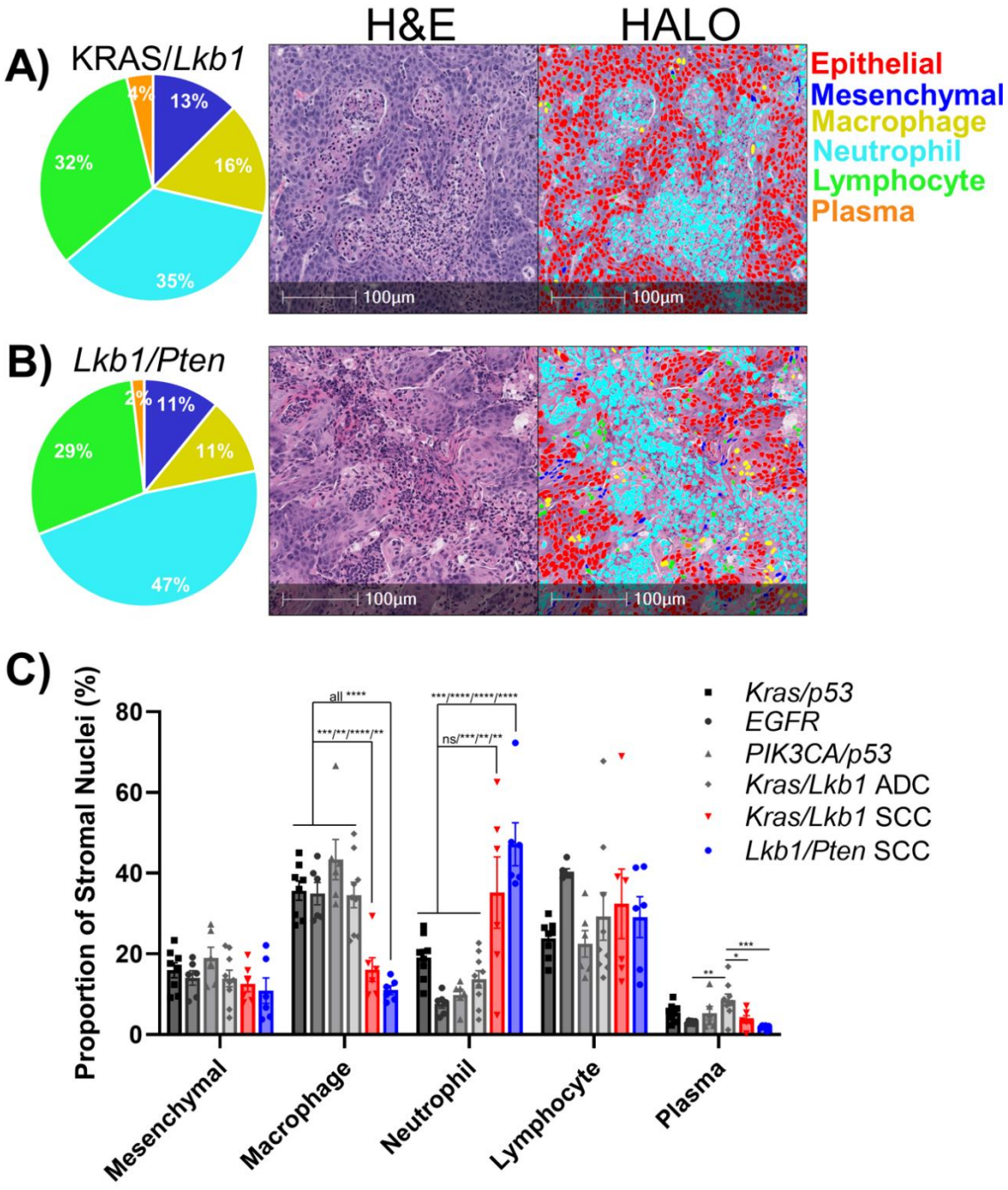

Figure 3.5: Neutrophil infiltration predominates in genetically-defined murine lung squamous cell carcinomas

A+B) Representative H&E-stained sections with different cell types identified by the HALO® AI nuclear phenotyping algorithm. Pie charts represent percentages of non-epithelial cells. A) $KRAS^{G12D}$*/Lkb1-null* squamous cell carcinomas, n=6. B) *Lkb1-null/Pten-*

null squamous cell carcinoma, n=6. C) Bar graph represents proportion of non-epithelial nuclei for the indicated genetic mouse models of NSCLC, plotted as mean +/- SEM. * indicates $p<0.02$, ** $p<0.006$, *** $p<0.001$, **** $p<0.0001$ by one-way ANOVA with multiple comparisons and Holm-Šídák's multiple comparisons test.

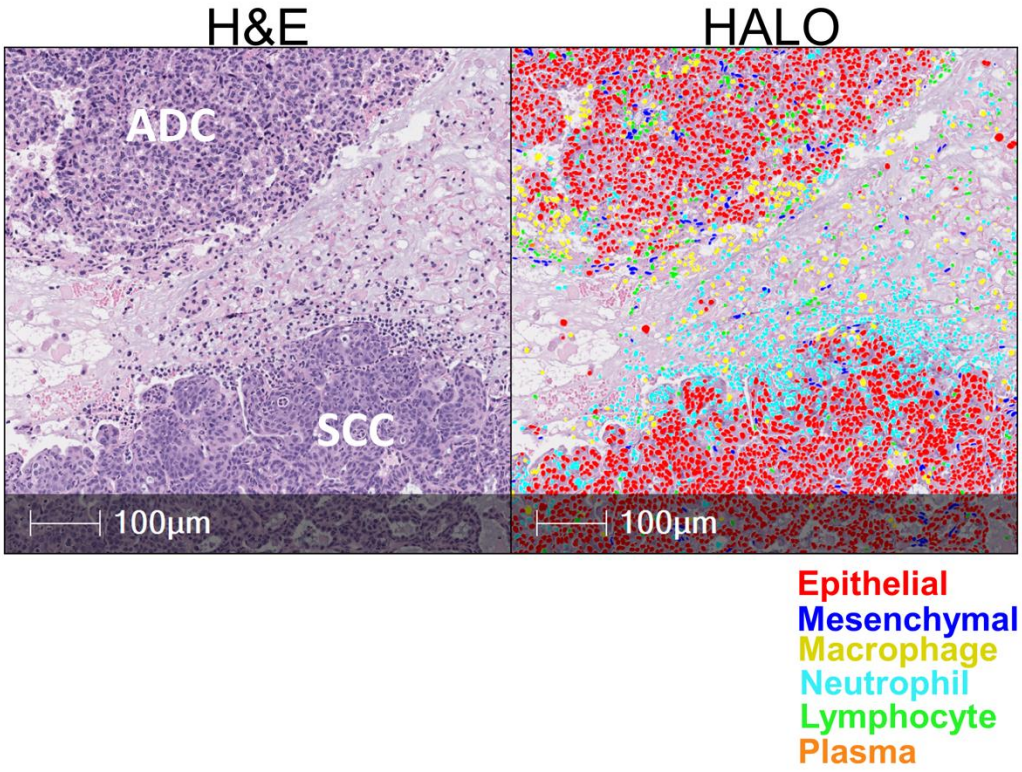

Figure 3.6: Neutrophil infiltration predominates in genetically-defined murine lung squamous cell carcinomas

H&E-stained section of murine KRAS^{G12D}*/Lkb1-null* tumors (left), with different cell types identified by the HALO AI nuclear phenotyper algorithm (right). Adenocarcinoma and squamous cell carcinoma in close proximately demonstrate the selective recruitment of neutrophils to the squamous cell carcinoma tumor (bottom), and the relatively more abundant macrophages in the adenocarcinoma tumor (top).

3.3 Characterization of Human Non-Small Cell Profiles

To examine the TME heterogeneity in human samples, we used a tissue microarray (TMA) that was generated from 216 NSCLC tumor samples. Using this TMA, we were able to recapitulate an accurate identification of the cells within the TME using the HALO® nuclear phenotyper algorithm in both ADC and SCC (Figure 3.7A+B). In contrast to our observations in the mouse models of NSCLC, we did not see any significant differences between the cell types present within these tumors (Figure 3.7C). The most commonly identified TME cell type was lymphocytes, in agreement with other work [92, 94]. The fact that the histotype did not predict cell infiltrations suggests that there are more heterogeneous factors contributing to the recruitment of immune cells within the tumor stroma in human samples than are present in our genetically-defined mouse models.

When comparing the percentages of mesenchymal cells to lymphocytes, we observed a very significant negative correlation between the two populations (Figure 3.8A). Furthermore, we observed a strongly significant negative correlation between tumor infiltrating neutrophils and lymphocytes (Figure 3.8B). This finding may indicate that mesenchymal cells and neutrophils present in the tumor stroma are phenotypically detrimental to lymphocyte survival or recruitment. To further interrogate the relationship between all the immune infiltrates identified by the HALO® AI nuclear phenotyper we created a correlation plot (Figure 3.8C). Positive correlations were observed between mesenchymal cells and neutrophils, which suggests that the mesenchymal cells could be phenotypically attracting neutrophils and together supporting a highly immunosuppressed environment. A negative correlation was also observed between macrophages and lymphocytes, but the degree of the correlation was lower.

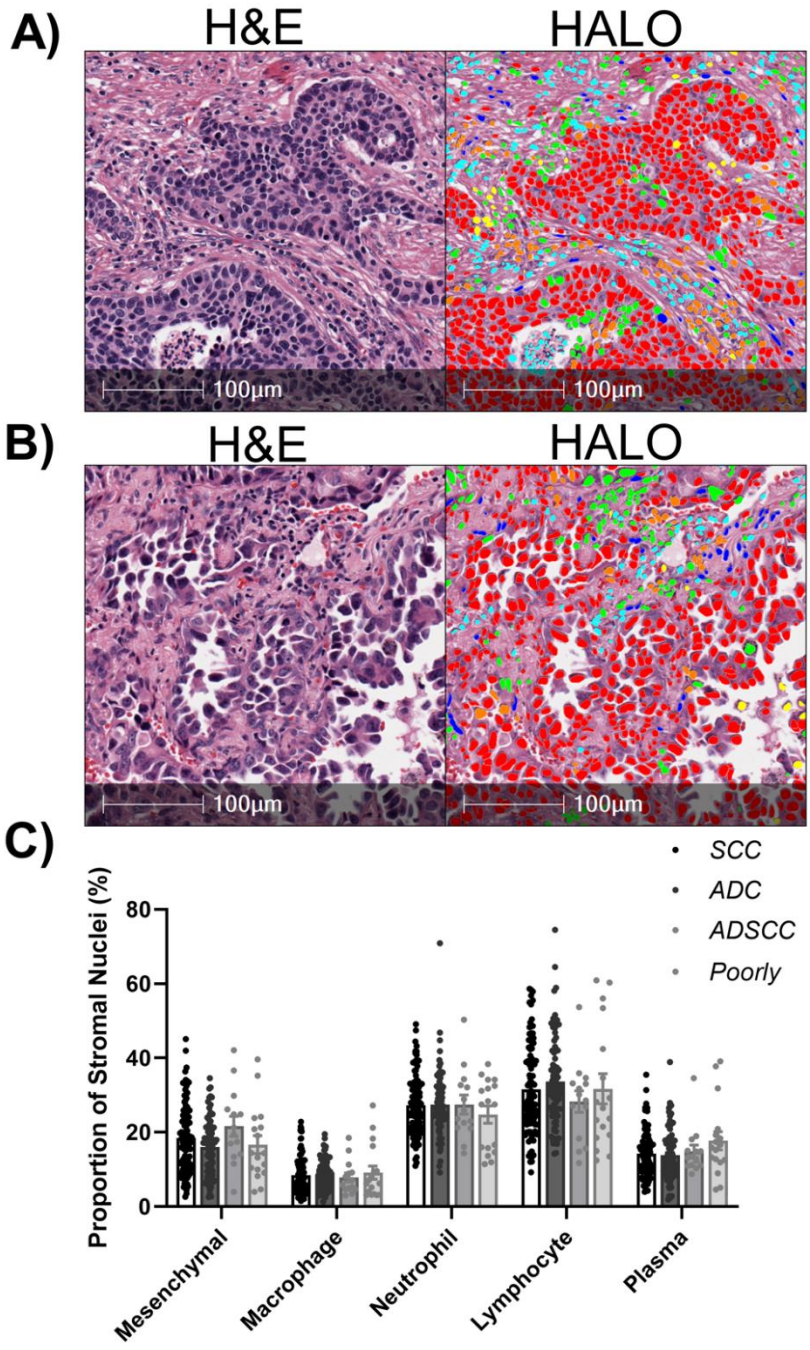

Figure 3.7: HALO AI nuclear phenotyper illustrates heterogeneity in patient NSCLC samples

A) Representative human squamous cell carcinoma. B) Representative human adenocarcinoma. C) Proportions of the different cell types within the tumor micro-environment, SCC n=102, ADC n=83, ADSCC n=14, Poorly Differentiated n=17.

We last sought to determine if abundance of any cell types within the tumors predicted poor overall survival in this cohort. We observed that patients whose tumors were classified as mesenchymal low survived longer than patients whose tumors were classified mesenchymal high (Figure 3.8D). This result was similar whether we queried all causes of death or if we limited the cohort to lung cancer-specific death (Figure 3.9A). Although not significant, high lymphocyte abundance predicted better prognosis, while a higher number of plasma cells predicted worse prognosis (Figure 3.9B+C). Lastly, neutrophil and macrophage abundance had no correlations to overall survival (Figure 3.9D+E).

Although we found that our mouse models did not entirely match patient TME based on subtypes, there are still important findings. We observed negative correlations with mesenchymal cells and lymphocytes as well as neutrophils and lymphocytes. Additionally, we found that patients that had more mesenchymal cells within their TME had a poorer outcome than patients with low mesenchymal cells. Since our mouse model subtypes did not not correlate to our TMA, these findings could be a way to further define which TMEs respond better to a specific treatment modality. Although these findings are exciting, further studies would need to be done to help us identify exact mechanisms of tumor promotion or tumor control.

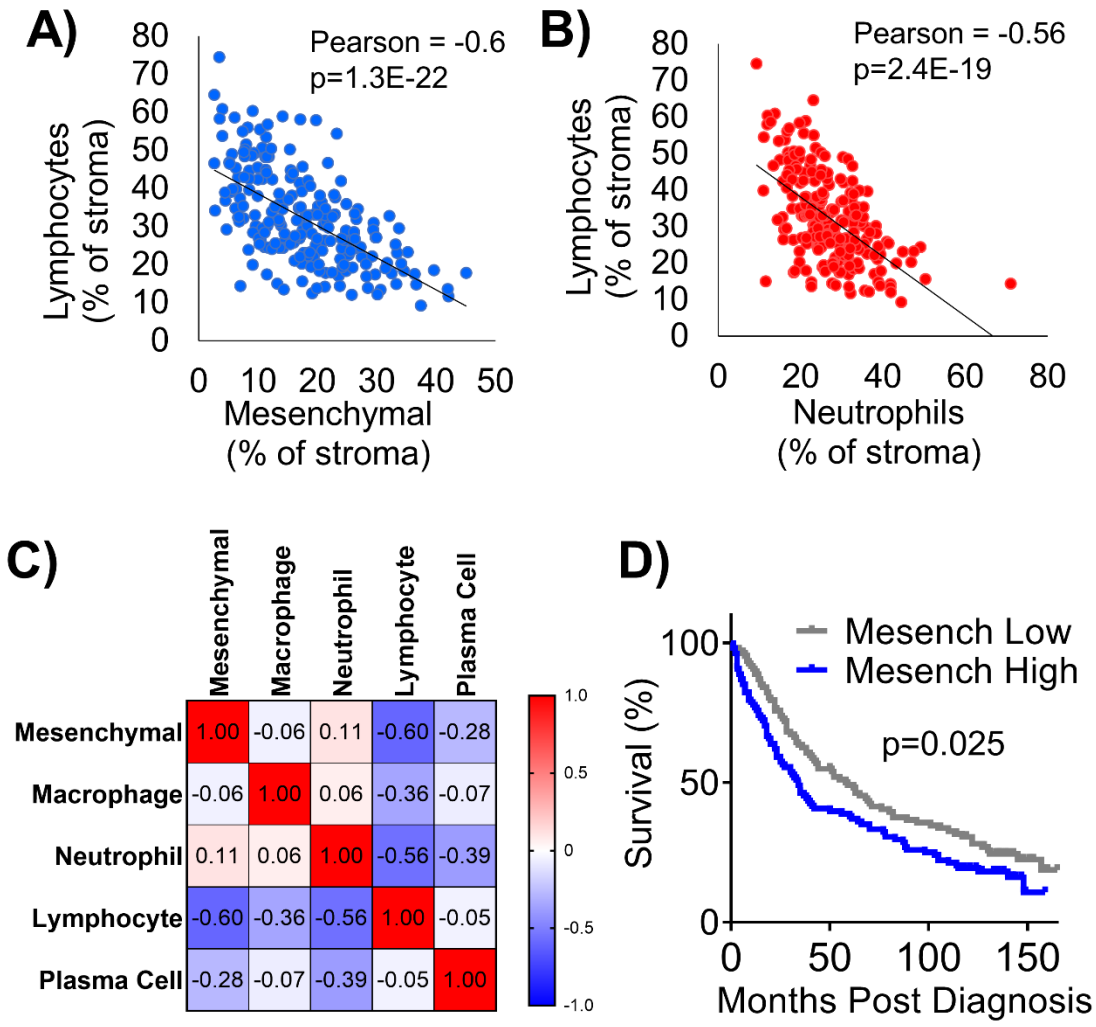

Figure 3.8: Lymphocytes negatively correlate with neutrophils and mesenchymal cells, and mesenchymal cells predict poor prognosis in human samples

A) Correlation plot between percentages of mesenchymal cells and lymphocytes, Pearson's correlation coefficient and p value indicated on graph. B) Correlation plot between percentages of neutrophils and lymphocytes, Pearson's correlation coefficient and p value indicated on graph. C) Correlation matrix depicts relationships between all tumor-associated cell types. D) Kaplan-Meier survival plot between mesenchymal low vs mesenchymal high tumors split at median, p value shown is Mantel-Cox LogRank test, n=216 patients for all plots.

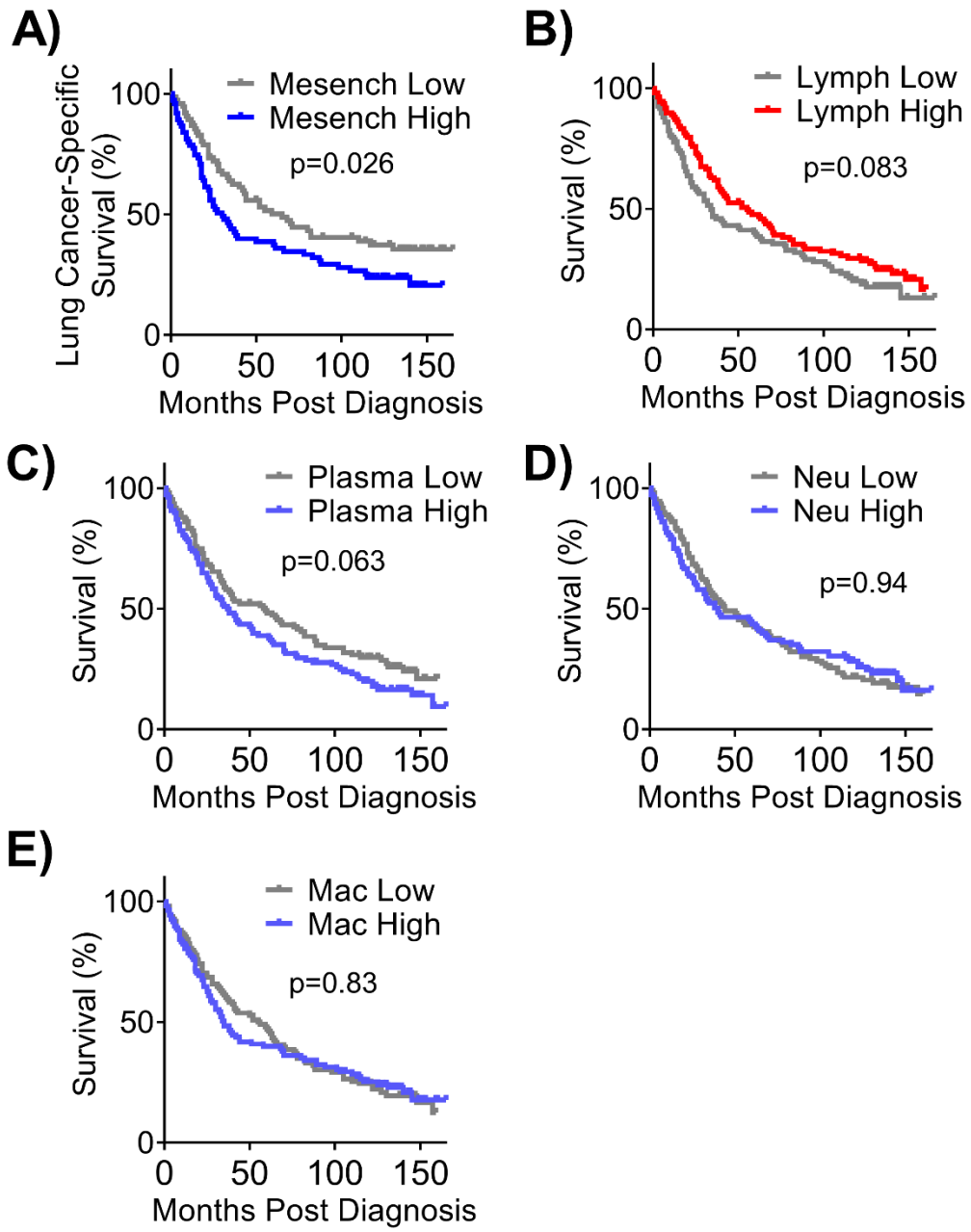

Figure 3.9: Lymphocytes negatively correlate with neutrophils and mesenchymal cells, and mesenchymal cells predict poor prognosis in human samples

A-E) Kaplan-Meier survival plots between tumors divided into two groups at the median using the indicated marker segregated at median, p value shown is Mantel-Cox LogRank test, n=216 patients for all plots.

CHAPTER 4. EZH2 INHIBITION PROMOTES TUMOR IMMUNOGENICITY IN LUNG SQUAMOUS CELL CARCINOMAS

4.1 Introduction

Lung squamous cell carcinoma (LSCC) is a subtype of non-small cell lung cancer (NSCLC) that historically has limited therapeutic options[9, 110]. The FDA recently approved first-line PD1/PD-L1 targeting immunotherapy for LSCC patients[111]. This therapy blocks the immune-evasion PD1/PD-L1 interaction, allowing for tumor-reactive T cells to expand and destroy the tumor. However, durable responses are seen in only ~20% of LSCC advanced-stage patients[112]. Efforts to increase the response rates in individuals have focused on combination therapies. EZH2 is a histone methyltransferase that catalyzes histone H3 lysine 27 tri-methylation (H3K27me3), a mark associated with gene silencing[113]. The FDA-approved EZH2 inhibitor tazemetostat [77, 114], as well as tool compounds including GSK126[115], are specific EZH2 inhibitors that serve to decrease H3K27me3, de-repress genes, and may lead to improved immunotherapy responses though several mechanisms.

In order to study LSCC in immunocompetent hosts, several autochthonous genetically engineered mouse models have been established. One such model was generated through biallelic deletion of the tumor suppressors *Pten* and *Lkb1* (aka *Stk11*)[60]. Tumors from these mice were shown to have transcriptional similarity to human LSCC, had high expression of PD-L1 on the tumor-propagating cells, and had predominant populations of tumor-associated neutrophils[60]. It is widely believed that tumor associated neutrophils, in particular neutrophils that are sometimes described as granulocytic myeloid-derived suppressor cell (Gr-MDSC), can promote tumor growth by creating a lymphocyte-suppressive microenvironment [44]. Mechanisms through which neutrophils suppress T cells include high expression of arginase, and reactive oxygen

species[44]. However, some neutrophils are thought to be tumor eliminating, and can create a pro-lymphocyte environments through production of TNF-α and CXCL10, and antigen presentation[44]. The neutrophil to lymphocyte ratio appears to strongly predict response to immunotherapy, suggesting that in the majority of NSCLCs, neutrophils are T cell suppressive[116].

One essential mechanism for T cell activation is by co-stimulation through antigen presentation by major histocompatibility complexes (MHC) I and II. Many tumor cells have evolved to repress antigen presentation machinery in order to evade the immune system surveillance[25]. It has been reported that patient tumors with high expression of MHC II demonstrate greater response to anti-PD-1 checkpoint inhibitors in melanoma[63]. In other cancer types, it has been demonstrated that both MHC I and MHC II can be regulated by the chromatin modifying enzyme enhancer of zeste 2 (EZH2)[25, 117-120].

Here, we utilized several murine and human models of lung squamous cell carcinoma (LSCC) to understand if and how EZH2 inhibition will boost immunotherapy responses. We found that inhibition of EZH2 catalytic activity with either GSK126 or EPZ6438 in the presence of IFNγ was able to de-repress numerous genes encoding antigen presentation constituents and the pro-T cell chemokines CXCL9/10/11 in both human and murine tumoroids. ChIP-sequencing in human patient-derived tumoroids (PDTs) further delineated the patterns of epigenetic changes in response to EZH2 inhibition and IFNγ treatment. In both autochthonous and syngeneic grafts, EZH2 inhibition alone or with immunotherapy led to excellent tumor control. Single cell RNA-sequencing (scRNAseq) and flow cytometry showed changes consistent with more immunogenic tumor cells and a more pro-T cell tumor microenvironment. Together, these data strongly support the addition of EZH2 inhibition to immunotherapy regimens that have now become first line treatment for many LSCC patients.

4.2 EZH2 inhibition allows up-regulation of MHC Class I and Class II in multiple models of lung squamous cell carcinoma

The Polycomb Repressive Complex 2 plays a central role in gene repression, including genes involved in immunogenicity[25, 117-120]. In order to understand the tumor-cell intrinsic effects of EZH2 inhibition, we treated four different non-small cell lung cancer cell lines with the EZH2 inhibitors GSK126 or EPZ6438 for 5 days, followed by one day of stimulation with IFNγ. We reasoned that this would allow for the de-repression of numerous loci in the cells, and that IFNγ treatment could then activate interferon responsive genes (Figure 4.1). Analysis of mRNA expression in these cultures showed that the MHC class I genes *B2M* and *HLA-A* were robustly upregulated by IFNγ in all cell lines, and that EZH2 inhibition lead to further *HLA-A* up-regulation in three out of four cell lines (Figure 4.2). The MHC class II gene *HLA-DRA* and a regulatory gene *CIITA* and showed a similar pattern, with significant stepwise increases in HLA-DRA expression with EZH2 inhibition, IFNγ treatment and combination (Figure 4.2). We also examined gene expression of *CD274* (encoding PD-L1) and the putative LSCC stem cell marker NGFR (Figure 4.3A). NGFR showed up-regulation at the protein level in 3 cell lines, but not in HCC95 that already expresses very high NGFR levels (Figure 4.3B). Consistent with our previous work[80], we observed that *NGFR* was up-regulated by EZH2 inhibitor in A549 cells. PD-L1 results show that while IFNγ can reproducibly up-regulate this T cell suppressor, only in the HCC15 cell line does EZH2 inhibition drive additional expression. To examine if the up-regulation in genes led to increased cell surface protein expression, flow cytometry was used. An antibody against the MHC Class I proteins HLA-A,B,C showed a stepwise increase in expression levels, with the highest levels observed in IFNγ and EZH2 inhibitor co-treated cultures (Figure 4.4A). PD-L1 expression was up-regulated significantly by IFNγ in A549 and HCC15 lines, and again HCC15 was the only cell line for which PD-L1 expression was further boosted by EZH2 inhibition (Figure 4.3A+B).

Strikingly, MHC Class II protein HLA-DR was dramatically increased in the cultures treated with a combination of IFNγ and EZH2 inhibitor, even in the H520 cells in which EZH2 inhibition drove a negligible increase in HLA-DRA mRNA (Figure 4.2B, 4.4). Lastly, we confirmed changes in B2M and HLA-DR,DQ,DP and efficacy of EZH2 inhibition by H3K27me3 levels by western blotting (Figure 4.4C).

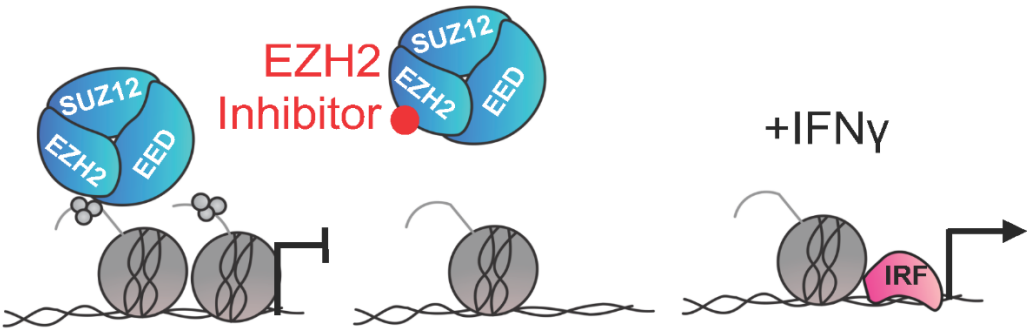

Figure 4.1: EZH2 inhibitors allow for de-pression of genes involved in antigen presentation

PRC2 silencing occurs through the catalytic activity of EZH2 by histone 3 lysine 27 tri-methylation. EZH2 inhibitors such as GSK126 and EPZ6438 block activity of EZH2 and allows formerly silence genes to become poised for transcription. Some of these genes are canonically activated by IFNγ; therefore, treatment with EZH2 inhibitors plus IFNγ allows them to now be expressed.

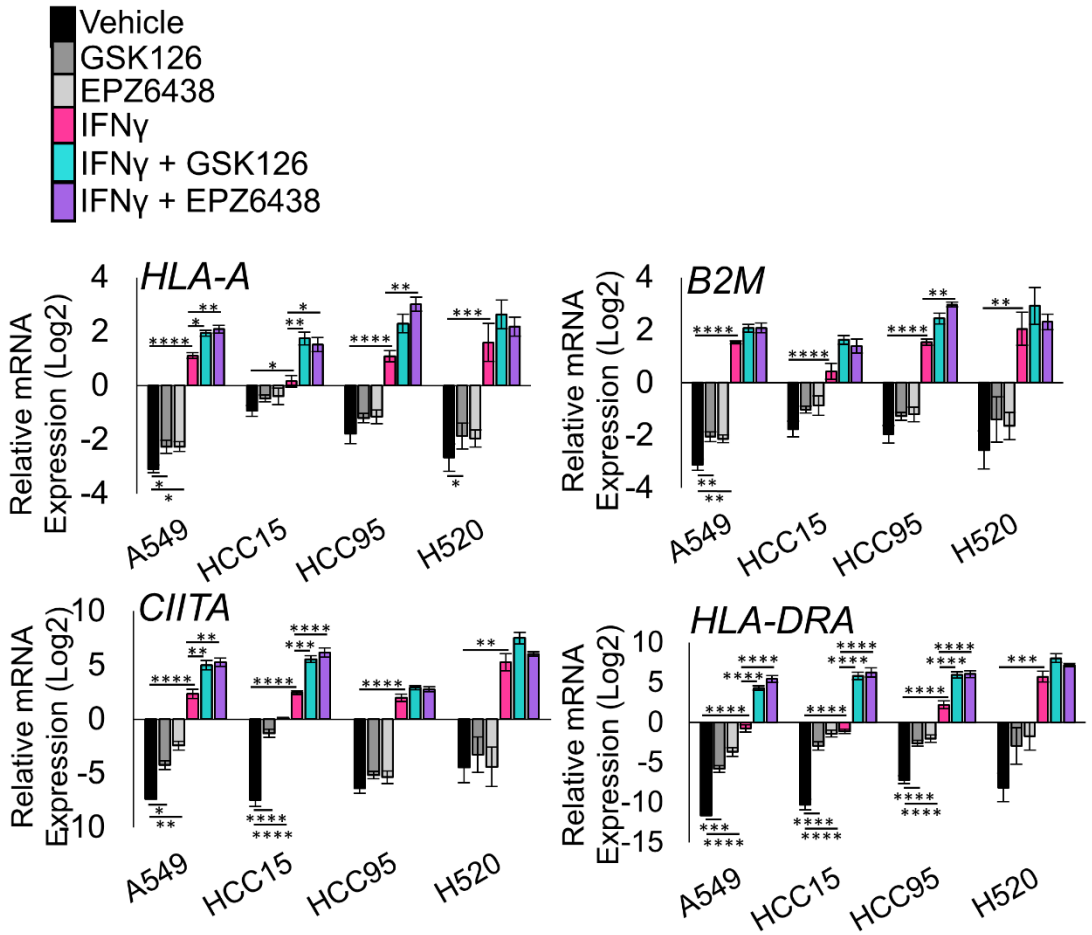

Figure 4.2: Combining EZH2 inhibitors with IFNγ increases MHC I and II gene expression in 2D human cell lines of LSCC

RT-qPCR in the indicated four human lung cancer cell lines treated for 7 days with vehicle or EZH2 inhibition with IFNγ added on day 5 for the genes *B2M*, *HLA-A*, *CIITA* and *HLA-DRA*, mean +/- SEM is graphed, n = 4 individual cultures, *indicated p<0.04, **p<0.006 ***p<0.007, ****p<0.0001 by one-way ANOVA with pairwise comparisons and Holm-Šídák's *post hoc* test.

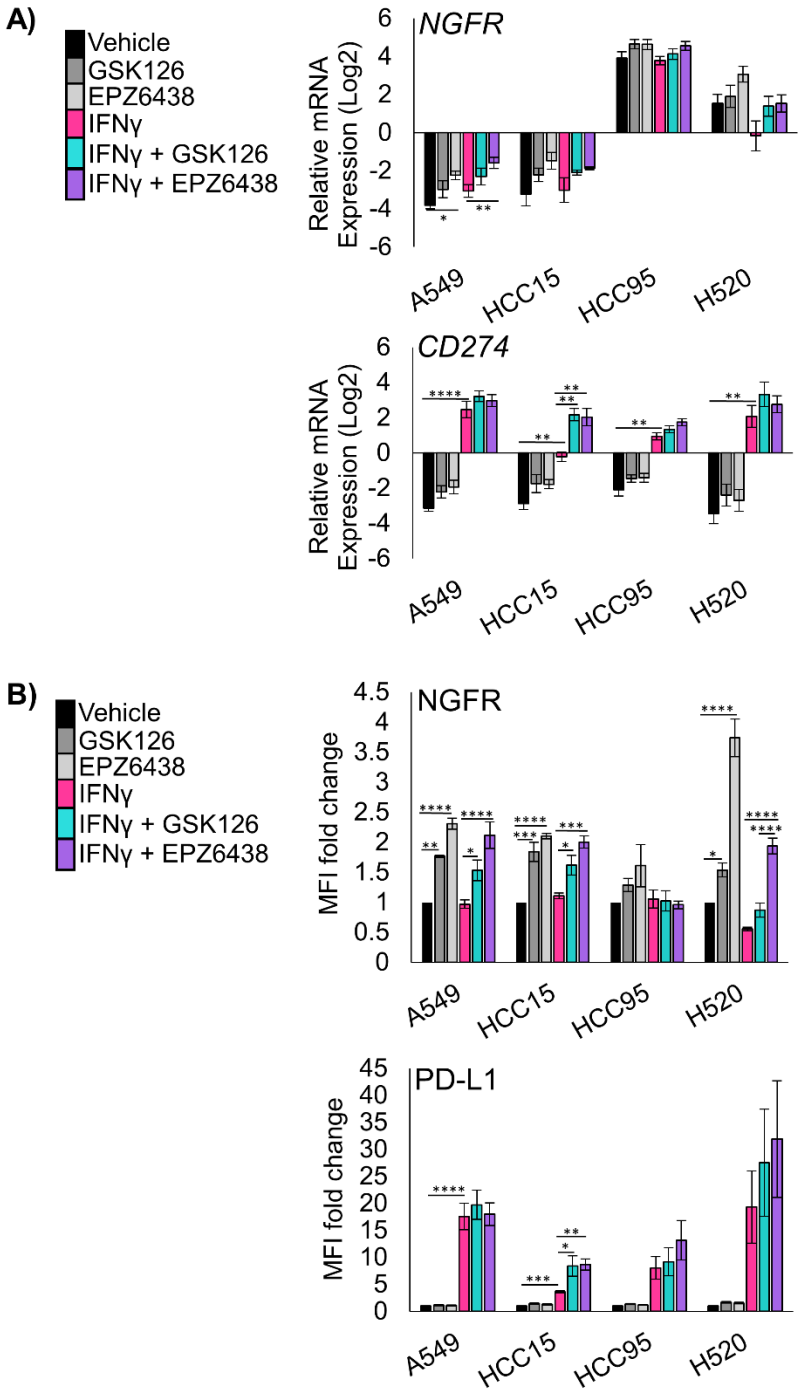

Figure 4.3: NGFR and PD-L1 expression can be increased by treating 2D cell lines with EZH2 inhibitors alone and combined with IFNγ

A) RT-qPCR in the indicated four human lung cancer cell lines treated for 6 days with vehicle or EZH2 inhibition with IFNγ added on day 5 for the genes *NGFR* and *CD274*, mean +/- SEM is graphed, n = 4 individual experiments, * indicated p= 0.0481 **p=0.0024

by one-way ANOVA with pairwise comparisons and Holm-Šídák's *post hoc* test. B) Flow cytometry analysis of indicated four human lung cancer cell lines treated for 6 days with vehicle or EZH2 inhibition with IFNγ added on day 5 for the cell surface proteins NGFR and PD-L1, mean +/- SEM is graphed, n = 4 individual experiments, * indicated p = 0.0251, **p<0.006, ***p<0.0003, ****p<0.0001 by one-way ANOVA with pairwise comparisons and Holm-Šídák's *post hoc* test.

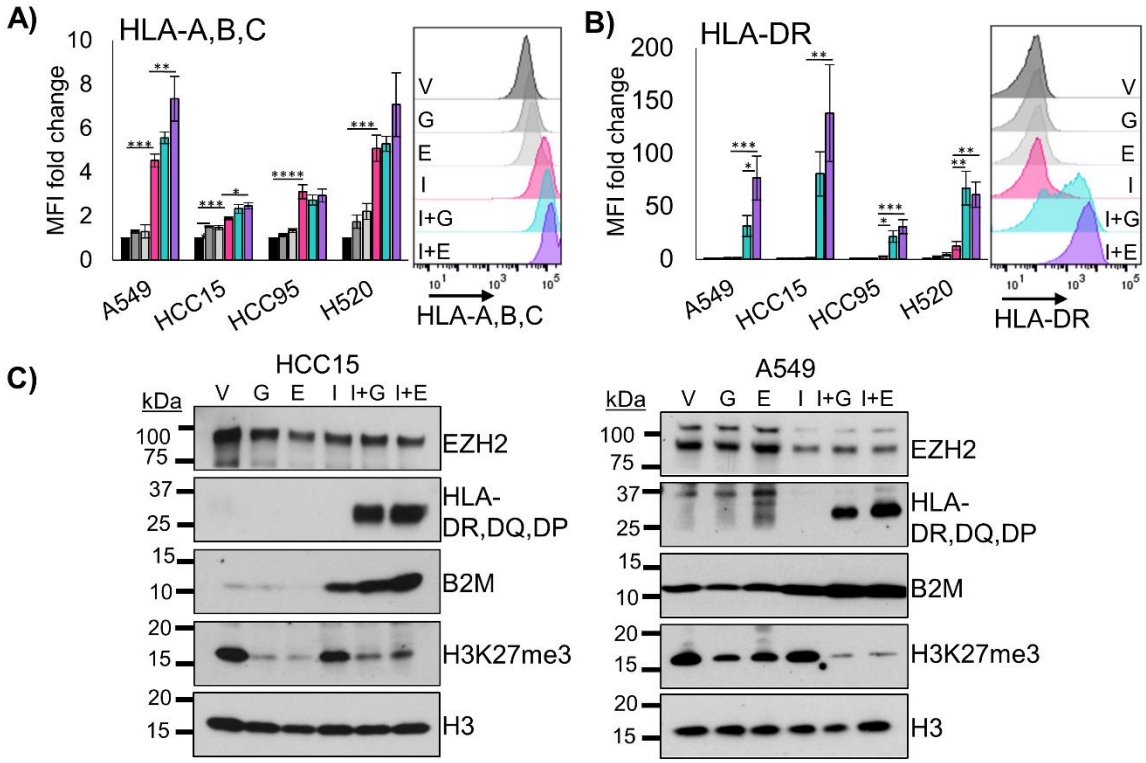

Figure 4.4: MHC I and II molecules induced by IFNγ and boosted by combining EZH2 inhibitors

A,B) Flow cytometry analysis of indicated four human lung cancer cell lines treated for 6 days with vehicle or EZH2 inhibition with IFNγ added on day 5 for the cell surface proteins HLA-A,B,C and HLA-DR, mean +/- SEM is graphed, n = 4 individual cultures, * indicated p<0.0331, ** p<0.0057, ***p<0.0009, ****p<0.0001 by one-way ANOVA with pairwise comparisons and Holm-Šídák's *post hoc* test. Representative histograms shown for one cell line C) Western blotting of A549 and HCC15 cell lines treated for 6 days with vehicle or EZH2 inhibition with IFNγ added on day 5 for the proteins B2M, HLA-DR,DQ,DP, EZH2, H3K27me3 and total histone H3. Data are representative of two individual cultures

Three-dimensional (3D) cultures allow for growth of tumor cells that cannot proliferate in 2D, and these cultures can retain the epigenetic state of *in vivo* tumors[79]. Therefore, we developed two patient-derived tumoroid (PDT) cultures from distinct LSCC patients (Figure 4.5). We treated these PDTs with the EZH2 inhibitors GSK126 and EPZ6438 for nine days, followed by two days of EZH2 inhibition with IFNγ. In tumoroids treated with EZH2 inhibitor and IFNγ, B2M and HLA-A mRNA were both increased (Figure 4.6A), as well as *CD274* and *NGFR* gene expression (Figure 4.7A). Similarly to the 2D cultures, the most striking results were with *CIITA* and *HLA-DRA* (Figure 4.6A). By flow cytometry, both HLA-A,B,C and HLA-DR have significantly higher expression in tumoroids treated with both EZH2 inhibition and IFNγ (Figure 4.6B). Cell surface expression of NGFR and PD-L1 proteins were changed very minimally by the treatments (Figure 4.7B). These results in 3D tumoroid cultures and the 2D cultures strongly implicate that de-repression of MHC class II is one of the primary outcomes of EZH2 inhibition in murine and human lung squamous cell carcinomas.

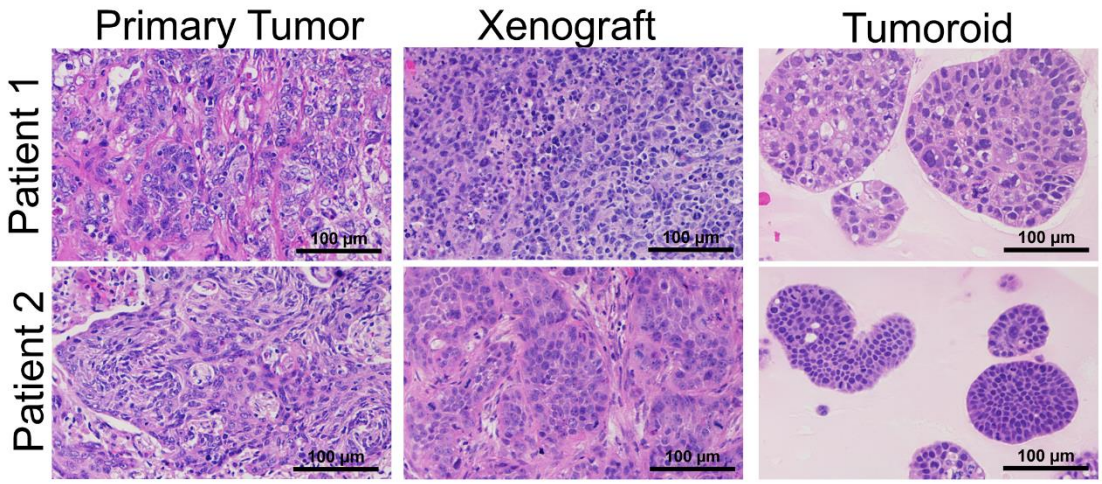

Figure 4.5: Tumoroids generated from human LSCC mimic histology of primary tumor of patients

Hematoxylin and eosin staining of primary squamous cell carcinoma tissue, xenograft tissue from primary patient tissue, and tumoroids generated from xenografts, scale bars = 100µm.

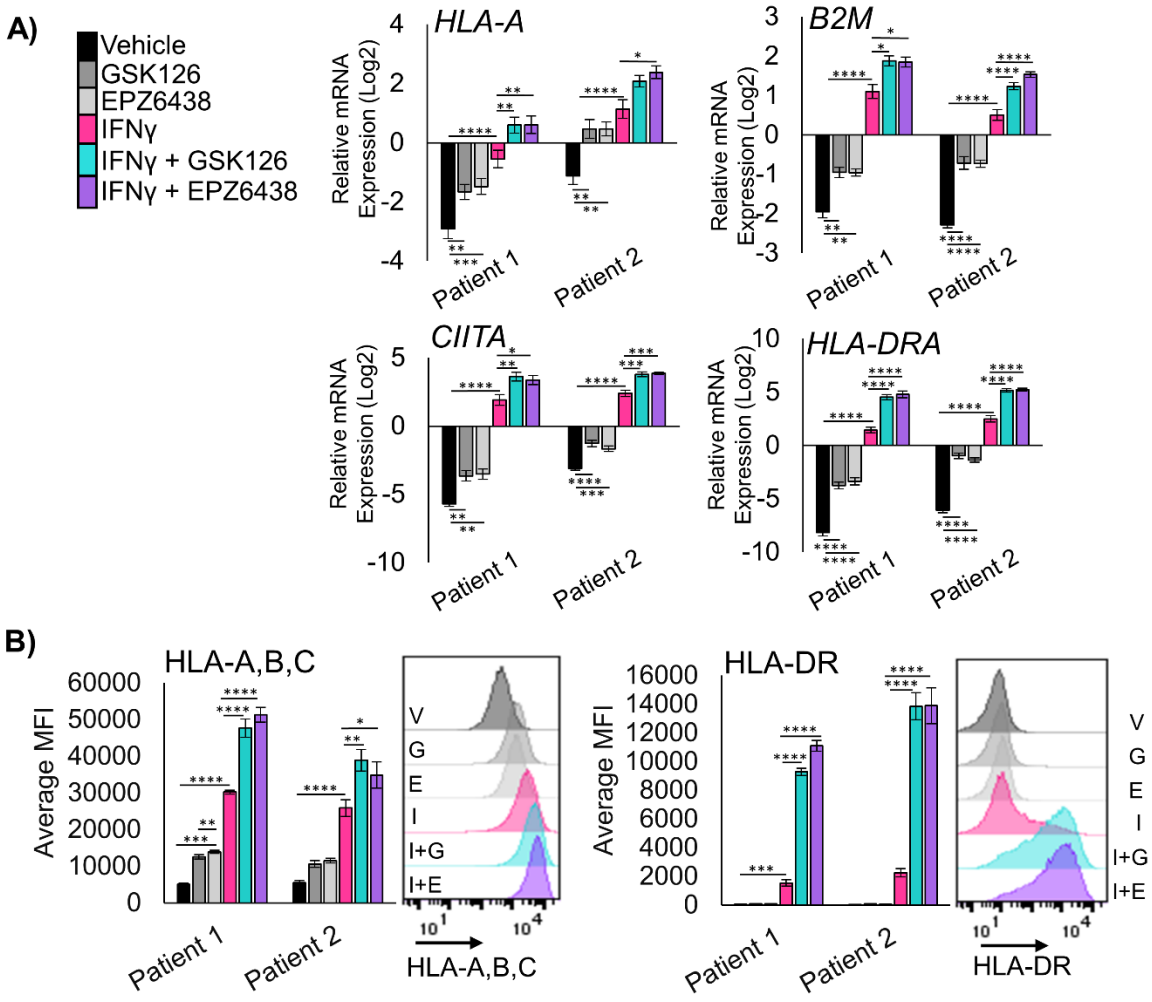

Figure 4.6: Gene and protein expression of MHC class I and II in patient derived organoids upregulated after EZH2 inhibition combined

A) RT-qPCR in two lines of patient derived tumoroids treated for 11 days and IFNγ added on day 9 for the genes *HLA-A*, *B2M*, *CIITA*, and *HLA-DRA*, mean +/- SEM is graphed, n = 4, * indicated p<0.05, **p<0.005, ***p<0.008, ****p<0.0001 by one-way ANOVA with multiple comparisons and Holm-Šídák's post hoc test. B) Flow cytometry analysis of both patient derived tumoroids treated for 11 days with IFNγ added in on day 9 for cell surface proteins HLA-A,B,C and HLA-DR, mean +/- SEM is graphed, n=4 biological replicates, * indicated p = 0.04, ** p<0.031, ***p<0.009, ****p<0.0001 by one-way ANOVA with multiple comparisons and Holm-Šídák's post hoc test. Representative histograms for patient 1 are shown.

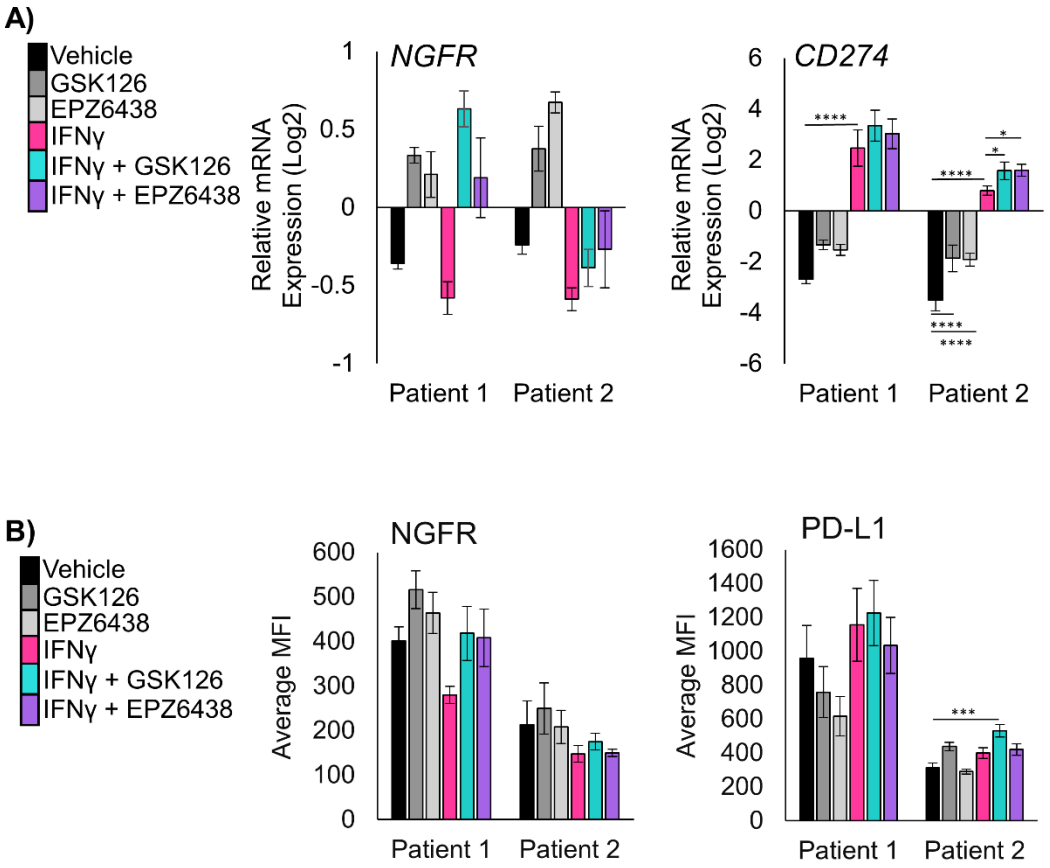

Figure 4.7: PD-L1 gene expression increases when activated by IFNγ and boosted when treated with the combination of EZH2 inhibition in 3D patient derived organoids

A) RT-qPCR in the indicated two unique patient derived tumoroid cultures treated for 11 days and IFNγ added on day 9 for the genes *NGFR* and *CD274*, mean +/- SEM is graphed, n = 4 individual experiments, * indicated p 0.0371, ****p<0.0001 by one-way ANOVA with pairwise comparisons and Holm-Šídák's *post hoc* test. B) Flow cytometry analysis of indicated two unique patient derived tumoroid cultures treated for 11 days and IFNγ added on day 9 for the cell surface proteins NGFR and PD-L1, mean +/- SEM is graphed, n = 4 individual experiments, *** indicated p <0.0007 by one-way ANOVA with pairwise comparisons and Holm-Šídák's *post hoc* test.

4.3 RNA- and ChIP-sequencing reveal regulation of both MHC and cytokine expression in tumor cells treated with EZH2 inhibitors

To effectively test immunotherapies *in vivo*, hosts with intact immune systems must be used. Genetically engineered mouse models meet this requirement by allowing for tumor formation in the autochthonous setting. We previously reported that conditional bi-allelic deletion of the genes *Pten* and *Lkb1* (aka *Stk11*) with inhaled adeno-Cre virus leads to lung squamous cell carcinoma[60]. From these squamous tumors, we developed tumoroid cultures (Figure 4.8A). Tumoroids treated with IFNγ were able to robustly upregulate all the MHC class I and class II genes tested and EZH2 inhibition was not needed for this effect (Figure 4.10A). There was a small, albeit significant, up-regulation in the HLA-A ortholog *H2-KI* in Mouse 2 with the combination treatment. Similar to human models, *Ngfr* was up-regulated by EZH2 inhibition. Next, we performed flow cytometry, and observed significant increases in H2-K^d,D^d and I-A/I-E, the mouse orthologs to human MHC I and II, in cultures treated with IFNγ and EZH2 inhibitor relative to IFNγ alone (Figure 4.8B). Furthermore, we saw a significant increase in NGFR and PD-L1expression in the group treated with the combination as well (Figure 4.10A). It is also important to note that once again NGFR upregulation occurs with EZH2i alone with Mouse 2, just as we saw in the human systems.

To further confirm gene programs that are regulated by EZH2 inhibition in a conserved fashion in both mouse and human lung SCC tumoroids, we performed RNAseq on all four tumoroid models. We compared genes up-regulated by IFNγ and EZH2 inhibition relative to vehicle treatment, and genes up-regulated by combination of EZH2 inhibition and IFNγ relative be to IFNγ (Figure 4.9). In addition to genes involved in antigen presentation, we observed a conservation of up-regulation of the pro-T cell chemokines *CXCL9/10/11* with EZH2 inhibition combined with NFγ treatment. In human cells, there

was also a down-regulation of the pro-neutrophil cytokines *CXCL1/2/3*, and the cytokines *IL1A* and *IL1B* in response to treatment with EZH2 inhibition and IFNγ. We next performed gene set enrichment analysis (GSEA) and observed a decrease in MYC targets, E2F targets, and DNA repair gene programs in response to EZH2 inhibition. Additionally, we saw an increase in pathways involved in the inflammatory response and IFN-response in response to EZH2 inhibition, and both effects were maintained when IFNγ was also added (Figure 4.10B, Supp Table 1).

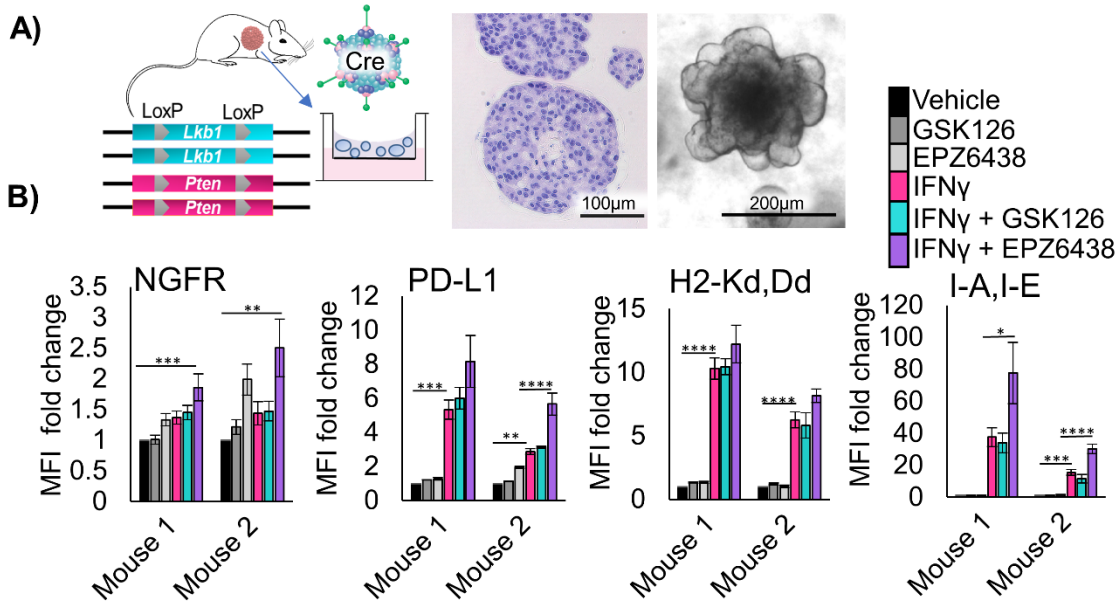

Figure 4.8: Murine LSCC organoids resemble histology found in genetically altered mouse model and upregulate PD-L1 and MHC class II

A) Schematic: Generation of murine tumoroids in air-liquid interface from tumor induced in *Lkb1/Pten* mice by adenoCre administration, showing H&E stain of tumoroids, scale bar = 100µm, and brightfield microscopy, scale bar = 200µm. B) Flow cytometry analysis of two separate murine tumoroid models treated for 11 days with EZH2 inhibitor and IFNγ added on day 9 and stained for cell surface expression of NGFR, PD-L1, H2Kd,Dd, and I-A/I-E, n = 4 individual experiments, n=3 for I-A/I-E* indicated p = 0.0321, **p<0.009, ***p<0.0009, ****p<0.0001 by one-way ANOVA with multiples comparisons and Holm-Šídák's *post hoc* test.

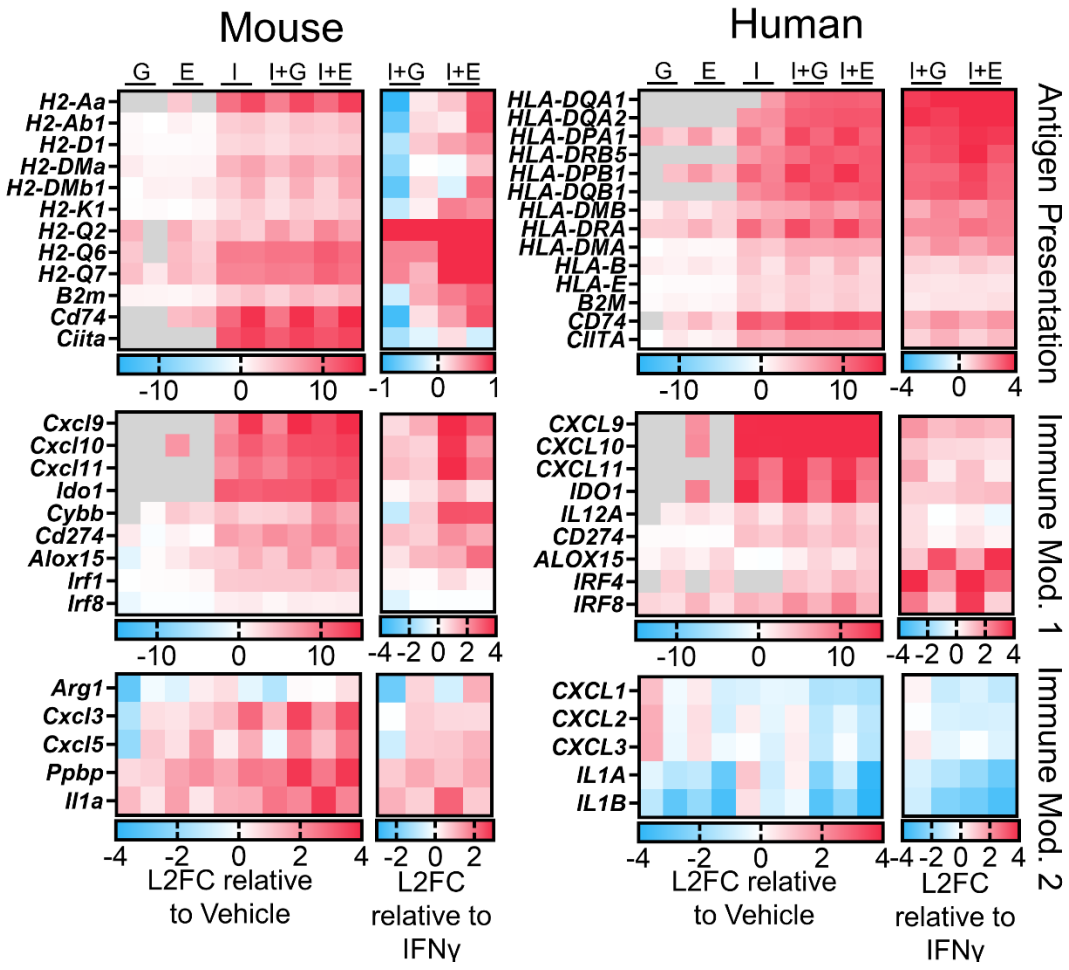

Figure 4.9: Murine LSCC organoids share de-repression of MHC and pro-T cell cytokines with human models

Heat maps of Log2-fold change (L2FC) in expression level from patient derived and murine tumoroids treated for 11 days and IFNγ added in on day 9, G=GSK126, E=EPZ6438, I=IFNγ, I+G= IFNγ+GSK126 and I+E= IFNγ+EPZ6438. For each map, the first columns are sample 1, the second columns are sample 2. Expression relative to vehicle control and relative to IFNy only are depicted.

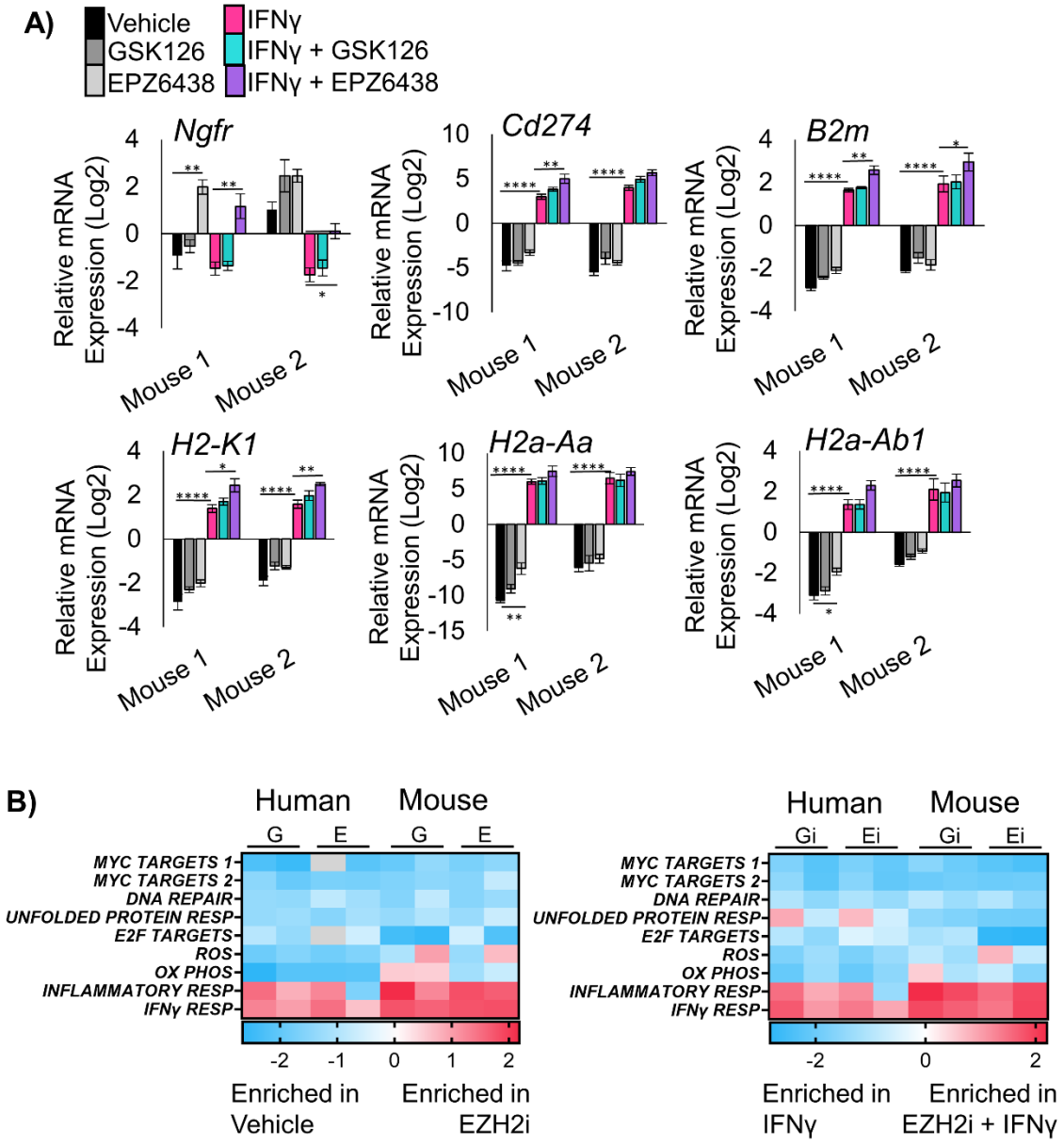

Figure 4.10: Gene expression of antigen presentation machinery in mouse tumoroids

A) RT-qPCR in the indicated two unique murine tumoroid cultures treated for 11 days with EZH2i and IFNγ added on day 9 for the genes *Ngfr, B2m, H2-K1, Cd274,* and *H2a-Aa*, mean +/- SEM is graphed, n = 5 individual experiments for mouse 1, n=4 individual experiments for mouse 2, * indicated p< 0.0461, **p<0.0063, ****p<0.0001 by one-way ANOVA with pairwise comparisons and Holm-Šídák's *post hoc* test. B) Heat map of

Enrichment Scores using Gene Set Enrichment Analysis on human or murine tumoroids treated with the EZH2 inhibitors GSK126 (G) or EPZ6438 (E) contrasted to vehicle control, or treated with EZH2 inhibitor and IFNγ contrasted to IFNγ alone.

To confirm the direct targets of EZH2 inhibition, we performed ChIPseq on the Patient 1 PDT model treated with vehicle, IFNγ, EPZ6438 or a combination of IFNγ and EPZ6438. We assessed enrichment of chromatin bound to H3K27me3, H3K27ac and H3K4me3 histone marks. We observed that IFNγ treatment increased the number of peaks bound by H3K27me3 and that the peaks were nearly completely ablated by treatment with EPZ6438 (Figure 4.11A, 4.12A+B). Several patterns of transcriptional regulation emerged from this analysis. One pattern was observed at MHC Class II genes and involved a loss of H3K27me3 with EZH2 inhibitor treatment, but only with IFNγ and EZH2 inhibitor together did the loci produce transcript (Figure 4.11B). Another pattern was that IFNγ alone increased H3K27me3, H3K27ac, H3K4me3, and gene expression, and EZH2 inhibition with IFNγ boosted gene expression further by reduction of H3K27me3. This happened at loci including the *CXCL9/10/11* cluster (Figure 4.11C). A smaller group of genes, including ALOX15, showed up-regulated transcription when EZH2 was inhibited regardless of IFNγ treatment (Figure 4.11D). ALOX15 is involved in resolving inflammatory states and therefore may be able to reduce a pro-tumor inflammatory environment[121]. Lastly, there were genes including *IL1B* that were on in the vehicle control cells, and transcriptionally turned off by EZH2 inhibition, despite loss of H3K27me3 at the loci (Figure 4.11E). Given that IL1B is a known driver of myeloid cell recruitment and immunosuppression[122], a decrease in its expression could lead to more effective T cell responses.

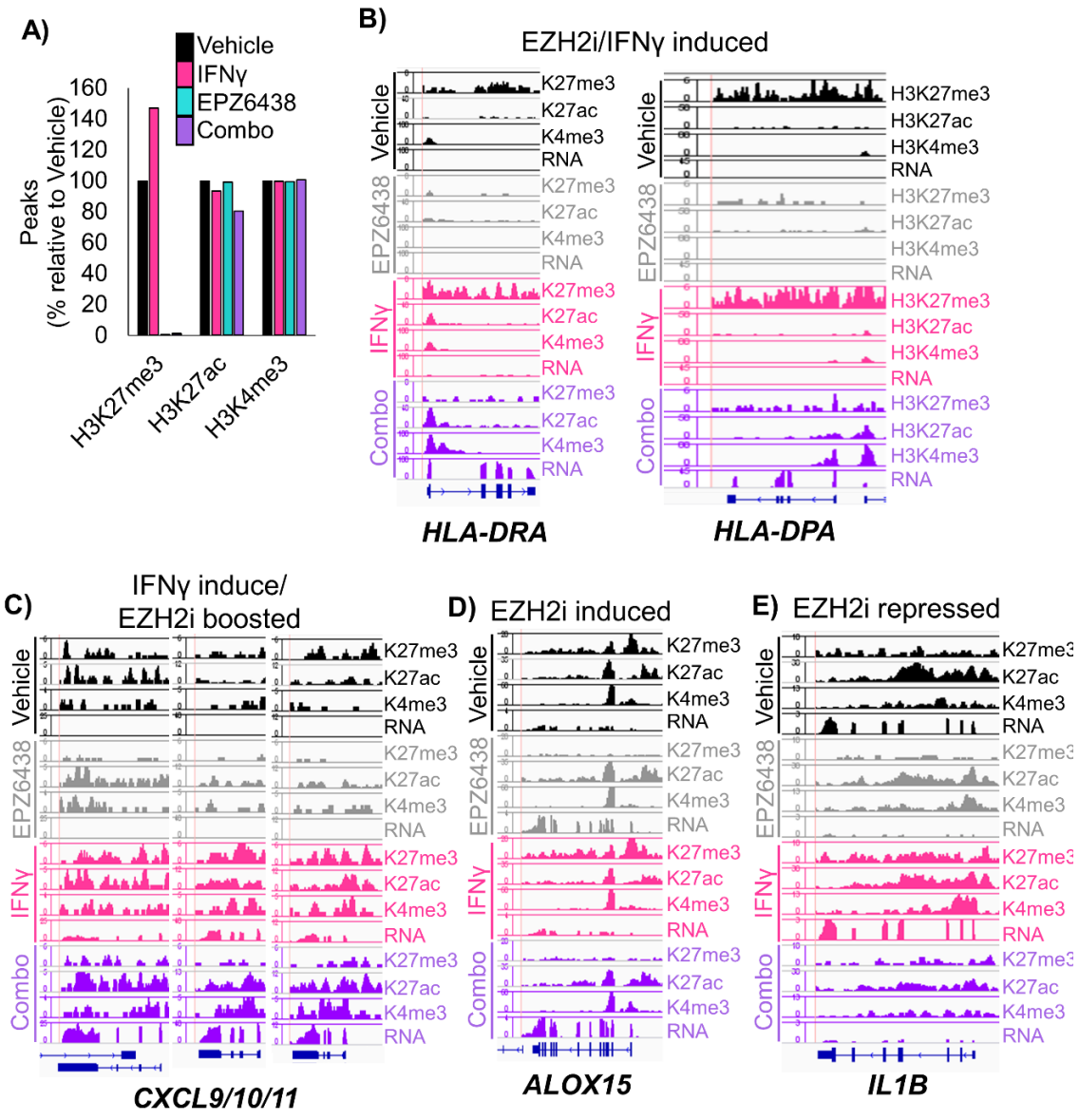

Figure 4.11 ChIP-sequencing of human patient-derived organoids confirms direct regulation of MHC and pro-T cell cytokines by EZH2

A) Peaks called at FDR 1E-7 for ChIP-seq using the chromatin marks H3K27me3, H3K27ac, and H3K4me3 in patient-derived tumoroids from the indicated treatment groups. B-F) Wiggle plots for H3K27me3, H3K27ac, and H3K4me3 histone mark enrichments, and matched RNAseq tracks in patient-derived tumoroids from the indicated treatment groups for the genes: B) *HLA-DRA, HLA-DPA* C) *CXCL9/10/11* D) *ALOX15* E) *IL1B*

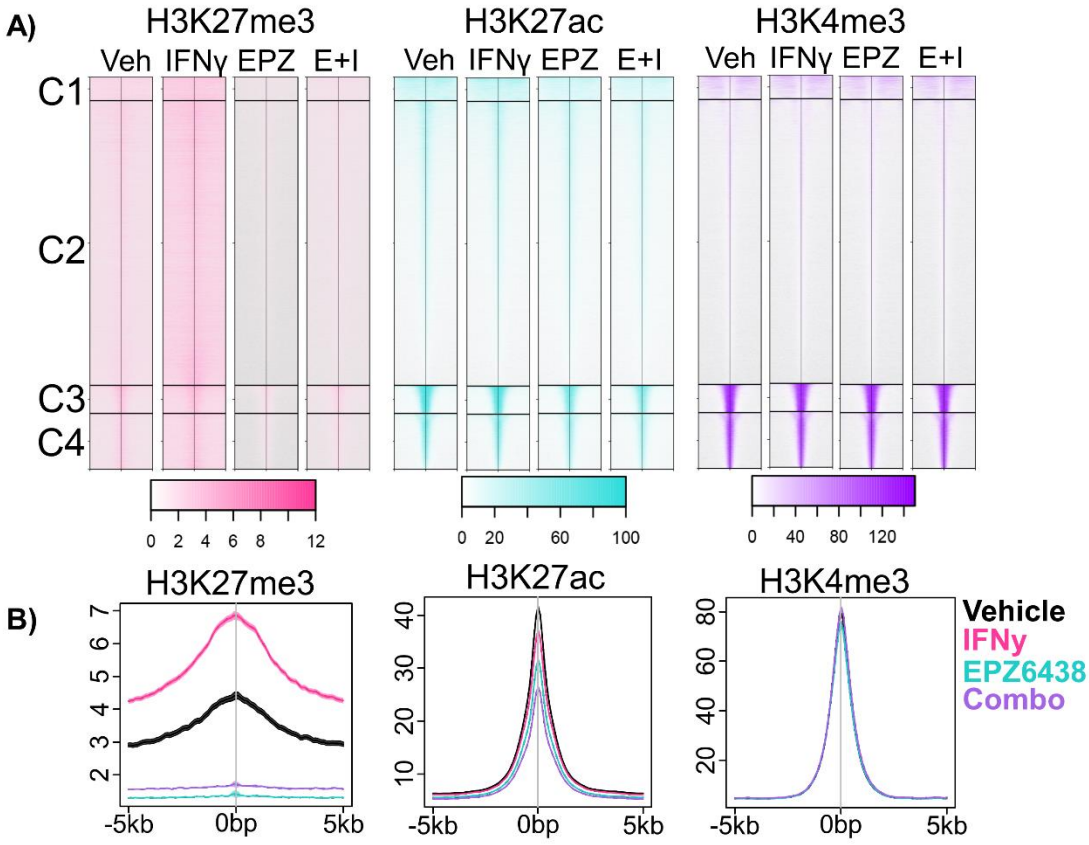

Figure 4.12: Global methylation and acetylation at specific residues on histone 3

A) Heatmap representation of H3K27me3-, H3K27ac- and H3K4me3-bound chromatin peaks centered across a ±5kb window that shows occupancy in tumoroids cultures of the indicated treatments. B) Histogram of merged ChIP-seq peaks in the indicated 3D tumoroid samples.

4.4 Treatment of lung squamous cell carcinoma tumor-bearing mice with EZH2 inhibitor and anti-PD1 results in strong tumor control

To study the effects of EZH2 inhibition in combination with immunotherapy *in vivo*, we induced tumors to grow in the lungs in *Lkb1/Pten* mice by adeno-Cre inhalation and randomized mice into four treatment arms. We treated mice for 4 weeks and then performed magnetic resonance imaging of the thoracic cavity at baseline, 2 weeks, and 4 weeks to quantify lung tumor burden (Figure 4.13A). Consistent with *LKB1* mutation predicting poor response to immunotherapy[118-120], anti-PD1 treatment alone had only a small impact on tumor growth (Figure 4.13B). In contrast, treatment of mice with the EZH2 inhibitor GSK126 showed excellent tumor control with some tumor regression, and treatment with EZH2 inhibitor and anti-PD1 lead to significant tumor regression in all mice tested (Figure 4.13B). Although these results were exciting, the experiments did not use the newly FDA-approved EZH2 inhibitor tazemetostat. In order to test tazemetostat in a faster and more cost-effective system, we established a syngeneic graft model by injecting Lkb1/Pten tumoroids into the parental mouse strain. By nuclear phenotyper, we observed that the tumor from this graft model closely resembled those in the autochthonous model, including the predominant infiltration of neutrophils (Figure 4.14A). After 14 days of treatment, tumors treated with EPZ-6438 alone had not increased in volume, and combination treated tumors grew initially, but began to regress at day 9, and ended with lower tumor volumes than EZH2 inhibition alone (Figure 4.14B).

The marked efficacy of EZH2 inhibition alone in both the autochthonous model and graft models were somewhat surprising, and lead us to compare to EPZ6438 response *in vitro*. By normalized cell counts, there were significant reductions in cultures treated with EPZ6438 and IFNγ compared to vehicle control only in Mouse 2 and Patient 2 (Figure 4.15A). Furthermore, for the Mouse 2 tumoroids used for the *in vivo* grafts, viability measurements also suggested that EPZ6428 itself has no effect on viability (Figure

4.15B), which implies that the tumor control seen in vivo in response to EPZ6438 alone is due almost entirely to immune response. In order to better understand the cell types present, grafts from each treatment arm were dissociated and analyzed by flow cytometry for a panel of immune cell markers (Figure 4.14C-G). Consistent with our *in vitro* data, tumors in mice treated with both EZH2 inhibitor and anti-PD1 had a significant increase in MHC Class II IA/IE positive cells, with a smaller less significant increase in PD-L1 positive cells (Figure 4.14C). Tumor cells also showed higher level of H2-K^d,D^d, particularly in the EZH2 single agent treated tumors (Figure 4.14D). With this flow cytometry panel, we were also able to validate the binding of the anti-PD1 antibody to PD1 positive CD4 and CD8 positive cells. Interestingly, T cells in the EZH2 inhibitor with anti-PD1 treated mice had higher percentages of PD1+ cells bound to antibody than anti-PD1 only treated mice (Figure 4.14E). Although total T cell proportions were not different, there was a significant increase in CD8+ T cells in combination treated mice compared to placebo (Figure 4.14F). There was also a trend towards fewer CD11B+/Ly6G+ or Ly6G+/F4/80- tumor-associated neutrophils, but these differences did not reach significance. One population that was significantly increased in the combination treated mice relative to all other cohorts was a Ly6G+/F4/80+ myeloid cell (Figure 4.16 A+B).

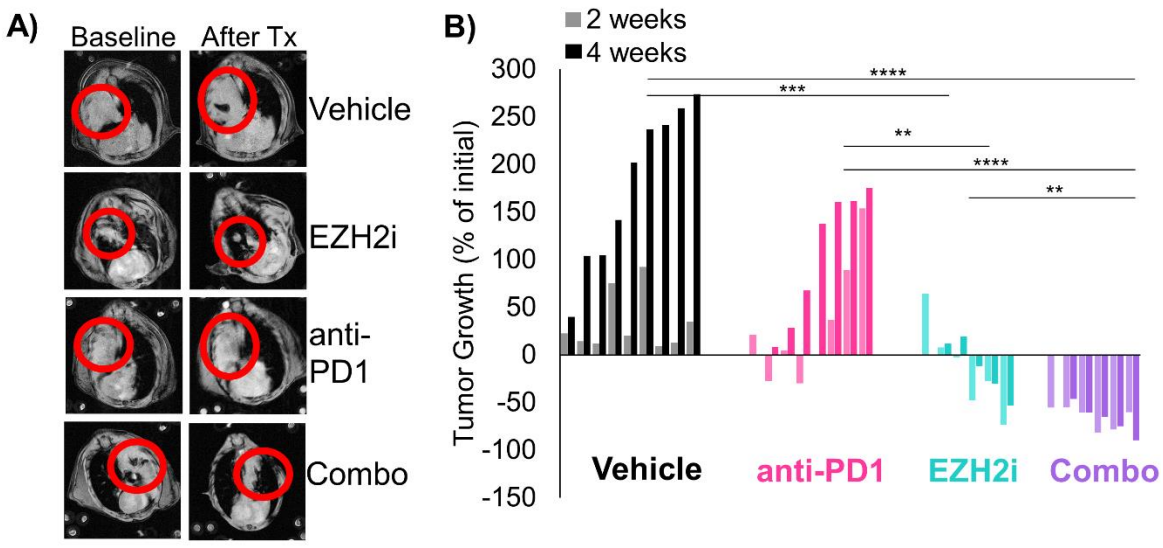

Figure 4.13: EZH2 inhibition alone as well as combined with immunotherapy demonstrates robust tumor control

A) Representative MRI scans of autochthonous mice from each treatment arm at baseline and after treatment. B) Waterfall plot showing change in tumor volume for each mouse on all treatment arms, **** indicates p<0.0001, *** indicates p<0.001, ** indicates p<0.01, * indicates p<0.05 by one-way ANOVA with multiple comparisons and Holm-Šídák's *post hoc* test on log2-transformed values.

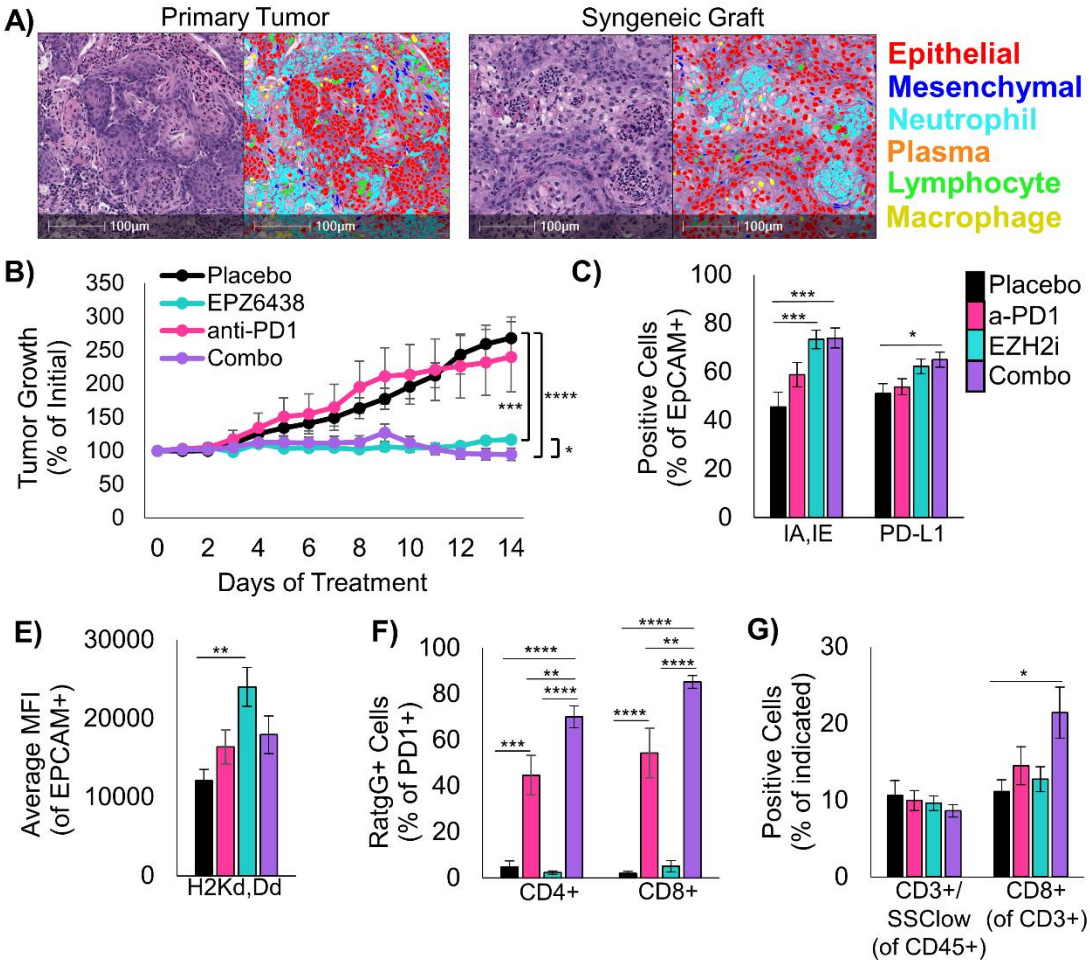

Figure 4.14: A syngeneic model of murine LSCC recapitulates primary tumor and responds well to EZH2 inhibition alone and combined with ant-PD1 therapy

A) H&E and HALO nuclear phenotyper images showing the cells within an autochthonous *Lkb1/Pten* tumor and a syngeneic graft seeded from *Lkb1/Pten* tumoroids. B) Percentage tumor growth from the syngeneic mouse model during 14 days of indicated treatments. *** indicates p=0.0004, **** p<0.0001 by one-way ANOVA with multiple comparisons and Holm-Šídák's *post-hoc* test, * indicates p=0.042 by two-tailed t test on log2-transformed values, Mice/tumors n are placebo=4/8, EPZ6438=5/8, anti-PD1=6/8, combo=5/9, mean +/- s.e.m. is plotted. C) Flow cytometry analysis of dissociated tumors from the syngeneic grafts from the indicated treatment arms at day 14. Percentage of EpCAM+ cells

expressing IA/IE or PD-L1 are graphed, mean +/- s.e.m. is plotted, placebo n=7, EZH2 inhibitor n=7, anti-PD1 n=8, combo n=7 with 2 experimental replicates each, *** indicates p= 0.0350, ***p= 0.0008 by one-way ANOVA with multiple comparisons and Holm-Šídák's *post-hoc* test. D) From the same tumor grafts, MFI for $H2K^d$,D^d in the EpCAM+ cells is graphed, mean +/- s.e.m. is plotted, n=7, EZH2 inhibitor n=7, anti-PD1 n=8, combo n=7 with 2 experimental replicates each, ** indicates p=0.0015, by one-way ANOVA with multiple comparisons and Holm-Šídák's *post-hoc* test. E) From tumor grafts, PD1+/CD3+/CD4+ cells and PD1+/CD3+/CD8+ were gated and percentage of cells bound to Rat-IgG2A antibody are graphed, mean +/- s.e.m. is plotted, n=6, EZH2 inhibitor n=6, anti-PD1 n=7, combo n=7, ** indicates p<0.0052, ***p= 0.0001, **** p<0.0001 by one-way ANOVA with multiple comparisons and Holm-Šídák's *post-hoc* test. F) From the grafts, percentage of CD3+ cells within the CD45+/SSClow fraction and percentage of CD8+ cells withing the CD3+ fraction were graphed, n=8, EZH2 inhibitor n=8, anti-PD1 n=9, combo n=7 with 2 experimental replicates each, * indicates p=0.0197, **** p<0.0001 by one-way ANOVA with multiple comparisons and Holm-Šídák's *post-hoc* test.

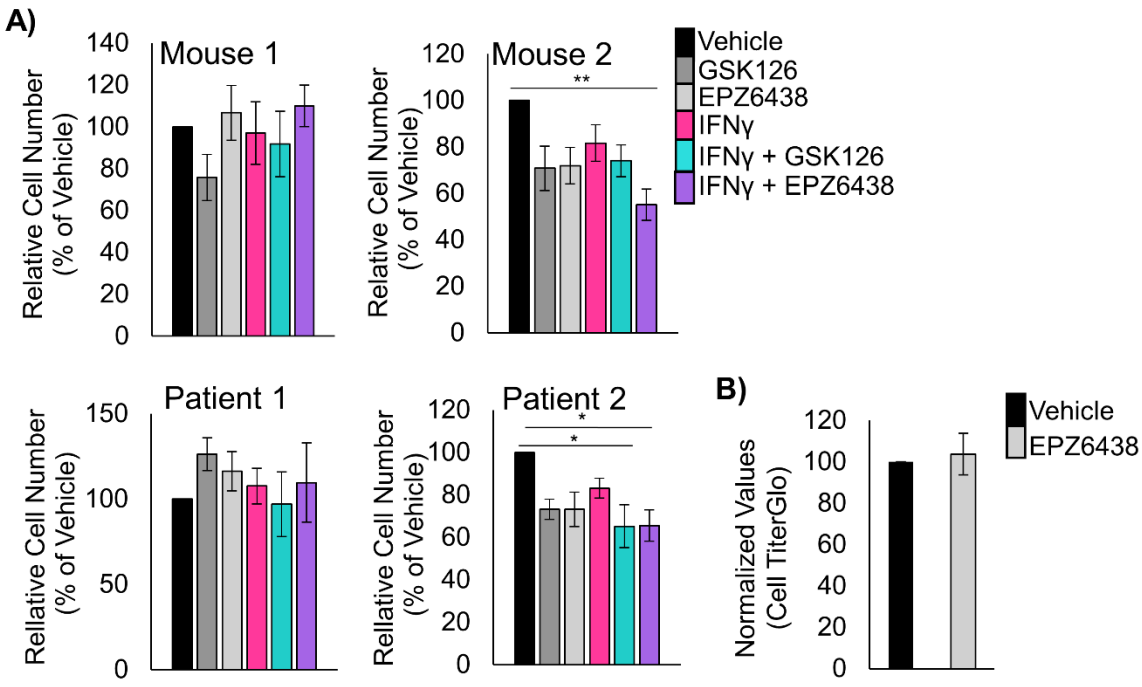

Figure 4.15: Cell viability after treatment with EZH2i

A) Relative counts of cells after dissociation of tumoroids treated with the indicated treatments, mean +/- s.e.m. is plotted, n=4 individual experiments for the human tumoroids, n=7 experiments for mouse 1 and n=5 experiments for mouse 2, * indicates $p<0.0250$, **$p = 0.0048$ by one-way ANOVA with multiple comparisons and Holm-Šídák's *post-hoc* test. B) Relative luminescence from CellTiter Glo assayed tumoroid cultures treated with vehicle or EPZ6438, mean +/- s.e.m. is plotted, n=4 individual experiments.

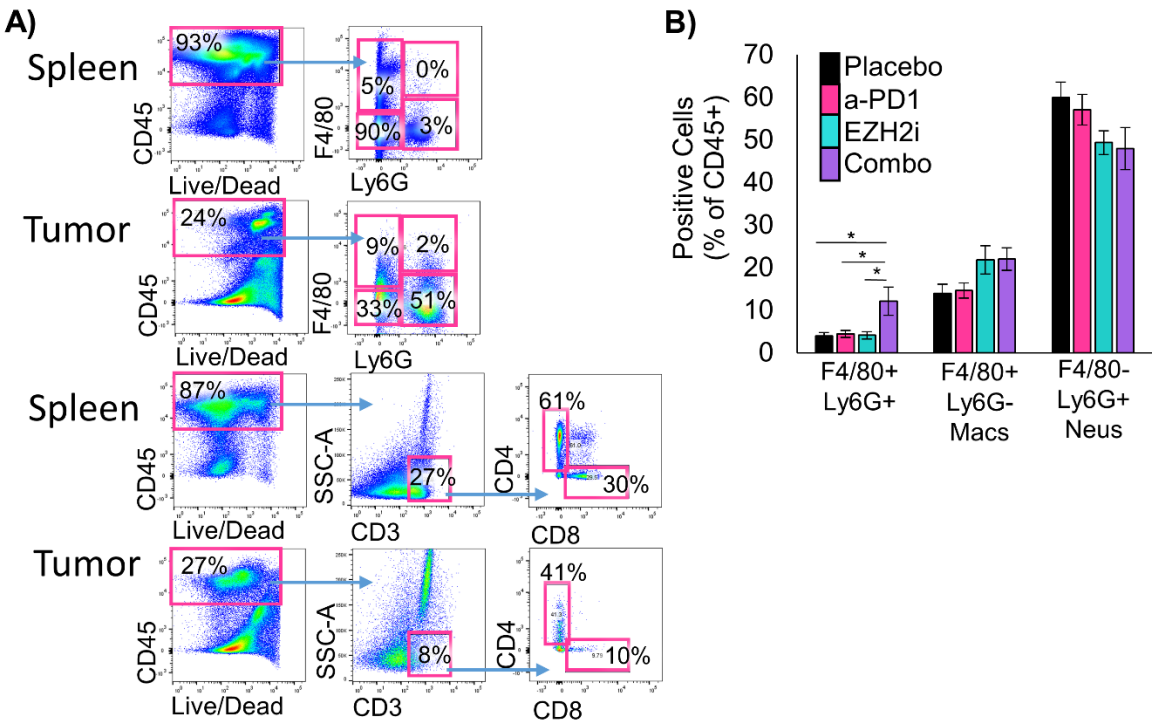

Figure 4.16 Flow cytometry reveals increased populations of neutrophils expressing macrophage lineage marker

A) Representative flow cytometry plots with the indicated samples and markers. The left plots are gated on FSC/SSC and Live/Dead. Spleen samples are shown as staining controls. B) Flow cytometry analysis of dissociated tumors from the syngeneic grafts from the indicated treatment arms at day 14. Percentage of CD45+ cells expressing F4/80 or Ly6G are graphed, mean +/- s.e.m. is plotted, placebo n=8, EZH2 inhibitor n=8, anti-PD1 n=9, combo n=7, * indicates $p<0.0112$, by one-way ANOVA with multiple comparisons and Holm-Šídák's *post-hoc* test.

4.5 Tumor profiling and single cell RNA-sequencing confirm mechanisms through which EZH2 inhibition drives increased tumor immunogenicity

Finally, to assess the transcriptional heterogeneity of cell types in the tumors and how transcriptional programs were changed by treatment, we performed single cell RNA sequencing (scRNAseq). We analyzed fresh autochthonous lung tumors after four weeks of therapy, and also analyzed lungs of mice that were on placebo or EZH2 inhibition that had no tumors as controls. From the tumors and total lungs, we identified 16 unique cell populations that we annotated based on conserved markers (Figure 4.17A+B, Supp Table 2). Analysis of cell proportions in each treatment group revealed significant decreases in tumor cells and some macrophage and neutrophil populations, and significant increases in T cells, cycling cells, normal lung, and some neutrophil populations (Figure 4.17B). Next, we analyzed the differentially expressed genes in three major groups, the tumor cells (malignant epithelial cells), the macrophage and dendritic cells, and the neutrophils. By GSEA, we observed a dramatic decrease in protein synthesis pathways in tumors treated with combination treatment when compared to either single treatment, and increases in DNA pathways, which could reflect cell cycle arrest or DNA damage. Pathways involved in oxidative phosphorylation were upregulated in all three cell populations in the combination treated tumors (Figure 4.18A, Supp Table 3). To understand the individual genes changed by treatment, we also assessed differential expression of each cell type in the treated groups relative to placebo (Figure 4.18B). Tumor cells that were treated with EZH2 inhibitor alone or in combination with anti-PD1 had increased *H2-K1*, *B2m*, and *Ifngr1* expression, and decreased expression of neutrophil-recruiting chemokines such as *Cxcl3*, *Cxcl5*, and *Ppbp* (aka *Cxcl7*). Moreover, macrophage and dendritic cells had increased MHC class II and IFN-response genes, while neutrophils showed upregulation in IFN-response genes in the combo group relative to both EZH2 inhibition and anti-PD1 treatments alone.

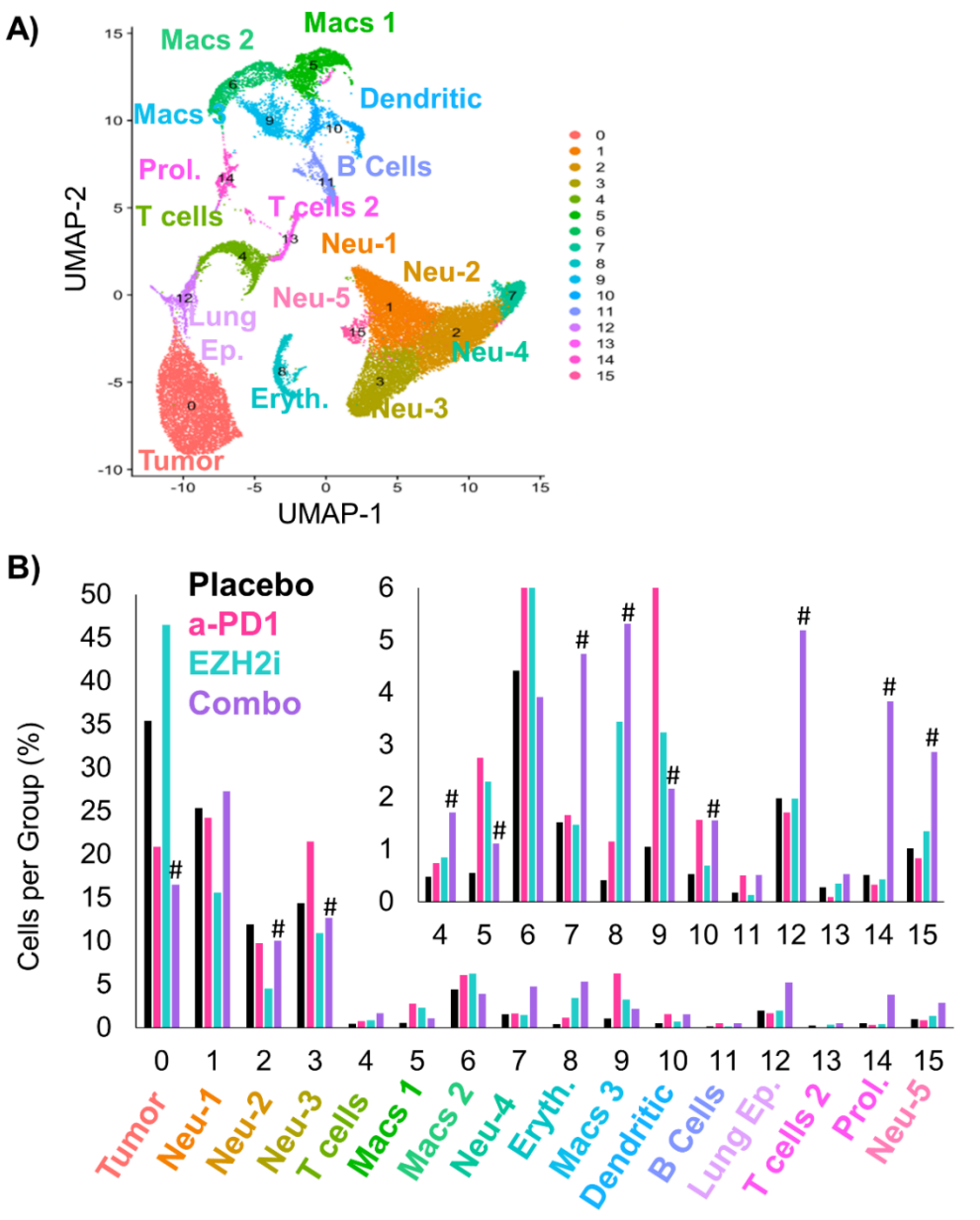

Figure 4.17: scRNAseq reveals cell subsets within the TME in LSCC after treatment with EZH2i and anti-PD1 immunotherapy

A) Annotated Uniform Manifold Approximation and Projection (UMAP) plot showing the 16 different populations within lung tumors of the *Lkb1/Pten* model of LSCC after treatment with placebo, GSK126, anti-PD1, or combined GSK126 with anti-PD1. B) Percentage of cells per treatment group graphed for all populations, # indicates adjusted p<0.01 by proportion z-test.

It was surprising that the neutrophil populations remained predominant in tumors treated with EZH2 inhibition and immunotherapy, given the large amount of data suggesting that neutrophils prevent proper immunotherapy response. Therefore, we next interrogated the differential gene expression profiles of the five identified neutrophil populations (Figure 4.18C, Supp Table 4). Based on the literature [44], we believe that there are three populations of neutrophils in our data set that appear to promote tumor elimination. These three populations, Neu1, Neu4, and Neu5, express genes such as *Tnf*, *Cxcl10*, and multiple IFN-response genes. Interestingly, we observed increases in these populations in the group treated with the combined therapy. Moreover, we saw significant decreases in Neu2 and Neu3 populations, which we believe to be immunosuppressive. These two populations express genes *Cxcl3*, *Ccl3*, *Ccl4, Atp6v1c1*, *Atp6v0d2*, which have been associated with a tumor promoting phenotype. However, Neu3 also has an MHC class II antigen presentation gene (*H2-Eb1*), suggesting it may be a 'hybrid' tumor promoting and tumor eliminating phenotype.

Demonstrating a conservation among models, genes bolded in our figure correspond to genes identified by other groups in neutrophil populations from lung cancers by scRNAseq [47, 48, 59]. In order to understand if neutrophils were also altered in the bone marrow when EZH2 inhibitor was administered, we performed cytospin of isolated neutrophils from the same mice that were used for scRNAseq. By nuclear phenotype, there was a dramatic shift towards a more mature phenotype in both the EZH2 only and combination treated mice compared to those with vehicle or anti-PD1 treatment (Figure 4.19A). Similarly, bone marrow cells isolated from the syngeneic graft-bearing mice treated with EZH2 inhibitor were more apoptotic, suggesting a more mature phenotype Figure 4.19B). Together these data show a systemic shift in neutrophil identity away from a less mature myeloid suppressor cell phenotype towards a more mature tumor

eliminating phenotype and suggests that neutrophils can be compatible with immunotherapy in the right contexts.

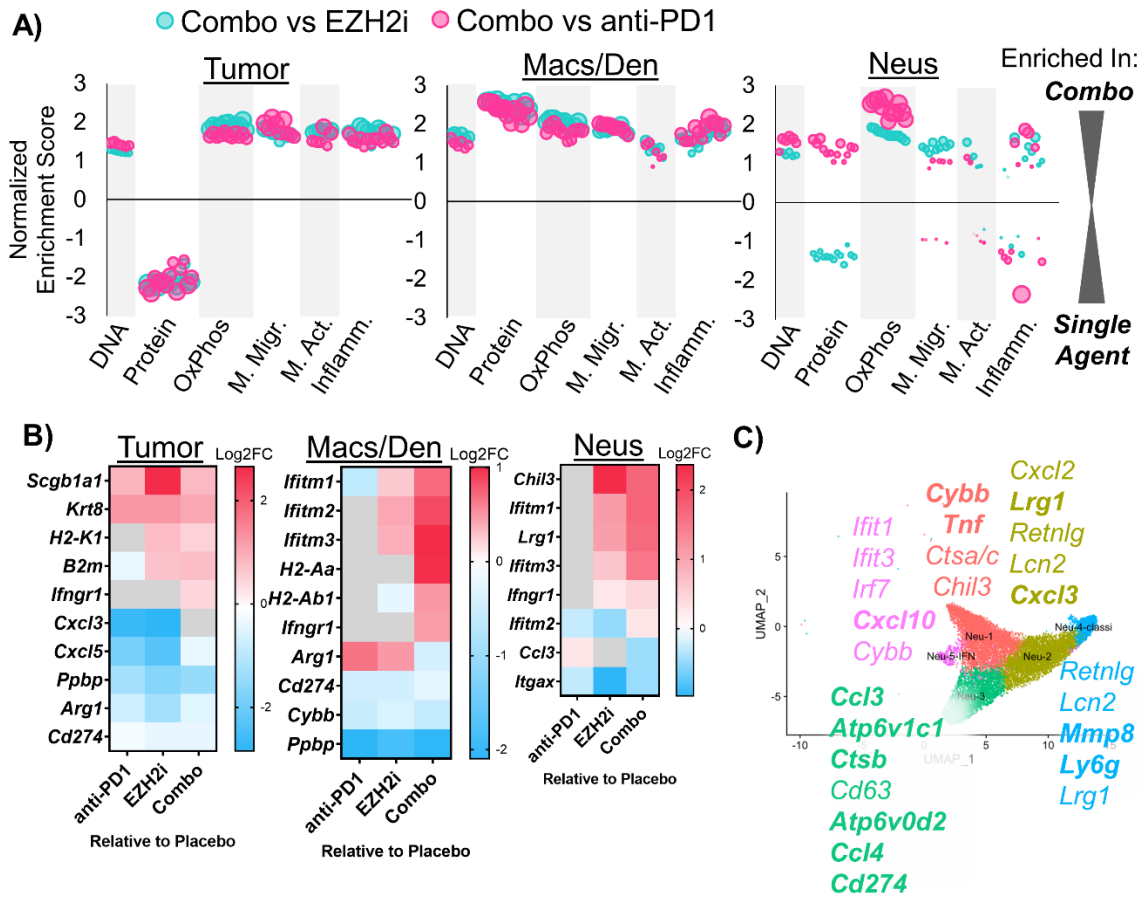

Figure 4.18: Single Cell RNA sequencing highlights neutrophil heterogeneity shifts in response to EZH2 inhibition combined with ICI

A) Gene Set Enrichment Analysis depicting gene sets that are enriched or depleted in Tumor, Macrophage/Dendritic Cells, or Neutrophils in mice treated with EZH2 inhibitor and anti-PD1 contrasted with either treatment alone. Normalized Enrichment Scores are plotted and bubble sizes estimate -log(false discovery rate). See also Supp. Table 2. B) Heat maps showing differentially expressed genes among tumor, macrophages and dendritic cells, and neutrophils between GSK126, anti-PD1, and combination treated mice compared to placebo on the log2 fold change. C) UMAP of 5 neutrophil populations showing selected genes that are highly expressed in each cluster.

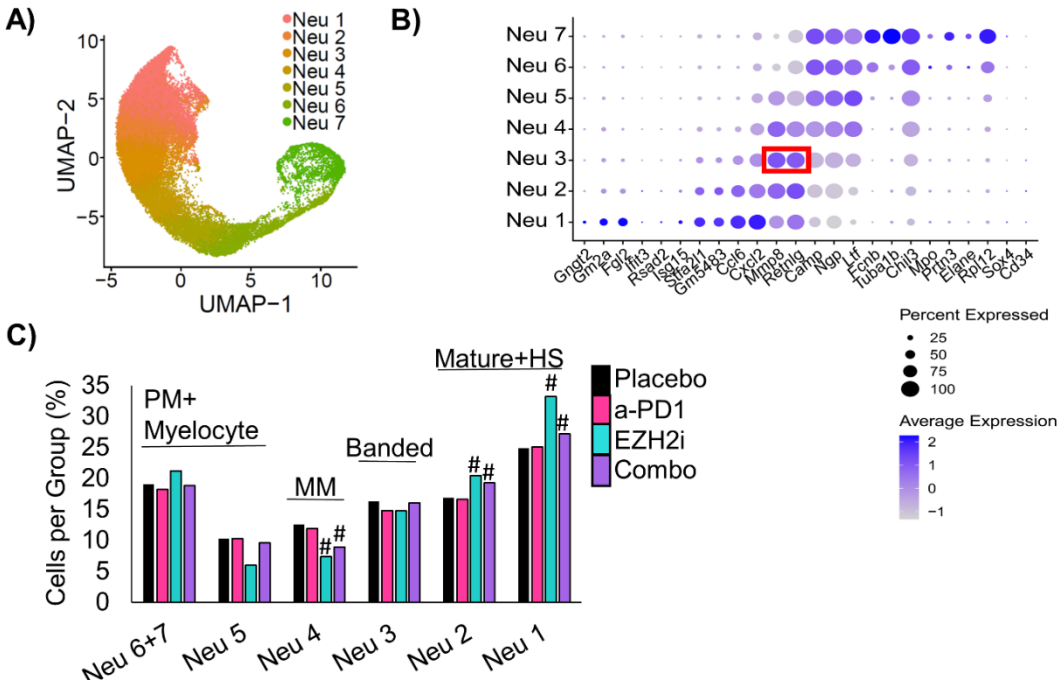

Figure 4.18: Heterogeneity of neutrophils populations following EZH2 inhibition plus immunotherapy.

A) Annotated Uniform Manifold Approximation and Projection (UMAP) plot showing the 8 different populations of neutrophils within the bone marrow of tumor-bearing mice treated with placebo, GSK126, anti-PD1, or combined GSK126 with anti-PD1. B) Dot plot showing the relative expression of marker genes (x-axis) in each neutrophil cluster (y-axis). Expression of *Mmp8* and *Rentlg* were shown to be enriched in banded neutrophils. C) Percentage of cells per treatment group graphed for the neutrophil populations, # indicates adjusted p<0.008 by proportion z-test

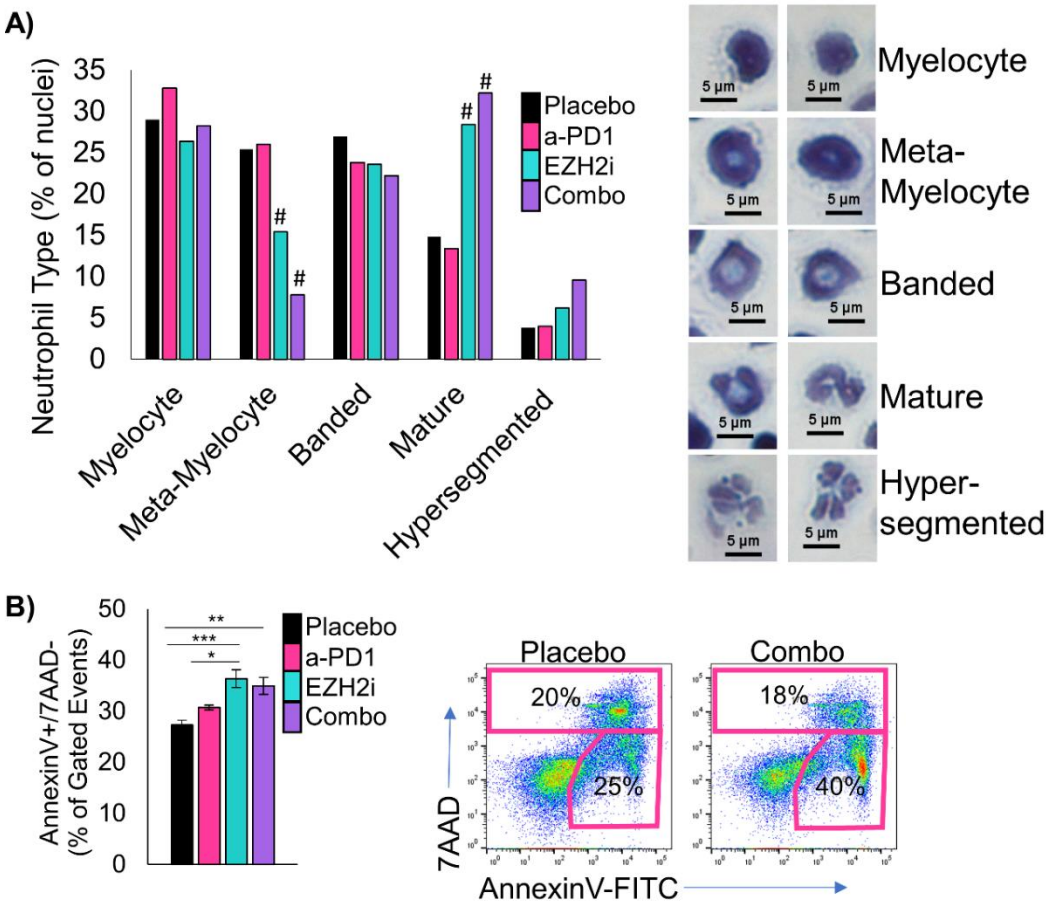

Figure 4.19: Neutrophil morphology after treatment with EZH2i and anti-PD1 ICI

A) Proportions of different nuclear morphologies in bone marrow cytospins, average of n=2 samples for Placebo, n=1 sample for others, 500 nuclei were counted, # indicates Fisher's Exact test between Vehicle and EZH2 inhibitor or Vehicle and Placebo for meta-myelocyte vs mature neutrophils. Representative images of nuclei types shown, scale bar = 5µm. B) Percentage of AnnexinV+/7AAD- cells in bone marrow cultures 48 hours post isolation from mice treated with the indicated therapies, n=3 biological replicates each with 2 experimental replicates for placebo, EPZ6438 and combo, n=4 biological replicates each with 2 experimental replicates for anti-PD1, * indicated p=0.01, **p=0.0017, ***p= 0.0003 by one-way ANOVA with pairwise comparisons and Holm-Šídák's *post hoc* test. Representative flow plots of placebo and combination treated cultures shown.

CHAPTER 5. DISCUSSION

While there are many methods to investigate the TME, some of these methods are expensive, time consuming, and often destroy the sample in the process of data generation. In the first study we present utilizing a HALO® AI nuclear phenotyper algorithm to examine the TME in NSCLC. This method boasts low overall costs, quick turnaround, and the ability to retain the original sample. Using both human and mouse histology samples, we were able to demonstrate the algorithm's ability to identify varied TME cell types, validating it as a tool for researchers and also as a potential clinical tool for the selection of appropriate treatments. Using GEMMS that have known immune cell tropisms, we confirmed that the nuclear phenotyping algorithm works very well to define the neutrophil and macrophage populations in lung cancer. This is one of the many ways in which this software can be used to differentiate between the microenvironments of these subtypes of NSCLC. We further confirmed the efficacy of the algorithm by assessing lymph node sections, comparing the algorithm's results to a more traditional IHC staining for CD3. The algorithm performed very well with each of these known data-sets and was able to provide additional information about the abundant cell types in the GEMMs examined.

In a patient sample tissue microarray, the AI nuclear phenotyper provided a rapid and simple way to study the correlation of the different cell types at the tumor site. Our data demonstrate that neutrophils and lymphocytes are highly negatively correlated in human NSCLCs. This finding is in agreement with fresh patient tissue flow cytometry, which demonstrated that neutrophils are negatively correlated to CD8+ T cells [123]. Given that CD8+ T cells are responsible for the elimination of malignant epithelial cells in immunotherapy contexts, a high neutrophil/low lymphocyte tumor may not respond well to immunotherapy, and this appears to be the case in patient samples [116]. Furthermore,

we show a strong negative correlation between mesenchymal cells and lymphocytes, and this is an additional avenue that could be explored for immunotherapy response. Lastly, we observed a large number of plasma cells in NSCLCs, and recent reports have demonstrated that plasma cells may have a negative correlation to survival in lung cancer patients [52, 124]. This further emphasizes both the importance of this program as a tool for researchers to understand the function of the TME, and the potential of this method to help determine patient treatment strategies. This easy-to-implement approach allows for specific understanding of the TME at the site of the tumor itself, and has potential to allow researchers to further investigate how abundance of different cell types influences the efficacy of therapies.

The data described here do not represent the first instance where AI has been suggested as a potential prognostic technique for histopathology. In fact, it has been predicted that AI will become a useful, if not necessary, tool for pathologists to triage slide analysis, quantify phenotypes and even to predict genetic alterations [125, 126]. However, there remain concerns about the ability of AI techniques to accurately differentiate between histopathologies, particularly if the algorithm was not trained on certain distinct patterns. Among proponents of the AI, it is widely accepted that the rigor of these algorithms will need to be tested abundantly to prove that their efficiency is equal to that of a pathologist before they are implemented as a prognostic technique [126]. Therefore, the immediate implications of this technique are to allow translational research to begin to adopt this technique while further clinical validation is ongoing. While we specifically study NSCLC, we believe this artificial intelligence-based cell detection algorithm will have wider utility in many other diseases characterized by heterogenous chronic inflammation.

In the second study we demonstrate that in both 2D and 3D *in vitro* models, treatment with EZH2 inhibition and IFNγ led to increases in MHC I/II and pro-inflammatory cytokine

expression. In 3D patient-derived tumoroids, ChIPseq confirmed a switch from repressive to active chromatin at these genes in response to treatment. Next, we employed both autochthonous and syngeneic models of LSCC driven by biallelic deletion of the tumor suppressors *Lkb1* and *Pten*. We observed significant tumor control in both the anti-PD1 with EZH2i combination, as well as EZH2i alone. Using scRNAseq and immune cell profiling, we identified increases in MHC I/II expression and a shift towards tumor-eliminating neutrophils within tumors. Several studies have found that IFNγ, CXCL9 and PD-L1 expression in tumor specimens correlate to stronger immunotherapy responses. In this study, we found that CXCL9/10/11 are strongly induced by a combination of IFNγ and EZH2 inhibition in both human and murine tumoroids, and that this cluster of chemokine genes is a direct PRC2 target in human cells. Our data mirror those seen in urothelial cells. In addition, *Arg1* was significantly downregulated in autochthonous tumors treated with EZH2 inhibition, leading to less arginase expression which inhibits T-cell responses. Lastly, we found that neutrophil populations shifted towards IFNγ-responsive and TNFα expressing populations. These data point to multiple overlapping mechanisms through which T cells can be recruited to tumors to turn 'cold' tumors 'hot' (Figure 4.20).

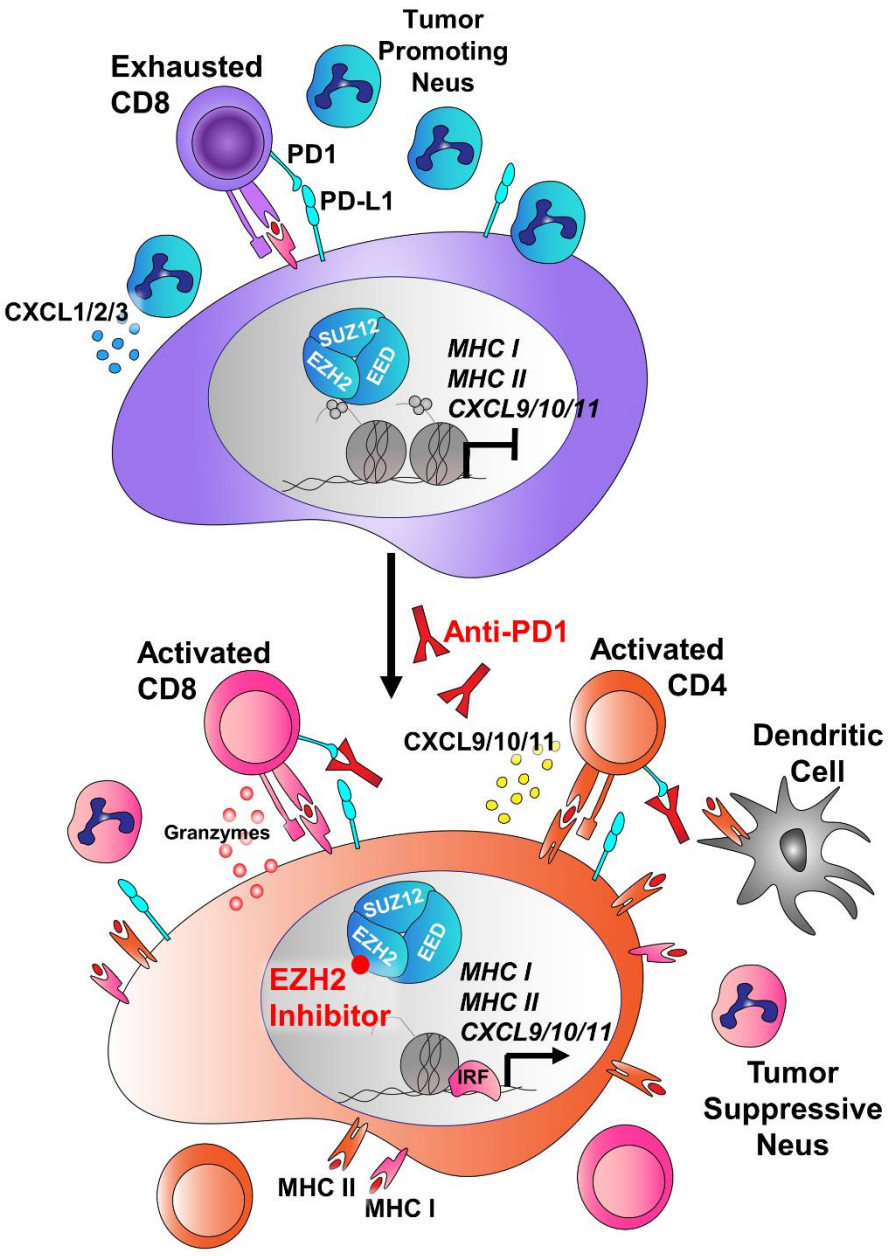

Figure 4.20: Schematic of tumor cell-intrinsic and microenvironmental consequences of EZH2 inhibition that boost immunotherapy response in LSCC

In LSCC, tumors can evade the immune system through expression of PD-L1, inhibiting T cell activation. In addition, these tumors secrete high levels of CXCL1/2/3 (mouse orthologs Cxcl3/5/7) that attract T-cell suppressive neutrophils, and can express high levels of Arginase, that further drive T cell suppression. In response to EZH2 inhibition, the tumors up-regulate MHC Class I and Class II potentially improving antigen

presentation, and switch from expression of *CXCL1/2/3* to expression of the T cell promoting chemokines *CXCL9/10/11* and the inflammatory resolution molecule ALOX15. *IL1B* and *Arg1* are downregulated, and the neutrophils surrounding the tumor take on more tumor-repressive phenotypes. When anti-PD1 antibody is added, the net result is tumor regression through immune targeting of tumor cells.

In addition to strongly influencing the tumor immune microenvironment, EZH2 inhibition drove dramatic increases in expression of both MHC class I and class II. Several studies have also observed that EZH2 plays a major role in repression of MHC class I in small cell lung cancer and class II in urothelial and AML cancers. Furthermore, class II expression has proven to correlate well with increased ICI response rates in melanoma. While anti-PD1 ICI is thought to activate CD8 T cells to target the tumor through MHC class I interactions, CD8+ T cells can kill MHC class II positive cells though FAS/FASL interactions. Again, these data suggest not one but multiple mechanisms through which EZH2 inhibition can alter both tumor cells and immune cells for a net effect of increased tumor immunogenicity. This multi-mechanism aspect may help to delay or prevent acquired resistance phenotypes that occur readily when only one molecular pathway is altered.

Importantly, the model we used is deficient for LKB1, which is correlated with immunotherapy resistance. However, the majority of data are in non-squamous histology tumors. Our data suggest that when a tumor is squamous in epigenetics state, that EZH2 inhibition combined with immunotherapy will be an effective treatment approach regardless of tumor genotype. What is less clear is whether tumors that are adenocarcinoma in histology will respond as effectively, and therefore more research is needed. MHC class I and class II expression are intrinsic properties of specific alveolar and bronchiolar lung cells. Therefore, these molecules may already be expressed in

adenocarcinomas, depending on the tumor cell-of-origin. We also focused on models with significant neutrophil infiltration. Our recent study of human lung cancers showed that macrophages and plasma cells can also predominate in tumors, and it will be important to test EZH2 inhibition in the context of diverse TIMEs moving forward.

One aspect of immunotherapy response that was not addressed in the current study is the role of tumor mutation burden (TMB). In general, genetically engineered mouse models are thought to have relatively low TMB. Therefore, one question is what are the neoantigens that the tumor was presenting that allowed for effective recognition and clearance. Future studies should work to understand if EZH2 inhibition drives genomic instability that increases TMB. The effect of EZH2 inhibition in models with varied TMBs would also be worthwhile. Despite this limitation, this work demonstrates several mechanisms through which EZH2i can boost ICI responses in lung cancer. The EZH2i tazemetostat was recently FDA approved and is already in clinical trials with ICIs for urothelial tumors. Importantly, these data suggest that EZH2i plus ICI, or EZH2i alone could be viable options specifically for lung SCC, and these data serve as strong premise for clinical investigation. Lastly, the model systems we have characterized will be useful tools to explore further mechanisms of ICI response and resistance.

APPENDIX

Supplemental Table 1: GSEA on RNAseq of Tumoroids, related to Figure 4.10B

NES=Normalized Enrichment Score, FDR=False Discovery Rate

MSigDB Signature Name	Patient 1		Patient 2		Patient 1		Patient 2	
	GSK126 vs Veh		*GSK126 vs Veh*		*EPZ6438 vs Veh*		*EPZ6438 vs Veh*	
	NES	FDR q-val	NES	FDR q-val	NES	FDR q-val	NES	FDR q-val
HALLMARK_MYC_TARGETS_V1	-2.274	0.000	-2.505	0.000		1.000	-2.127	0.000
HALLMARK_MYC_TARGETS_V2	-1.482	0.079	-1.940	0.014	-1.711	0.017	-1.743	0.026
HALLMARK_DNA_REPAIR	-1.356	0.085	-1.413	0.097	-0.833	0.644	-1.207	0.217
HALLMARK_UNFOLDED_PROTEIN_RESPONSE	-1.360	0.096	-1.273	0.160	-1.542	0.039	-1.142	0.268
HALLMARK_E2F_TARGETS	-0.922	0.688	-1.357	0.117		1.000	-0.632	0.966
HALLMARK_REACTIVE_OXYGEN_SPECIES_PATHWAY	-1.868	0.008	-1.594	0.058	-1.818	0.007	-1.625	0.035
HALLMARK_OXIDATIVE_PHOSPHORYLATION	-2.657	0.000	-2.152	0.000	-2.161	0.004	-2.125	0.000
HALLMARK_INFLAMMATORY_RESPONSE	1.501	0.025	0.821	0.927	1.242	0.183	-1.659	0.036
HALLMARK_INTERFERON_GAMMA_RESPONSE	1.273	0.164	0.999	0.793	1.479	0.036	0.639	1.000
	GSK+IFN vs IFN		*GSK+IFN vs IFN*		*EPZ+IFN vs IFN*		*EPZ+IFN vs IFN*	
	NES	FDR q-val	NES	FDR q-val	NES	FDR q-val	NES	FDR q-val
HALLMARK_MYC_TARGETS_V1	-1.753	0.024	-2.284	0.000	-1.801	0.026	-2.111	0.000
HALLMARK_MYC_TARGETS_V2	-1.527	0.062	-2.244	0.000	-1.637	0.051	-2.139	0.000
HALLMARK_DNA_REPAIR	-1.064	0.420	-1.540	0.069	-1.121	0.361	-1.419	0.117
HALLMARK_UNFOLDED_PROTEIN_RESPONSE	0.892	0.977	-0.829	0.814	0.716	1.000	-0.648	0.965
HALLMARK_E2F_TARGETS	-1.001	0.478	-1.530	0.054	-0.480	1.000	-0.730	0.984
HALLMARK_REACTIVE_OXYGEN_SPECIES_PATHWAY	-1.763	0.032	-1.321	0.149	-1.806	0.038	-1.398	0.096
HALLMARK_OXIDATIVE_PHOSPHORYLATION	-2.091	0.002	-1.393	0.107	-2.064	0.000	-1.557	0.067
HALLMARK_INFLAMMATORY_RESPONSE	1.503	0.036	0.882	0.934	1.178	0.421	-1.413	0.100
HALLMARK_INTERFERON_GAMMA_RESPONSE	1.722	0.002	1.066	0.698	1.385	0.118	0.912	1.000
	Mouse 1		**Mouse 2**		**Mouse 1**		**Mouse 2**	
	GSK126 vs Veh		*GSK126 vs Veh*		*EPZ6438 vs Veh*		*EPZ6438 vs Veh*	
	NES	FDR q-val	NES	FDR q-val	NES	FDR q-val	NES	FDR q-val
HALLMARK_MYC_TARGETS_V1	-1.948	0.001	-1.404	0.086	-1.701	0.089	-1.465	0.092
HALLMARK_MYC_TARGETS_V2	-1.635	0.017	-1.463	0.064	-1.543	0.110	-0.778	1.000
HALLMARK_DNA_REPAIR	-1.572	0.025	-0.815	0.981	-1.542	0.073	-1.315	0.167
HALLMARK_UNFOLDED_PROTEIN_RESPONSE	-1.348	0.112	-1.000	0.690	-1.313	0.178	-0.693	0.931
HALLMARK_E2F_TARGETS	-2.393	0.000	-2.560	0.000	-0.597	0.980	-2.231	0.003
HALLMARK_REACTIVE_OXYGEN_SPECIES_PATHWAY	-1.054	0.424	0.979	0.591	-1.317	0.218	0.695	0.960
HALLMARK_OXIDATIVE_PHOSPHORYLATION	0.534	0.998	0.499	0.999	-1.198	0.258	-0.728	1.000
HALLMARK_INFLAMMATORY_RESPONSE	2.178	0.000	1.233	0.227	1.811	0.000	1.662	0.006
HALLMARK_INTERFERON_GAMMA_RESPONSE	1.772	0.014	1.614	0.032	1.775	0.001	1.811	0.000
	GSK+IFN vs IFN		*GSK+IFN vs IFN*		*EPZ+IFN vs IFN*		*EPZ+IFN vs IFN*	
	NES	FDR q-val	NES	FDR q-val	NES	FDR q-val	NES	FDR q-val
HALLMARK_MYC_TARGETS_V1	-1.618	0.050	-2.248	0.000	-2.003	0.008	-2.443	0.000
HALLMARK_MYC_TARGETS_V2	-2.020	0.007	-2.006	0.000	-1.930	0.007	-1.969	0.005
HALLMARK_DNA_REPAIR	-0.938	0.889	-1.046	0.469	-1.350	0.144	-1.591	0.030
HALLMARK_UNFOLDED_PROTEIN_RESPONSE	-1.559	0.044	-1.936	0.001	-1.732	0.017	-1.955	0.004
HALLMARK_E2F_TARGETS	-1.185	0.458	-2.775	0.000	-1.024	0.392	-2.832	0.000
HALLMARK_REACTIVE_OXYGEN_SPECIES_PATHWAY	-0.911	0.884	0.768	0.945	-1.309	0.143	-0.828	0.799
HALLMARK_OXIDATIVE_PHOSPHORYLATION	0.510	0.998	-0.779	1.000	-1.114	0.294	-1.681	0.023
HALLMARK_INFLAMMATORY_RESPONSE	2.196	0.000	1.512	0.108	1.894	0.000	1.895	0.000
HALLMARK_INTERFERON_GAMMA_RESPONSE	1.888	0.001	1.426	0.121	1.663	0.007	1.937	0.000

Supplemental Table 2: Genes in All 16 Clusters, Related to Figure 4.17A
Log2FC= fold change between cluster and all others, pct=percentage of cells expressing

Cluster	Gene Symbol	Log2FC	pct.1	pct.2	P value	Adj P value	Cluster	Gene Symbol	Log2FC	pct.1	pct.2	P value	Adj P value
Tumor	Krt19	4.685	0.977	0.814	0.0E+00	0.0E+00	**Dendritic**	Cd74	4.390	0.964	0.555	0.0E+00	0.0E+00
	Ppbp	4.050	0.781	0.673	0.0E+00	0.0E+00		H2-Ab1	4.061	0.934	0.629	0.0E+00	0.0E+00
	S100a7a	3.910	0.908	0.872	0.0E+00	0.0E+00		C1qa	3.857	0.988	0.581	0.0E+00	0.0E+00
	S100a10	3.589	0.968	0.700	0.0E+00	0.0E+00		H2-Aa	3.618	0.918	0.556	0.0E+00	0.0E+00
	Ly6d	3.380	0.853	0.767	0.0E+00	0.0E+00		C1qb	3.455	0.982	0.503	0.0E+00	0.0E+00
	Prss27	3.341	0.899	0.825	0.0E+00	0.0E+00		Apoe	3.074	0.985	0.781	0.0E+00	0.0E+00
	Krt18	3.333	0.824	0.698	0.0E+00	0.0E+00		C1qc	2.985	0.988	0.640	0.0E+00	0.0E+00
	Plet1	3.301	0.954	0.684	0.0E+00	0.0E+00		Ms4a6c	2.243	0.930	0.407	0.0E+00	0.0E+00
	Nupr1	3.285	0.892	0.671	0.0E+00	0.0E+00		Ms4a7	2.238	0.969	0.433	0.0E+00	0.0E+00
	S100a16	3.221	0.951	0.730	0.0E+00	0.0E+00		Ctss	1.932	0.990	0.654	0.0E+00	0.0E+00
	Krt23	3.208	0.894	0.638	0.0E+00	0.0E+00		Cst3	1.844	0.987	0.817	0.0E+00	0.0E+00
	Ly6c1	2.943	0.832	0.652	0.0E+00	0.0E+00		Gatm	1.752	0.937	0.517	0.0E+00	0.0E+00
	Atp1b1	2.870	0.888	0.682	0.0E+00	0.0E+00		Lair1	1.530	0.895	0.546	0.0E+00	0.0E+00
	Irf7	2.800	0.937	0.588	0.0E+00	0.0E+00		Pld4	1.525	0.899	0.187	0.0E+00	0.0E+00
	Isg15	2.772	0.869	0.644	0.0E+00	0.0E+00		Tmem119	0.828	0.959	0.256	0.0E+00	0.0E+00
	Tspan1	2.562	0.857	0.516	0.0E+00	0.0E+00		Cxcl9	0.789	0.946	0.644	0.0E+00	0.0E+00
	Hspa5	2.539	0.951	0.818	0.0E+00	0.0E+00		Ccl8	0.651	0.962	0.382	0.0E+00	0.0E+00
	Glrx	2.448	0.869	0.594	0.0E+00	0.0E+00		Retnla	0.821	0.957	0.743	2.9E-289	4.4E-286
	Emp1	2.302	0.920	0.778	0.0E+00	0.0E+00		Cybb	1.677	0.924	0.514	1.9E-288	2.9E-285
	Hopx	2.294	0.766	0.477	0.0E+00	0.0E+00		Gngt2	1.535	0.964	0.637	4.8E-284	7.2E-281
	Cd81	2.276	0.909	0.547	0.0E+00	0.0E+00		Cxcl16	1.511	0.983	0.701	5.4E-279	8.1E-276
	Arg1	2.255	0.872	0.739	0.0E+00	0.0E+00		Fyb	1.709	0.949	0.688	1.7E-277	2.5E-274
	Scgb1a1	2.246	0.831	0.809	0.0E+00	0.0E+00		Pou2f2	1.956	0.849	0.421	1.4E-270	2.1E-267
	Lmo7	2.226	0.849	0.750	0.0E+00	0.0E+00		Acp5	1.404	0.968	0.607	4.2E-268	6.3E-265
	Ceacam1	2.214	0.888	0.649	0.0E+00	0.0E+00		Lgmn	1.372	0.964	0.624	2.1E-257	3.2E-254
	Dusp14	2.072	0.836	0.675	0.0E+00	0.0E+00		Aif1	2.087	0.853	0.573	2.8E-255	4.3E-252
	Wnt4	2.037	0.882	0.722	0.0E+00	0.0E+00		Atp1a1	1.325	0.957	0.700	3.7E-254	5.6E-251
	Clu	2.031	0.918	0.761	0.0E+00	0.0E+00		Lyz2	0.748	0.994	0.755	9.3E-252	1.4E-248
	Epcam	2.006	0.848	0.601	0.0E+00	0.0E+00		Trf	1.377	0.891	0.499	4.4E-247	6.7E-244
	Anxa1	2.002	0.919	0.772	0.0E+00	0.0E+00		Ms4a6d	1.230	0.895	0.733	2.9E-240	4.4E-237
	Cldn3	1.963	0.803	0.773	0.0E+00	0.0E+00		Csf1r	1.731	0.824	0.437	2.0E-233	3.1E-230
	2310007B03Ril	1.887	0.861	0.663	0.0E+00	0.0E+00		Bcl2a1d	1.057	0.884	0.505	3.6E-223	5.4E-220
	Pdzk1ip1	1.882	0.850	0.786	0.0E+00	0.0E+00		Fcgr1	0.866	0.839	0.480	3.3E-217	5.0E-214
	Prss22	1.850	0.702	0.557	0.0E+00	0.0E+00		Napsa	1.159	0.904	0.579	1.7E-213	2.5E-210
	Aqp5	1.785	0.676	0.741	0.0E+00	0.0E+00		Ly86	1.085	0.807	0.287	7.3E-213	1.1E-209
	Cldn7	1.777	0.732	0.679	0.0E+00	0.0E+00		Ctsc	1.394	0.881	0.644	2.9E-207	4.4E-204
	Jdp2	1.736	0.810	0.711	0.0E+00	0.0E+00		Gm2a	1.234	0.909	0.624	5.8E-207	8.7E-204
	Plpp1	1.699	0.783	0.653	0.0E+00	0.0E+00		Mafb	1.508	0.853	0.588	4.2E-199	6.3E-196
	Avpi1	1.689	0.843	0.712	0.0E+00	0.0E+00		Ccr2	0.905	0.788	0.255	3.8E-195	5.7E-192
	Nccrp1	1.658	0.754	0.730	0.0E+00	0.0E+00		Ifitm3	1.495	0.943	0.695	1.8E-194	2.6E-191
	Errfi1	1.618	0.894	0.564	0.0E+00	0.0E+00		Pgls	0.758	0.921	0.629	5.1E-182	7.6E-179
	Plat	1.601	0.627	0.504	0.0E+00	0.0E+00		Itgb5	0.923	0.849	0.676	1.1E-177	1.6E-174
	Gsta4	1.599	0.796	0.689	0.0E+00	0.0E+00		Rpl3	1.055	0.970	0.708	1.1E-177	1.7E-174
	Tacstd2	1.567	0.736	0.538	0.0E+00	0.0E+00		Gpx1	0.883	0.965	0.833	4.2E-173	6.3E-170
	Calr	1.558	0.945	0.734	0.0E+00	0.0E+00		Clec4a3	1.528	0.770	0.440	5.1E-172	7.6E-169
	Tubb4b	1.556	0.918	0.674	0.0E+00	0.0E+00		Cd72	1.163	0.717	0.163	1.4E-171	2.1E-168
	Wwtr1	1.537	0.890	0.574	0.0E+00	0.0E+00		Cx3cr1	1.589	0.759	0.360	7.3E-171	1.1E-167
	Fxyd3	1.529	0.782	0.582	0.0E+00	0.0E+00		Tgfbi	0.964	0.915	0.601	2.9E-170	4.4E-167
	Csrp1	1.520	0.819	0.671	0.0E+00	0.0E+00		Asah1	0.779	0.879	0.564	1.0E-169	1.5E-166
	Spns3	1.512	0.823	0.552	0.0E+00	0.0E+00		Ptma	0.975	0.965	0.726	1.6E-165	2.4E-162
	Mall	1.506	0.859	0.721	0.0E+00	0.0E+00		Smpdl3a	1.034	0.904	0.622	3.0E-163	4.5E-160
	Gprc5a	1.498	0.799	0.586	0.0E+00	0.0E+00		Ucp2	0.852	0.973	0.726	5.8E-162	8.7E-159
	Herpud1	1.429	0.790	0.560	0.0E+00	0.0E+00		Bcl2a1a	0.700	0.859	0.545	1.3E-159	1.9E-156
	Ddit3	1.405	0.820	0.723	0.0E+00	0.0E+00		Cd300e	1.156	0.727	0.244	4.8E-158	7.1E-155
	Clec2g	1.386	0.818	0.436	0.0E+00	0.0E+00		Ctsz	0.849	0.994	0.790	2.0E-152	3.1E-149
	Dnajb1	1.374	0.893	0.567	0.0E+00	0.0E+00		Laptm5	0.768	0.989	0.732	2.3E-151	3.5E-148
	Cidea	1.304	0.610	0.536	0.0E+00	0.0E+00		Rassf4	0.995	0.789	0.576	1.5E-149	2.3E-146
	Lrrc26	1.302	0.812	0.724	0.0E+00	0.0E+00		Emp3	1.135	0.840	0.456	8.3E-148	1.2E-144
	Cldn23	1.294	0.734	0.615	0.0E+00	0.0E+00		Erp29	1.067	0.922	0.709	9.2E-146	1.4E-142
	Chac1	1.291	0.750	0.706	0.0E+00	0.0E+00		Sdf2l1	0.667	0.902	0.718	1.0E-143	1.5E-140
	Rdh10	1.290	0.787	0.518	0.0E+00	0.0E+00		Cd300c2	0.691	0.932	0.651	5.4E-142	8.1E-139
	Fam57a	1.279	0.733	0.754	0.0E+00	0.0E+00		Clec4a1	1.686	0.720	0.281	1.3E-141	1.9E-138
	Gadd45b	1.263	0.948	0.711	0.0E+00	0.0E+00		Ms4a6b	1.104	0.755	0.271	1.1E-138	1.6E-135
	Cops6	1.253	0.833	0.647	0.0E+00	0.0E+00		Tmem160	0.781	0.834	0.577	2.9E-137	4.4E-134
	Krt8	1.231	0.690	0.700	0.0E+00	0.0E+00		H2-DMa	1.252	0.756	0.394	3.1E-136	4.7E-133
	Gadd45g	1.225	0.659	0.573	0.0E+00	0.0E+00		Abhd12	0.845	0.790	0.432	6.7E-135	1.0E-131
	Fam110a	1.163	0.787	0.499	0.0E+00	0.0E+00		Hexb	1.403	0.863	0.751	6.5E-132	9.7E-129
	Pls3	1.149	0.784	0.594	0.0E+00	0.0E+00		S100a4	1.042	0.790	0.500	1.6E-130	2.3E-127
	Hbegf	1.114	0.731	0.762	0.0E+00	0.0E+00		Flna	0.830	0.835	0.487	2.2E-128	3.3E-125

	Phlda1	1.100	0.759	0.510	0.0E+00	0.0E+00		Unc93b1	0.755	0.848	0.511	1.4E-127	2.0E-124
	Krt80	1.097	0.845	0.529	0.0E+00	0.0E+00		Pid1	0.802	0.765	0.585	1.5E-127	2.2E-124
	Manf	1.096	0.869	0.829	0.0E+00	0.0E+00		Rras	0.921	0.760	0.544	7.2E-126	1.1E-122
	Parm1	1.078	0.778	0.721	0.0E+00	0.0E+00		Itgb2	0.950	0.910	0.585	2.3E-124	3.5E-121
	Hsd17b2	1.076	0.686	0.537	0.0E+00	0.0E+00		Lilra5	1.100	0.724	0.321	2.1E-120	3.2E-117
	Slco2a1	1.075	0.676	0.528	0.0E+00	0.0E+00		Mgst1	0.710	0.874	0.601	1.1E-119	1.6E-116
	2610528A11Rik	1.070	0.701	0.641	0.0E+00	0.0E+00		Selenop	0.924	0.776	0.519	2.1E-115	3.2E-112
	Apol7a	1.050	0.698	0.453	0.0E+00	0.0E+00		mt-Nd1	0.722	0.963	0.666	1.7E-114	2.6E-111
	Mlph	1.045	0.754	0.665	0.0E+00	0.0E+00		Fcgrt	0.886	0.735	0.282	7.0E-114	1.0E-110
	Sqstm1	1.023	0.873	0.581	0.0E+00	0.0E+00		Plekho1	0.926	0.756	0.553	7.7E-112	1.2E-108
	Pmaip1	0.991	0.742	0.669	0.0E+00	0.0E+00		Ndufa4	0.708	0.879	0.666	2.0E-111	3.0E-108
	Oasl1	0.984	0.620	0.575	0.0E+00	0.0E+00		Mef2c	1.025	0.724	0.384	3.3E-106	5.0E-103
	Plac8	0.977	0.735	0.523	0.0E+00	0.0E+00		Irf8	1.231	0.760	0.635	2.2E-105	3.3E-102
	Ifi202b	0.963	0.703	0.648	0.0E+00	0.0E+00		Npc2	0.824	0.958	0.889	2.4E-101	3.7E-98
	Rbp1	0.960	0.608	0.545	0.0E+00	0.0E+00		Plac8	1.352	0.759	0.557	6.2E-100	9.3E-97
	2010109I03Rik	0.930	0.607	0.662	0.0E+00	0.0E+00		H2-DMb1	1.111	0.707	0.428	3.2E-94	4.9E-91
	Tspan8	0.903	0.766	0.646	0.0E+00	0.0E+00		Tifab	0.751	0.686	0.354	2.7E-81	4.1E-78
	Yod1	0.898	0.649	0.569	0.0E+00	0.0E+00		Pltp	0.669	0.703	0.365	9.6E-81	1.4E-77
	Cald1	0.888	0.677	0.690	0.0E+00	0.0E+00		Ccdc88a	1.007	0.688	0.547	2.3E-70	3.5E-67
	Plk2	0.881	0.723	0.493	0.0E+00	0.0E+00		Ear2	1.003	0.647	0.320	8.7E-66	1.3E-62
	Ephb3	0.877	0.717	0.631	0.0E+00	0.0E+00		Ms4a4c	0.756	0.630	0.135	1.7E-64	2.5E-61
	Oit1	0.851	0.751	0.566	0.0E+00	0.0E+00		Ace	1.683	0.644	0.536	6.6E-64	9.9E-61
	Hsp90aa1	0.846	0.911	0.832	0.0E+00	0.0E+00		Evl	0.693	0.688	0.340	1.6E-61	2.4E-58
	Klk8	0.932	0.547	0.488	6.8E-289	1.0E-285		Ifi27l2a	0.784	0.697	0.528	8.9E-55	1.3E-51
	Hsp90b1	1.266	0.827	0.781	2.1E-272	3.1E-269		Gm15987	0.810	0.635	0.261	1.1E-54	1.6E-51
	Tsc22d1	0.850	0.640	0.773	8.6E-178	1.3E-174		Klf4	0.724	0.648	0.422	4.9E-44	7.3E-41
	Clic5	1.114	0.581	0.733	7.7E-159	1.2E-155		Slc12a2	1.262	0.706	0.578	4.8E-43	7.2E-40
	Ifit1bl1	1.446	0.487	0.470	6.4E-149	9.6E-146		Adgre4	0.930	0.597	0.375	2.9E-42	4.4E-39
	Cxcl5	1.588	0.446	0.399	6.7E-125	1.0E-121		Bst2	0.727	0.651	0.506	1.1E-30	1.7E-27
	Pigr	0.995	0.441	0.469	6.3E-68	9.5E-65		Tmem176b	1.272	0.622	0.568	1.4E-22	2.1E-19
	Cxcl3	1.035	0.364	0.517	5.7E-03	1.0E+00		Krt80	0.745	0.634	0.587	1.1E-20	1.6E-17
Neu-1	Cst3	1.532	0.929	0.800	0.0E+00	0.0E+00	**B cells**	Igkc	4.317	0.964	0.279	0.0E+00	0.0E+00
	Gngt2	1.374	0.812	0.614	0.0E+00	0.0E+00		Ighm	3.141	0.908	0.317	0.0E+00	0.0E+00
	Id2	1.172	0.925	0.753	0.0E+00	0.0E+00		Cd74	3.059	0.992	0.554	0.0E+00	0.0E+00
	Ptgs1	1.172	0.772	0.678	0.0E+00	0.0E+00		H2-Ab1	2.828	0.975	0.628	0.0E+00	0.0E+00
	Laptm5	0.838	0.829	0.722	0.0E+00	0.0E+00		H2-Aa	2.789	0.983	0.554	0.0E+00	0.0E+00
	Gm19951	0.675	0.840	0.656	0.0E+00	0.0E+00		Cd79a	2.550	0.908	0.408	0.0E+00	0.0E+00
	Ccl4	0.552	0.895	0.685	0.0E+00	0.0E+00		Cd79b	2.207	0.854	0.309	0.0E+00	0.0E+00
	Hist1h1e	0.491	0.794	0.590	0.0E+00	0.0E+00		Ebf1	2.190	0.862	0.157	0.0E+00	0.0E+00
	Asprv1	0.446	0.778	0.552	0.0E+00	0.0E+00		Iglc2	2.133	0.870	0.147	0.0E+00	0.0E+00
	Egr2	0.310	0.274	0.401	3.3E-290	5.0E-287		Cd72	1.409	0.846	0.159	0.0E+00	0.0E+00
	B930036N10Rik	0.499	0.642	0.468	1.2E-283	1.8E-280		Serpina3g	0.465	0.972	0.560	0.0E+00	0.0E+00
	Id1	1.043	0.832	0.665	4.7E-266	7.1E-263		Gatm	0.355	0.992	0.516	0.0E+00	0.0E+00
	Gpx1	0.848	0.869	0.830	3.8E-265	5.7E-262		Ighd	2.304	0.799	0.270	1.4E-299	2.1E-296
	Ms4a6d	0.565	0.805	0.725	7.4E-254	1.1E-250		Gm15987	0.802	0.838	0.255	1.2E-273	1.9E-270
	Csf1r	0.366	0.280	0.483	9.3E-226	1.4E-222		Jchain	1.341	0.826	0.370	9.8E-271	1.5E-267
	Gpc3	0.286	0.688	0.670	3.7E-198	5.5E-195		Ms4a1	1.914	0.819	0.197	6.8E-270	1.0E-266
	Cd300c2	1.210	0.716	0.649	5.2E-190	7.8E-187		Ly6d	0.446	0.929	0.779	5.9E-245	8.9E-242
	Hist1h1d	0.253	0.697	0.533	8.4E-188	1.3E-184		Rpl3	1.155	0.991	0.707	7.0E-233	1.1E-229
	Ptgs2	0.526	0.234	0.306	4.4E-180	6.6E-177		Mef2c	1.562	0.830	0.381	8.7E-231	1.3E-227
	Pmaip1	0.518	0.787	0.662	1.1E-178	1.6E-175		Bank1	1.757	0.792	0.348	2.6E-210	3.9E-207
	Ccl3	0.592	0.738	0.624	1.2E-148	1.8E-145		Ptma	0.989	0.991	0.725	2.2E-205	3.3E-202
	Osgin1	0.724	0.685	0.570	7.6E-146	1.1E-142		Igha	1.645	0.780	0.378	1.0E-200	1.5E-197
	Olr1	0.348	0.328	0.404	8.3E-139	1.2E-135		Ighg1	1.025	0.772	0.364	8.7E-190	1.3E-186
	Pi16	0.312	0.619	0.443	4.3E-134	6.5E-131		H2-DMa	0.962	0.810	0.392	7.6E-178	1.1E-174
	Hexb	0.810	0.794	0.746	4.2E-133	6.3E-130		Fam96a	0.433	0.939	0.556	5.6E-177	8.5E-174
	Fcgr4	0.354	0.750	0.685	1.7E-126	2.6E-123		Gpr65	0.440	0.838	0.448	3.8E-174	5.7E-171
	Bcl2a1d	0.547	0.380	0.543	1.6E-123	2.4E-120		Iglc3	1.588	0.712	0.157	2.9E-168	4.3E-165
	Cd63	0.327	0.866	0.768	2.9E-120	4.4E-117		Napsa	1.338	0.843	0.582	3.3E-163	5.0E-160
	Ier3	0.771	0.802	0.786	5.3E-113	8.0E-110		mt-Nd1	0.665	0.967	0.666	1.3E-152	1.9E-149
	Atp1a1	0.853	0.779	0.694	1.1E-110	1.7E-107		Ets1	1.116	0.792	0.447	1.3E-150	1.9E-147
	Hk2	0.263	0.470	0.609	5.4E-104	8.0E-101		Mzb1	1.617	0.728	0.330	2.9E-146	4.3E-143
	P2ry6	0.401	0.710	0.682	1.5E-100	2.3E-97		Rps2	0.667	0.989	0.892	8.8E-135	1.3E-131
	Lrg1	0.265	0.765	0.686	1.4E-95	2.1E-92		Fcmr	1.153	0.750	0.392	8.3E-132	1.2E-128
	Gm12840	1.099	0.321	0.411	2.0E-95	3.0E-92		Gm31243	1.017	0.709	0.181	9.7E-121	1.5E-117
	H1f0	0.599	0.700	0.568	2.2E-87	3.3E-84		H2-DMb2	1.138	0.718	0.272	2.2E-119	3.3E-116
	Naaa	0.359	0.655	0.568	4.8E-75	7.2E-72		Ranbp1	0.695	0.826	0.642	4.2E-105	6.4E-102
	Ltc4s	0.796	0.644	0.599	1.2E-72	1.9E-69		Gm8369	0.449	0.297	0.105	1.4E-101	2.1E-98
	Reep5	0.646	0.749	0.711	5.2E-55	7.9E-52		Gimap6	1.256	0.710	0.321	1.5E-98	2.3E-95
	Egr1	0.842	0.617	0.544	1.1E-51	1.6E-48		4930523C07R	1.050	0.716	0.510	6.0E-92	9.0E-89
	Asah1	0.261	0.666	0.555	1.3E-49	2.0E-46		Ptprcap	0.932	0.716	0.524	7.3E-82	1.1E-78
	Gm2a	0.855	0.637	0.632	1.0E-45	1.5E-42		Cd55	0.849	0.734	0.433	3.2E-81	4.8E-78
	Hist1h4i	1.255	0.646	0.671	1.8E-45	2.8E-42		Fcer2a	1.434	0.669	0.501	4.6E-75	6.9E-72
	Chil1	0.513	0.593	0.475	2.1E-43	3.2E-40		Erp29	0.518	0.910	0.710	1.4E-73	2.1E-70
	Tgm2	0.664	0.463	0.641	5.8E-43	8.6E-40		Pax5	0.985	0.641	0.212	3.4E-73	5.1E-70

	Dpep2	0.374	0.652	0.687	7.8E-43	1.2E-39
	Ctsa	0.381	0.744	0.697	2.0E-42	2.9E-39
	Fgd4	0.251	0.688	0.624	1.5E-41	2.3E-38
	Fam20c	0.442	0.792	0.763	5.8E-41	8.7E-38
	Pou2f2	0.312	0.387	0.444	1.9E-34	2.9E-31
	Cks2	1.189	0.534	0.460	3.2E-33	4.8E-30
	Rhoc	0.380	0.529	0.605	3.6E-33	5.3E-30
	Fyb	0.514	0.751	0.686	7.6E-32	1.1E-28
	Fcgr2b	0.347	0.713	0.648	2.8E-31	4.1E-28
	C3	0.875	0.585	0.551	5.4E-30	8.1E-27
	Slc7a11	0.272	0.428	0.478	6.5E-28	9.7E-25
	Hist1h1c	0.763	0.664	0.606	5.7E-26	8.5E-23
	Tcirg1	0.280	0.550	0.636	9.7E-26	1.5E-22
	Abca1	0.438	0.768	0.731	1.2E-25	1.7E-22
	Rgs1	1.284	0.650	0.628	1.6E-25	2.4E-22
	Csf2rb	0.693	0.676	0.689	3.6E-25	5.5E-22
	Bcl2a1b	0.872	0.640	0.631	2.0E-23	2.9E-20
	Ccng1	0.266	0.520	0.595	7.3E-23	1.1E-19
	Agap1	0.867	0.586	0.610	2.6E-22	3.9E-19
	Erp29	0.301	0.600	0.739	1.2E-21	1.7E-18
	Slc6a6	0.338	0.463	0.522	2.5E-21	3.7E-18
	Tnf	0.725	0.327	0.308	9.4E-19	1.4E-15
	Hist1h2ap	0.263	0.508	0.479	6.2E-18	9.3E-15
	Gm20186	0.564	0.404	0.440	6.6E-18	9.9E-15
	Cfp	0.354	0.543	0.434	1.4E-17	2.2E-14
	Unc93b1	0.643	0.570	0.512	3.2E-16	4.8E-13
	Ptma	0.282	0.760	0.728	3.5E-15	5.2E-12
	Itgax	0.746	0.468	0.563	2.5E-14	3.8E-11
	Aprt	0.365	0.639	0.761	2.1E-12	3.1E-09
	Itgb2	0.303	0.503	0.614	2.2E-12	3.3E-09
	Ucp2	0.280	0.743	0.732	4.5E-11	6.8E-08
	Bcl2a1a	0.956	0.592	0.547	7.5E-10	1.1E-06
	Arhgap25	0.475	0.546	0.497	4.7E-08	7.1E-05
	G0s2	0.960	0.524	0.494	1.9E-06	2.8E-03
	Gm26870	0.339	0.577	0.569	5.6E-05	8.3E-02
	Cdkn1a	0.436	0.825	0.760	5.5E-04	8.2E-01
	Tgfbi	0.656	0.586	0.616	5.7E-04	8.5E-01
	Mpeg1	0.405	0.595	0.629	6.4E-04	9.6E-01
	Csf2ra	0.674	0.543	0.575	1.5E-03	1.0E+00
	Tnfrsf23	0.465	0.654	0.712	5.8E-03	1.0E+00
Neu-2	Gm5483	2.762	0.938	0.564	0.0E+00	0.0E+00
	BC100530	2.671	0.815	0.520	0.0E+00	0.0E+00
	Wfdc17	2.485	0.993	0.744	0.0E+00	0.0E+00
	Cxcl2	2.340	0.951	0.469	0.0E+00	0.0E+00
	Ifitm1	2.087	0.963	0.701	0.0E+00	0.0E+00
	Retnlg	2.057	0.960	0.576	0.0E+00	0.0E+00
	Wfdc21	1.768	0.945	0.605	0.0E+00	0.0E+00
	Lrg1	1.760	0.929	0.661	0.0E+00	0.0E+00
	G0s2	1.756	0.819	0.446	0.0E+00	0.0E+00
	Egr1	1.705	0.912	0.497	0.0E+00	0.0E+00
	Lcn2	1.667	0.911	0.561	0.0E+00	0.0E+00
	Ier3	1.643	0.972	0.758	0.0E+00	0.0E+00
	Slpi	1.397	0.904	0.602	0.0E+00	0.0E+00
	Adam8	1.286	0.729	0.572	0.0E+00	0.0E+00
	Ccl4	1.276	0.981	0.676	0.0E+00	0.0E+00
	F630028O10Ri	1.234	0.798	0.503	0.0E+00	0.0E+00
	Slfn4	1.160	0.942	0.505	0.0E+00	0.0E+00
	Id1	0.989	0.915	0.655	0.0E+00	0.0E+00
	Csf2rb	0.976	0.921	0.648	0.0E+00	0.0E+00
	Steap4	0.965	0.732	0.447	0.0E+00	0.0E+00
	Hcar2	0.955	0.882	0.648	0.0E+00	0.0E+00
	Prok2	0.868	0.790	0.548	0.0E+00	0.0E+00
	Olfm4	0.701	0.793	0.426	0.0E+00	0.0E+00
	Dgat2	0.563	0.795	0.603	0.0E+00	0.0E+00
	Tceal9	0.557	0.888	0.641	0.0E+00	0.0E+00
	Cxcl3	0.533	0.840	0.429	0.0E+00	0.0E+00
	Cd177	0.461	0.740	0.458	0.0E+00	0.0E+00
	Tnfrsf23	0.440	0.910	0.668	0.0E+00	0.0E+00
	Hk2	0.430	0.884	0.536	0.0E+00	0.0E+00
	Ccl6	0.398	0.910	0.592	0.0E+00	0.0E+00
	Cdkn1a	0.298	0.945	0.742	0.0E+00	0.0E+00
	Rgcc	0.260	0.926	0.710	0.0E+00	0.0E+00
	Slc7a11	0.868	0.715	0.429	1.1E-307	1.6E-304
	Mmp8	0.729	0.731	0.597	8.0E-292	1.2E-288
	Stfa2l1	2.238	0.682	0.448	1.4E-272	2.1E-269
	Ndufa4	0.509	0.843	0.667	4.6E-69	6.9E-66
	Sdc4	0.893	0.745	0.674	2.2E-67	3.3E-64
	Tnfrsf13c	0.888	0.622	0.177	2.7E-67	4.1E-64
	Scd1	1.063	0.661	0.348	8.6E-65	1.3E-61
	Hmgn1	0.833	0.723	0.652	7.2E-61	1.1E-57
	Hspe1	0.691	0.777	0.674	5.8E-60	8.7E-57
	Hes1	0.392	0.338	0.532	7.1E-59	1.1E-55
	Pxdc1	0.899	0.660	0.339	2.1E-58	3.2E-55
	Cd180	0.448	0.352	0.326	1.2E-54	1.8E-51
	Pgls	0.647	0.753	0.634	2.2E-54	3.3E-51
	Nap1l1	0.555	0.726	0.561	1.5E-44	2.2E-41
	Blk	0.482	0.380	0.328	1.6E-43	2.3E-40
	Bcar3	0.432	0.387	0.408	3.1E-43	4.7E-40
	Gimap3	0.924	0.632	0.218	1.3E-42	2.0E-39
	AC149090.1	1.234	0.659	0.455	1.3E-41	1.9E-38
	Irf8	0.826	0.671	0.638	8.6E-38	1.3E-34
	Pou2f2	0.590	0.656	0.428	5.8E-36	8.7E-33
	Ms4a4c	0.498	0.386	0.143	8.2E-36	1.2E-32
	Tubb5	0.433	0.727	0.599	1.1E-33	1.7E-30
	Ly86	0.735	0.619	0.293	8.3E-27	1.2E-23
	Aldh2	0.584	0.639	0.517	2.6E-26	3.9E-23
	S1pr1	0.415	0.391	0.514	1.3E-24	1.9E-21
	Id3	0.855	0.605	0.569	1.8E-24	2.7E-21
	Pou2af1	1.186	0.585	0.245	5.4E-24	8.1E-21
	Lmo2	0.870	0.616	0.400	1.0E-23	1.5E-20
	Gimap1	0.903	0.615	0.455	3.2E-23	4.9E-20
	C1qbp	0.416	0.684	0.663	3.0E-22	4.5E-19
	Slc25a4	0.458	0.662	0.537	2.2E-21	3.3E-18
	Gimap7	0.681	0.581	0.231	4.9E-21	7.3E-18
	Myo1e	0.370	0.454	0.610	3.7E-20	5.5E-17
	Siglecg	0.415	0.590	0.505	4.4E-17	6.6E-14
	Eprs	0.470	0.654	0.584	2.2E-16	3.3E-13
	Nucks1	0.526	0.636	0.534	2.7E-15	4.0E-12
	Plekho1	0.670	0.621	0.557	1.2E-14	1.9E-11
	Zbtb20	0.422	0.454	0.546	7.7E-14	1.2E-10
	Evl	0.561	0.600	0.343	3.7E-13	5.6E-10
	Snx5	0.608	0.621	0.551	2.3E-12	3.5E-09
	Ciita	0.638	0.441	0.281	1.7E-11	2.6E-08
	Blnk	0.663	0.596	0.738	2.1E-10	3.2E-07
	Sptbn1	0.654	0.623	0.580	6.2E-10	9.3E-07
	Iglc1	1.620	0.546	0.204	9.9E-09	1.5E-05
	Ms4a6c	0.618	0.593	0.418	1.4E-08	2.1E-05
	Cd2ap	0.534	0.624	0.597	1.7E-08	2.6E-05
	Cd69	0.605	0.558	0.334	5.9E-08	8.8E-05
	Ms4a6b	0.387	0.469	0.280	2.3E-07	3.4E-04
	Bin1	0.731	0.578	0.566	2.8E-07	4.2E-04
	Kcnq1ot1	0.583	0.624	0.657	3.6E-07	5.4E-04
	Odc1	0.433	0.478	0.572	3.6E-07	5.4E-04
	Vpreb3	1.232	0.539	0.135	4.7E-07	7.1E-04
	Nr4a1	0.505	0.424	0.317	1.1E-06	1.7E-03
	Rftn1	0.435	0.495	0.627	2.7E-06	4.1E-03
	Pdia4	0.591	0.566	0.537	7.0E-06	1.1E-02
	Gpr171	0.531	0.481	0.578	3.9E-05	5.9E-02
	Ikzf3	0.915	0.544	0.267	4.1E-05	6.2E-02
	Gpr183	0.771	0.535	0.267	4.2E-04	6.2E-01
	Cd38	0.484	0.588	0.584	8.6E-03	1.0E+00
Lung Ep.	Il33	1.978	0.892	0.537	0.0E+00	0.0E+00
	Areg	1.182	0.853	0.425	1.7E-291	2.6E-288
	Fxyd3	2.925	0.930	0.612	1.3E-275	2.0E-272
	Wfdc2	4.063	0.911	0.760	1.7E-275	2.5E-272
	Col1a1	1.424	0.721	0.220	4.9E-249	7.3E-246
	Dapl1	1.474	0.823	0.391	1.1E-243	1.6E-240
	Col1a2	1.973	0.756	0.381	8.7E-239	1.3E-235
	Btbd3	1.083	0.834	0.570	1.3E-220	1.9E-217
	Ly6d	1.756	0.948	0.779	8.8E-220	1.3E-216
	Hspb1	1.934	0.823	0.582	6.5E-217	9.7E-214
	Wfdc3	1.449	0.821	0.682	5.9E-205	8.8E-202
	Ckmt1	1.370	0.883	0.732	1.1E-200	1.7E-197
	Gpx2	1.928	0.819	0.571	1.7E-198	2.6E-195
	Cdh1	1.240	0.859	0.604	1.2E-197	1.8E-194
	Tmem176a	2.040	0.873	0.582	7.6E-197	1.1E-193
	Ehf	2.134	0.855	0.799	5.1E-196	7.6E-193
	Gsta4	2.610	0.871	0.705	1.8E-191	2.7E-188
	Them5	1.260	0.732	0.268	1.7E-187	2.5E-184
	Cldn7	1.072	0.896	0.684	1.1E-182	1.6E-179

	Osgin1	0.516	0.765	0.560	5.6E-269	8.5E-266		Clu	2.509	0.912	0.787	1.7E-182	2.5E-179
	Stfa2	1.396	0.680	0.497	3.6E-261	5.4E-258		Avpi1	1.828	0.900	0.732	2.4E-182	3.6E-179
	Il1f9	0.937	0.718	0.534	1.0E-248	1.6E-245		Cp	1.550	0.766	0.560	1.4E-168	2.1E-165
	Gadd45a	0.936	0.731	0.606	1.1E-241	1.7E-238		Cald1	1.304	0.837	0.684	1.2E-164	1.8E-161
	Ifitm3	0.397	0.844	0.679	2.8E-228	4.3E-225		Mgp	2.757	0.817	0.644	3.8E-162	5.7E-159
	Hip1	0.280	0.812	0.586	5.1E-221	7.7E-218		Cbr2	3.030	0.806	0.745	6.7E-160	1.0E-156
	Ifitm6	0.479	0.683	0.435	1.5E-216	2.2E-213		Ybx3	1.340	0.857	0.598	6.7E-160	1.0E-156
	Chil1	0.781	0.691	0.462	2.0E-216	2.9E-213		Far1	1.422	0.882	0.509	6.9E-160	1.0E-156
	Asprv1	1.206	0.707	0.570	1.3E-199	1.9E-196		Plac8	1.530	0.919	0.554	8.7E-160	1.3E-156
	Tgm2	0.428	0.758	0.587	5.2E-159	7.8E-156		Serping1	1.481	0.693	0.306	5.8E-159	8.7E-156
	Acod1	0.849	0.624	0.389	1.6E-127	2.5E-124		Akr1b3	1.620	0.866	0.517	1.5E-157	2.2E-154
	Fyb	0.331	0.786	0.682	1.7E-118	2.6E-115		Cd81	1.439	0.922	0.607	1.0E-155	1.5E-152
	Saa3	0.560	0.748	0.606	4.7E-83	7.1E-80		Scgb1a1	3.980	0.915	0.811	7.6E-155	1.1E-151
	Ly6g	0.520	0.596	0.425	4.1E-82	6.1E-79		Id3	1.470	0.769	0.565	1.6E-149	2.5E-146
	Tgfbi	0.391	0.696	0.596	1.9E-80	2.8E-77		Perp	1.659	0.834	0.733	1.2E-147	1.8E-144
	Gm5416	0.363	0.605	0.486	5.7E-76	8.5E-73		Ppp1r14b	1.481	0.892	0.660	6.9E-146	1.0E-142
	Pi16	0.460	0.605	0.450	1.1E-70	1.6E-67		Tpm2	1.173	0.815	0.658	4.9E-138	7.4E-135
	Fcgr4	0.341	0.715	0.693	1.4E-60	2.0E-57		Ceacam1	1.300	0.918	0.689	2.4E-135	3.5E-132
	Slc6a6	0.335	0.651	0.489	4.4E-51	6.6E-48		Igfbp4	1.213	0.714	0.516	3.6E-125	5.4E-122
	Csf2ra	0.339	0.671	0.553	1.6E-47	2.4E-44		Rpl3	1.482	0.892	0.712	1.4E-118	2.1E-115
	Fgd4	0.308	0.677	0.628	5.9E-39	8.9E-36		Ptprf	1.412	0.746	0.622	2.3E-117	3.4E-114
	Stfa3	0.456	0.528	0.544	1.1E-08	1.7E-05		Rps2	1.263	0.934	0.894	1.5E-115	2.2E-112
	Hacd4	0.323	0.496	0.524	8.5E-08	1.3E-04		Nenf	1.188	0.790	0.520	6.5E-109	9.7E-106
	Ptgs2	0.592	0.407	0.275	1.3E-07	2.0E-04		Arg1	1.174	0.919	0.760	1.7E-105	2.6E-102
	Fosb	0.422	0.476	0.366	3.8E-03	1.0E+00		Nedd4	1.526	0.696	0.323	1.8E-105	2.8E-102
Neu-3	Ccl3	2.965	0.920	0.610	0.0E+00	0.0E+00		Dmkn	1.828	0.776	0.719	1.0E-104	1.6E-101
	Hcar2	2.705	0.884	0.657	0.0E+00	0.0E+00		Fabp5	2.134	0.923	0.803	7.8E-103	1.2E-99
	Ccl4	2.320	0.868	0.702	0.0E+00	0.0E+00		Gm26870	1.224	0.813	0.564	1.2E-101	1.8E-98
	Nceh1	2.161	0.856	0.686	0.0E+00	0.0E+00		Eln	1.022	0.671	0.350	3.1E-100	4.6E-97
	Gadd45b	2.109	0.877	0.741	0.0E+00	0.0E+00		Scgb3a1	4.567	0.740	0.635	1.2E-99	1.8E-96
	Ifrd1	1.995	0.819	0.702	0.0E+00	0.0E+00		Pam	1.544	0.788	0.651	1.9E-97	2.9E-94
	Hilpda	1.887	0.836	0.728	0.0E+00	0.0E+00		Aqp5	1.174	0.777	0.728	4.3E-96	6.5E-93
	Atp6v1c1	1.859	0.857	0.741	0.0E+00	0.0E+00		Phlda1	1.105	0.823	0.551	4.7E-95	7.1E-92
	Zeb2	1.831	0.829	0.607	0.0E+00	0.0E+00		Prdx2	1.395	0.805	0.642	2.1E-89	3.1E-86
	Cd63	1.769	0.936	0.766	0.0E+00	0.0E+00		Epcam	1.512	0.786	0.644	4.0E-89	6.0E-86
	Ftl1	1.745	1.000	0.953	0.0E+00	0.0E+00		Dcxr	1.400	0.768	0.619	4.5E-87	6.8E-84
	Id2	1.629	0.874	0.771	0.0E+00	0.0E+00		Serpinb6b	1.063	0.769	0.688	5.7E-86	8.6E-83
	F10	1.608	0.863	0.694	0.0E+00	0.0E+00		Rbp1	1.619	0.722	0.552	4.9E-85	7.3E-82
	Ctsz	1.414	0.936	0.780	0.0E+00	0.0E+00		Muc5b	2.403	0.675	0.506	7.2E-84	1.1E-80
	Ctsb	1.241	0.977	0.941	0.0E+00	0.0E+00		Scd1	1.002	0.226	0.360	1.4E-83	2.2E-80
	Gas2l3	1.116	0.818	0.634	0.0E+00	0.0E+00		Tsc22d1	1.408	0.780	0.747	1.2E-81	1.9E-78
	Dhfr	0.942	0.789	0.739	0.0E+00	0.0E+00		Socs2	1.111	0.732	0.667	2.5E-80	3.8E-77
	Lhfpl2	0.915	0.784	0.664	0.0E+00	0.0E+00		Selenbp1	2.144	0.707	0.645	4.2E-80	6.3E-77
	Ctsd	0.494	0.987	0.963	0.0E+00	0.0E+00		Krt8	1.959	0.720	0.698	5.2E-77	7.9E-74
	Fcgr2b	0.726	0.838	0.637	1.2E-307	1.8E-304		Atp5g1	1.265	0.834	0.645	8.9E-76	1.3E-72
	Chka	0.537	0.738	0.519	3.0E-302	4.5E-299		Prdx1	1.233	0.822	0.667	1.8E-74	2.6E-71
	H2-Eb1	1.000	0.683	0.519	1.0E-285	1.5E-282		Sftpb	1.227	0.664	0.439	2.9E-74	4.4E-71
	Cd274	1.549	0.725	0.579	2.4E-265	3.6E-262		Retnla	1.246	0.738	0.750	1.6E-71	2.3E-68
	Plcxd2	0.637	0.728	0.653	3.2E-265	4.8E-262		Nfib	1.180	0.680	0.619	2.7E-70	4.1E-67
	Hexa	0.947	0.839	0.688	1.1E-248	1.7E-245		Aldh1a1	1.071	0.648	0.384	9.0E-69	1.3E-65
	Dock10	0.893	0.783	0.666	2.7E-239	4.1E-236		Nupr1	1.463	0.795	0.711	1.2E-68	1.8E-65
	Pdxk	0.597	0.726	0.574	7.5E-236	1.1E-232		Ifitm3	1.335	0.809	0.700	6.7E-68	1.0E-64
	Cxcl2	1.230	0.759	0.512	6.9E-233	1.0E-229		Sdc4	1.174	0.760	0.674	1.7E-65	2.5E-62
	Psap	0.760	0.852	0.749	1.3E-230	1.9E-227		Cldn3	1.119	0.776	0.778	5.3E-64	8.0E-61
	Gns	1.339	0.782	0.688	1.3E-230	2.0E-227		Scd2	1.073	0.705	0.541	6.5E-63	9.7E-60
	Lamp1	1.194	0.885	0.861	2.6E-229	3.9E-226		Timp3	1.525	0.657	0.569	1.1E-59	1.6E-56
	Atf3	1.754	0.679	0.548	3.1E-224	4.7E-221		Scgb3a2	2.769	0.668	0.618	4.3E-58	6.5E-55
	Npc1	1.211	0.749	0.677	5.2E-220	7.8E-217		Dbi	1.376	0.776	0.646	7.1E-52	1.1E-48
	Ccnf	0.536	0.662	0.612	4.8E-210	7.3E-207		Tmem176b	1.986	0.660	0.567	2.6E-51	3.9E-48
	Plekhm2	1.096	0.785	0.726	1.7E-206	2.5E-203		Sdc1	1.649	0.700	0.709	1.3E-43	2.0E-40
	Rgs1	1.675	0.774	0.615	1.1E-205	1.6E-202		Cyp2f2	2.315	0.663	0.704	2.5E-42	3.7E-39
	Ier3	1.085	0.810	0.786	1.8E-195	2.7E-192		Bgn	1.569	0.550	0.243	1.1E-39	1.7E-36
	9130230L23Rik	0.335	0.648	0.524	1.2E-192	1.8E-189		Trf	1.356	0.684	0.507	1.6E-37	2.5E-34
	P2rx7	0.626	0.760	0.609	9.9E-177	1.5E-173		Wfdc18	1.473	0.361	0.563	6.2E-34	9.4E-31
	Fam20c	0.499	0.847	0.758	1.7E-170	2.6E-167		Sparc	2.443	0.542	0.358	1.0E-32	1.6E-29
	Gstm1	0.562	0.697	0.550	1.0E-164	1.6E-161		Foxq1	1.159	0.583	0.537	2.1E-25	3.2E-22
	Hmox1	1.389	0.790	0.754	7.4E-133	1.1E-129		Tff2	1.506	0.544	0.381	1.1E-24	1.7E-21
	Aprt	0.932	0.820	0.731	3.6E-132	5.4E-129		Ndufc2	1.065	0.660	0.625	1.1E-23	1.7E-20
	Tnfrsf12a	0.301	0.721	0.595	1.8E-125	2.7E-122		Chchd10	1.241	0.644	0.644	2.8E-22	4.3E-19
	Tpp1	0.909	0.716	0.608	4.3E-113	6.5E-110		Igfbp5	1.952	0.347	0.441	9.8E-22	1.5E-18
	Inhba	0.910	0.622	0.550	4.4E-112	6.5E-109		Ccnd1	1.370	0.572	0.514	2.1E-19	3.2E-16
	Tst	0.398	0.688	0.590	1.2E-95	1.9E-92		Tagln2	1.084	0.659	0.593	5.6E-18	8.5E-15
	Tcirg1	1.119	0.670	0.616	9.4E-90	1.4E-86		Hmgn1	1.450	0.616	0.655	9.1E-17	1.4E-13
	Canx	0.712	0.769	0.666	1.2E-87	1.8E-84		Snhg18	1.056	0.551	0.593	1.2E-10	1.7E-07
	Mpeg1	0.696	0.701	0.614	6.5E-80	9.7E-77		C3	1.081	0.651	0.554	3.2E-06	4.8E-03

	Tmem86a	0.586	0.724	0.687	1.8E-78	2.7E-75
	Osm	0.502	0.286	0.341	5.9E-76	8.8E-73
	C3	0.873	0.632	0.548	3.4E-72	5.1E-69
	Slc7a11	1.622	0.565	0.458	4.8E-70	7.2E-67
	Acod1	1.455	0.548	0.408	1.2E-65	1.8E-62
	Ftl1-ps1	0.517	0.338	0.440	5.7E-65	8.5E-62
	Naglu	0.833	0.616	0.547	7.7E-61	1.2E-57
	Gm5416	0.294	0.605	0.491	3.2E-55	4.8E-52
	Prok2	0.362	0.643	0.575	3.5E-50	5.2E-47
	Cd300c2	0.878	0.675	0.658	2.2E-49	3.3E-46
	Hk2	0.718	0.466	0.600	6.9E-44	1.0E-40
	Slc43a3	0.347	0.577	0.585	8.1E-44	1.2E-40
	Creg1	1.161	0.702	0.668	6.8E-39	1.0E-35
	Cldn1	0.605	0.582	0.623	1.3E-37	2.0E-34
	Hspa1b	0.760	0.659	0.609	2.5E-37	3.8E-34
	G0s2	0.733	0.597	0.488	6.5E-37	9.7E-34
	Tgm2	0.386	0.453	0.630	1.1E-35	1.7E-32
	Ctsa	0.424	0.748	0.700	1.5E-35	2.2E-32
	Cxcr1	0.882	0.643	0.718	9.1E-35	1.4E-31
	Gadd45g	0.961	0.634	0.584	2.1E-31	3.2E-28
	Cd68	0.694	0.714	0.715	6.3E-31	9.4E-28
	Tnfrsf23	0.997	0.661	0.707	8.2E-31	1.2E-27
	Hal	0.570	0.514	0.710	1.2E-30	1.8E-27
	Syngr1	0.408	0.721	0.777	1.4E-28	2.0E-25
	Ptgs2	0.446	0.299	0.293	4.0E-27	6.0E-24
	Slc37a2	0.659	0.609	0.589	5.6E-27	8.4E-24
	Dpp7	0.410	0.624	0.628	5.7E-25	8.6E-22
	Laptm5	0.357	0.748	0.739	3.4E-23	5.1E-20
	Hpgds	0.365	0.680	0.634	4.8E-21	7.2E-18
	Rps6ka2	0.407	0.521	0.487	7.5E-20	1.1E-16
	Slc6a6	0.352	0.448	0.520	6.6E-18	9.9E-15
	Syne1	0.775	0.511	0.619	2.1E-17	3.1E-14
	Vegfa	0.957	0.495	0.433	7.9E-17	1.2E-13
	Asprv1	0.304	0.639	0.584	1.2E-14	1.8E-11
	Sqstm1	0.695	0.608	0.639	3.5E-14	5.2E-11
	Tnf	0.606	0.311	0.311	1.1E-12	1.6E-09
	Gm26870	0.659	0.567	0.570	1.1E-11	1.7E-08
	Hspa9	0.318	0.651	0.648	1.1E-09	1.6E-06
	Osgin1	0.594	0.500	0.600	5.8E-08	8.7E-05
	Csf2rb	0.453	0.681	0.687	7.0E-07	1.1E-03
	Egr1	0.431	0.574	0.554	8.2E-07	1.2E-03
	Dhrs3	0.461	0.674	0.676	1.1E-06	1.7E-03
	Thbs1	1.309	0.451	0.550	7.4E-06	1.1E-02
	Cdkn1a	0.339	0.776	0.770	4.9E-05	7.3E-02
	Gadd45a	0.424	0.639	0.622	1.8E-04	2.6E-01
	Hist1h4i	0.531	0.648	0.669	3.2E-04	4.8E-01
	Slpi	0.477	0.653	0.644	3.7E-04	5.5E-01
	Ddit3	0.444	0.598	0.758	3.7E-04	5.6E-01
	Il1f9	0.929	0.529	0.564	5.8E-04	8.7E-01
	Sirpa	0.299	0.560	0.634	5.2E-03	1.0E+00
T cells	Cd3g	2.602	0.918	0.436	0.0E+00	0.0E+00
	Trbc2	2.530	0.904	0.229	0.0E+00	0.0E+00
	Il7r	2.308	0.820	0.669	0.0E+00	0.0E+00
	Bcl2	2.093	0.817	0.414	0.0E+00	0.0E+00
	Rpl3	1.972	0.988	0.699	0.0E+00	0.0E+00
	Cd3e	1.953	0.856	0.286	0.0E+00	0.0E+00
	Cd3d	1.904	0.890	0.375	0.0E+00	0.0E+00
	Ptprcap	1.902	0.828	0.511	0.0E+00	0.0E+00
	Gimap1	1.875	0.851	0.436	0.0E+00	0.0E+00
	Cxcr6	1.867	0.946	0.284	0.0E+00	0.0E+00
	Ctla2a	1.782	0.926	0.738	0.0E+00	0.0E+00
	Trac	1.722	0.781	0.126	0.0E+00	0.0E+00
	Gimap3	1.701	0.790	0.197	0.0E+00	0.0E+00
	AW112010	1.634	0.891	0.489	0.0E+00	0.0E+00
	Ets1	1.568	0.849	0.434	0.0E+00	0.0E+00
	Ms4a6b	1.553	0.803	0.254	0.0E+00	0.0E+00
	Skap1	1.513	0.806	0.163	0.0E+00	0.0E+00
	Lck	1.488	0.779	0.264	0.0E+00	0.0E+00
	Ramp1	1.368	0.783	0.405	0.0E+00	0.0E+00
	Rps2	1.301	0.993	0.889	0.0E+00	0.0E+00
	Nkg7	1.264	0.876	0.521	0.0E+00	0.0E+00
	Ptma	1.233	0.983	0.718	0.0E+00	0.0E+00
	Maf	1.184	0.936	0.701	0.0E+00	0.0E+00
	Thy1	1.172	0.878	0.165	0.0E+00	0.0E+00
	Hspe1	1.096	0.879	0.665	0.0E+00	0.0E+00
	Tst	1.319	0.571	0.602	1.0E-05	1.6E-02
	Pmepa1	1.556	0.563	0.622	5.8E-05	8.7E-02
	Fmo2	1.044	0.413	0.343	2.5E-04	3.8E-01
	Crip2	1.269	0.502	0.560	1.6E-03	1.0E+00
	Igfbp7	1.823	0.413	0.473	5.7E-03	1.0E+00
	Sftpd	1.945	0.489	0.461	8.2E-03	1.0E+00
T cells 2	Ccl5	6.355	0.988	0.505	0.0E+00	0.0E+00
	Nkg7	4.438	0.997	0.532	0.0E+00	0.0E+00
	AW112010	3.298	0.997	0.502	0.0E+00	0.0E+00
	Cd3g	2.927	0.963	0.453	0.0E+00	0.0E+00
	Klrd1	2.649	0.930	0.383	0.0E+00	0.0E+00
	Gimap4	2.407	0.904	0.222	0.0E+00	0.0E+00
	Cxcr6	2.039	0.977	0.308	0.0E+00	0.0E+00
	Ikzf3	1.577	0.956	0.261	0.0E+00	0.0E+00
	Pdcd1	1.413	0.989	0.234	0.0E+00	0.0E+00
	Rgs16	0.578	0.966	0.464	0.0E+00	0.0E+00
	Bcl2	2.127	0.963	0.426	1.1E-305	1.6E-302
	Klre1	1.502	0.905	0.518	5.3E-294	8.0E-291
	Gimap1	2.138	0.918	0.450	1.1E-276	1.6E-273
	Ptprcap	2.054	0.919	0.521	6.8E-265	1.0E-261
	Gzma	3.710	0.885	0.291	3.3E-263	5.0E-260
	Serpinb9	1.165	0.887	0.348	3.6E-245	5.4E-242
	Wls	1.997	0.925	0.525	5.8E-242	8.8E-239
	Ctsw	2.064	0.826	0.206	9.3E-235	1.4E-231
	Gpr171	0.922	0.902	0.568	2.0E-234	3.1E-231
	Camk2n1	0.674	0.893	0.584	6.5E-232	9.8E-229
	Klrb1c	0.994	0.792	0.241	1.3E-217	2.0E-214
	Thy1	1.399	0.805	0.194	2.8E-212	4.2E-209
	Itga1	1.174	0.858	0.540	2.9E-207	4.3E-204
	Lck	1.936	0.843	0.282	9.4E-198	1.4E-194
	Cd3e	1.702	0.850	0.307	4.9E-196	7.4E-193
	Bin1	1.028	0.889	0.559	4.2E-175	6.3E-172
	Rpl3	1.327	0.992	0.710	1.8E-173	2.7E-170
	mt-Nd1	1.057	0.991	0.669	1.2E-168	1.8E-165
	Ctla2a	1.995	0.849	0.746	4.1E-167	6.2E-164
	Gbp4	0.491	0.908	0.599	6.1E-164	9.2E-161
	Skap1	1.419	0.785	0.187	8.8E-160	1.3E-156
	Lgals1	1.245	0.915	0.575	1.1E-159	1.6E-156
	Gimap3	1.887	0.779	0.219	8.9E-157	1.3E-153
	Gpr65	0.821	0.870	0.451	4.5E-153	6.7E-150
	Ets1	1.314	0.838	0.449	9.4E-153	1.4E-149
	Ptma	1.057	0.983	0.728	1.0E-151	1.5E-148
	Il2rb	1.677	0.756	0.242	1.1E-147	1.7E-144
	Crip1	0.729	0.947	0.503	4.0E-140	5.9E-137
	Hspe1	0.981	0.928	0.671	4.3E-139	6.5E-136
	Gzmb	2.047	0.733	0.217	1.6E-136	2.4E-133
	Bcl2a1d	0.761	0.902	0.508	6.0E-129	9.1E-126
	Ly9	0.743	0.798	0.321	9.2E-125	1.4E-121
	Laptm5	0.968	0.994	0.735	1.4E-124	2.2E-121
	Trbc2	2.552	0.763	0.257	3.1E-120	4.7E-117
	Gimap6	1.119	0.771	0.323	5.1E-115	7.7E-112
	Rps2	0.852	0.998	0.893	4.5E-114	6.7E-111
	Trac	1.458	0.734	0.151	8.0E-114	1.2E-110
	AU020206	0.620	0.934	0.698	2.9E-110	4.4E-107
	Irf8	0.532	0.853	0.635	3.3E-106	4.9E-103
	H2afz	0.948	0.944	0.804	2.5E-104	3.7E-101
	Ccnd2	1.530	0.785	0.608	3.8E-104	5.7E-101
	Dut	0.533	0.774	0.448	1.5E-98	2.3E-95
	Emp3	0.746	0.876	0.460	5.1E-97	7.6E-94
	Id2	0.628	0.977	0.778	1.4E-96	2.0E-93
	Ebpl	0.549	0.782	0.407	2.9E-88	4.4E-85
	Ndufa4	0.747	0.879	0.668	4.0E-88	6.0E-85
	Cd2	1.412	0.725	0.421	1.2E-85	1.8E-82
	Ifi47	0.906	0.766	0.648	1.7E-82	2.6E-79
	Klrk1	1.640	0.666	0.100	2.0E-81	3.0E-78
	Serpinb6b	0.741	0.769	0.688	8.2E-73	1.2E-69
	Cx3cr1	0.855	0.716	0.365	3.6E-72	5.4E-69
	Reep5	0.686	0.904	0.713	1.6E-71	2.4E-68
	Pla2g16	0.823	0.780	0.548	3.0E-65	4.5E-62
	Racgap1	0.500	0.689	0.255	1.8E-63	2.7E-60
	Cd7	1.311	0.653	0.123	3.7E-59	5.5E-56
	F2r	1.007	0.699	0.655	1.7E-57	2.5E-54
	Itm2c	0.598	0.789	0.595	2.3E-57	3.5E-54
	Maf	0.484	0.773	0.713	6.1E-56	9.2E-53
	Sh2d1a	1.028	0.637	0.160	4.7E-49	7.0E-46

	Ccl5	1.061	0.893	0.492	0.0E+00	0.0E+00		Cd3d	1.570	0.660	0.399	1.5E-48	2.3E-45
	Pdcd1	1.058	0.965	0.206	0.0E+00	0.0E+00		Nme1	0.638	0.798	0.715	6.0E-44	9.0E-41
	Icos	1.040	0.721	0.224	0.0E+00	0.0E+00		Cd48	1.146	0.658	0.445	9.0E-42	1.3E-38
	Il2rb	0.938	0.822	0.219	0.0E+00	0.0E+00		Pycard	0.597	0.864	0.778	3.7E-39	5.5E-36
	Trdc	0.926	0.888	0.260	0.0E+00	0.0E+00		Zbp1	0.508	0.708	0.633	3.6E-36	5.5E-33
	Ikzf3	0.876	0.895	0.238	0.0E+00	0.0E+00		Itgb7	0.911	0.655	0.528	4.8E-34	7.2E-31
	F2r	0.833	0.807	0.646	0.0E+00	0.0E+00		Gimap7	1.216	0.618	0.234	2.7E-31	4.0E-28
	mt-Nd1	0.778	0.971	0.657	0.0E+00	0.0E+00		Tmem160	0.727	0.687	0.583	2.4E-28	3.7E-25
	Tcrg-C1	0.619	0.895	0.175	0.0E+00	0.0E+00		Phf11b	0.550	0.623	0.316	8.7E-28	1.3E-24
	Cd163l1	0.484	0.811	0.167	0.0E+00	0.0E+00		Dock10	0.734	0.696	0.678	3.1E-27	4.7E-24
	Camk2n1	0.476	0.974	0.567	0.0E+00	0.0E+00		Klra4	1.070	0.347	0.141	2.8E-26	4.2E-23
	Il2ra	0.462	0.861	0.138	0.0E+00	0.0E+00		Kcnq1ot1	0.612	0.692	0.655	1.8E-18	2.6E-15
	Gbp4	0.441	0.879	0.589	0.0E+00	0.0E+00		Nucks1	0.618	0.643	0.535	1.4E-17	2.1E-14
	AU020206	0.440	0.957	0.687	0.0E+00	0.0E+00		Ranbp1	0.579	0.682	0.647	3.9E-15	5.9E-12
	Nrp1	0.439	0.886	0.725	0.0E+00	0.0E+00		Trbc1	1.609	0.582	0.216	9.1E-15	1.4E-11
	Gpr171	0.417	0.782	0.562	3.2E-288	4.8E-285		Osbpl3	0.642	0.631	0.611	1.3E-13	1.9E-10
	S100a4	1.528	0.865	0.488	9.4E-267	1.4E-263		AC149090.1	0.829	0.602	0.458	1.3E-12	2.0E-09
	Crip1	0.519	0.881	0.490	1.0E-230	1.6E-227		Bcl11b	1.186	0.573	0.347	3.4E-12	5.1E-09
	Ctsw	0.610	0.694	0.191	3.5E-222	5.3E-219		Sept9	0.475	0.618	0.475	1.9E-10	2.8E-07
	Slc25a4	0.912	0.791	0.526	7.1E-222	1.1E-218		Il18r1	0.691	0.586	0.426	6.5E-10	9.8E-07
	Lat	0.926	0.715	0.457	1.0E-202	1.6E-199		Il7r	0.709	0.631	0.679	2.1E-09	3.1E-06
	Gimap4	1.294	0.695	0.208	3.3E-200	5.0E-197		S100a4	1.032	0.598	0.508	3.6E-09	5.4E-06
	Tcf7	0.897	0.659	0.050	2.1E-199	3.1E-196		Evl	0.553	0.597	0.346	4.4E-08	6.6E-05
	Gimap6	0.852	0.713	0.309	4.4E-194	6.6E-191		Dok2	0.675	0.563	0.438	3.4E-07	5.0E-04
	Cd28	1.003	0.702	0.529	1.9E-184	2.8E-181		Sms	0.505	0.435	0.441	5.8E-07	8.7E-04
	Bcl11b	1.081	0.686	0.332	1.0E-181	1.6E-178		Ms4a6b	0.880	0.574	0.280	7.1E-07	1.1E-03
	Ebpl	0.434	0.744	0.395	1.2E-177	1.7E-174		Ybx3	0.569	0.449	0.607	4.5E-06	6.7E-03
	Itgb7	1.071	0.709	0.520	5.7E-170	8.5E-167		Cblb	0.518	0.449	0.632	7.0E-06	1.0E-02
	Wls	0.694	0.775	0.518	1.0E-164	1.6E-161		Esyt1	0.697	0.566	0.420	1.5E-05	2.2E-02
	Cd2	1.084	0.694	0.411	6.8E-162	1.0E-158		Sept11	0.805	0.568	0.594	8.0E-05	1.2E-01
	Gpr65	0.404	0.737	0.442	2.0E-150	3.0E-147		Slamf7	0.845	0.534	0.547	8.7E-03	1.0E+00
	4930523C07Rik	0.862	0.693	0.505	1.3E-137	1.9E-134	**Prol.**	Pclaf	2.491	0.958	0.145	0.0E+00	0.0E+00
	Pla2g16	0.610	0.767	0.540	8.1E-130	1.2E-126		Tpx2	1.659	0.979	0.461	0.0E+00	0.0E+00
	Pgls	0.429	0.820	0.627	5.4E-121	8.1E-118		Hmmr	1.416	0.965	0.417	0.0E+00	0.0E+00
	Dut	0.633	0.647	0.443	7.5E-88	1.1E-84		Cks1b	1.929	0.966	0.434	5.1E-307	7.7E-304
	Cd7	0.448	0.374	0.119	7.0E-70	1.1E-66		Ccnb1	1.412	0.897	0.279	9.5E-295	1.4E-291
	Ifi203	0.760	0.642	0.560	2.2E-69	3.3E-66		Spc25	1.049	0.954	0.304	7.3E-293	1.1E-289
	Il18r1	0.468	0.359	0.433	9.1E-69	1.4E-65		Stmn1	2.414	0.965	0.511	2.1E-290	3.1E-287
	Ranbp1	0.564	0.715	0.643	6.1E-68	9.1E-65		Mki67	2.558	0.959	0.570	2.8E-289	4.3E-286
	Mllt3	0.629	0.666	0.631	2.6E-67	3.8E-64		Nusap1	1.629	0.920	0.239	1.2E-271	1.7E-268
	Ar	0.464	0.380	0.208	8.1E-65	1.2E-61		Cdca8	1.719	0.927	0.543	1.2E-265	1.8E-262
	Ccnd2	0.721	0.677	0.608	5.6E-64	8.3E-61		Tuba1b	2.789	0.975	0.597	1.6E-247	2.4E-244
	Tmem176a	0.693	0.737	0.580	1.5E-62	2.3E-59		Cenpe	1.483	0.904	0.409	3.6E-245	5.4E-242
	Igfbp4	0.442	0.371	0.530	4.0E-61	6.0E-58		Racgap1	1.111	0.892	0.252	2.0E-234	3.0E-231
	Hmgn1	0.444	0.702	0.651	8.9E-57	1.3E-53		Ptma	2.106	0.961	0.729	9.1E-234	1.4E-230
	Nucks1	0.698	0.651	0.530	2.2E-56	3.2E-53		Lig1	1.309	0.922	0.604	1.5E-224	2.2E-221
	Ifi27l2a	0.810	0.649	0.527	1.1E-55	1.7E-52		Comt	1.054	0.981	0.624	1.5E-214	2.2E-211
	Nrip1	0.824	0.664	0.612	7.0E-54	1.1E-50		Fn1	1.115	0.950	0.408	2.4E-214	3.6E-211
	Esyt1	0.550	0.636	0.410	6.1E-53	9.1E-50		Mt1	1.467	0.989	0.771	5.7E-214	8.6E-211
	Ifi47	0.471	0.662	0.649	1.9E-50	2.9E-47		Tacc3	1.088	0.885	0.465	6.6E-212	1.0E-208
	Dock10	0.556	0.688	0.678	8.2E-47	1.2E-43		Nucks1	2.033	0.961	0.529	6.2E-211	9.3E-208
	Trbc1	1.908	0.580	0.202	3.3E-44	4.9E-41		H2afz	1.932	0.933	0.805	2.0E-204	3.0E-201
	C1qbp	0.468	0.666	0.664	9.5E-43	1.4E-39		Tagln2	2.069	0.991	0.587	7.3E-196	1.1E-192
	Ms4a4b	0.952	0.551	0.088	2.1E-41	3.2E-38		Snx5	1.077	0.986	0.545	5.5E-194	8.2E-191
	Gm12840	1.196	0.572	0.386	9.3E-39	1.4E-35		Tubb5	2.638	0.927	0.597	1.1E-193	1.6E-190
	Gimap7	0.743	0.566	0.222	1.6E-32	2.4E-29		Hmgn1	1.810	0.970	0.649	2.7E-191	4.0E-188
	Klk8	0.546	0.598	0.493	8.8E-32	1.3E-28		Atad2	1.082	0.929	0.479	9.4E-191	1.4E-187
	Rexo2	0.515	0.636	0.637	1.1E-25	1.6E-22		Ppp1r14b	1.888	0.981	0.660	1.3E-189	1.9E-186
	Zbtb20	0.641	0.604	0.540	1.0E-24	1.5E-21		Lgals1	1.754	0.982	0.574	1.6E-188	2.4E-185
	Evl	0.589	0.582	0.337	5.4E-18	8.2E-15		Slc25a4	1.447	0.961	0.533	1.2E-185	1.8E-182
	Las1l	0.388	0.576	0.490	5.6E-17	8.4E-14		Ccnb2	1.586	0.846	0.228	4.4E-185	6.7E-182
	Kcnq1ot1	0.582	0.619	0.658	8.6E-16	1.3E-12		Hebp1	1.259	0.989	0.644	2.7E-183	4.1E-180
	S1pr1	0.739	0.552	0.507	8.8E-16	1.3E-12		Ezh2	1.288	0.869	0.522	1.3E-180	2.0E-177
	Lef1	0.517	0.517	0.035	3.6E-14	5.4E-11		Crip1	1.624	0.982	0.504	1.2E-176	1.8E-173
	Gpr183	0.598	0.436	0.265	9.7E-11	1.5E-07		Tmem256	1.475	0.968	0.545	1.8E-173	2.7E-170
	Kcnn4	0.510	0.468	0.579	5.0E-10	7.6E-07		Prdx1	1.850	0.996	0.665	5.2E-173	7.7E-170
	Gm8369	0.566	0.443	0.091	1.8E-09	2.8E-06		Selenoh	1.849	0.871	0.469	1.9E-168	2.8E-165
	Tnfsf8	0.669	0.451	0.396	5.5E-09	8.3E-06		Cenpa	1.756	0.867	0.426	3.0E-166	4.4E-163
	Ramp3	0.410	0.540	0.413	1.2E-07	1.8E-04		Cenpx	1.309	0.959	0.664	6.9E-165	1.0E-161
	Ccr2	0.445	0.449	0.261	4.5E-07	6.8E-04		Rexo2	1.263	0.965	0.631	8.8E-164	1.3E-160
	Tmem160	0.367	0.600	0.584	5.6E-07	8.5E-04		Ndufa4	2.100	0.982	0.667	3.8E-158	5.8E-155
	Dapl1	0.839	0.526	0.394	4.6E-06	6.9E-03		Pycard	1.529	0.989	0.776	2.6E-157	4.0E-154
	Cblb	0.388	0.487	0.637	1.4E-04	2.1E-01		Smc4	1.764	0.924	0.614	5.8E-155	8.7E-152
	Odc1	0.426	0.573	0.569	1.2E-03	1.0E+00		Fabp5	1.449	0.993	0.803	1.1E-154	1.7E-151
	Tmem176b	0.675	0.581	0.569	5.8E-03	1.0E+00		Cks2	1.430	0.931	0.464	1.4E-152	2.2E-149

	Igfbp4	0.442	0.371	0.530	4.0E-61	6.0E-58		Racgap1	1.111	0.892	0.252	2.0E-234	3.0E-231
	Hmgn1	0.444	0.702	0.651	8.9E-57	1.3E-53		Ptma	2.106	0.961	0.729	9.1E-234	1.4E-230
	Nucks1	0.698	0.651	0.530	2.2E-56	3.2E-53		Lig1	1.309	0.922	0.604	1.5E-224	2.2E-221
	Ifi27l2a	0.810	0.649	0.527	1.1E-55	1.7E-52		Comt	1.054	0.981	0.624	1.5E-214	2.2E-211
	Nrip1	0.824	0.664	0.612	7.0E-54	1.1E-50		Fn1	1.115	0.950	0.408	2.4E-214	3.6E-211
	Esyt1	0.550	0.636	0.410	6.1E-53	9.1E-50		Mt1	1.467	0.989	0.771	5.7E-214	8.6E-211
	Ifi47	0.471	0.662	0.649	1.9E-50	2.9E-47		Tacc3	1.088	0.885	0.465	6.6E-212	1.0E-208
	Dock10	0.556	0.688	0.678	8.2E-47	1.2E-43		Nucks1	2.033	0.961	0.529	6.2E-211	9.3E-208
	Trbc1	1.908	0.580	0.202	3.3E-44	4.9E-41		H2afz	1.932	0.933	0.805	2.0E-204	3.0E-201
	C1qbp	0.468	0.666	0.664	9.5E-43	1.4E-39		Tagln2	2.069	0.991	0.587	7.3E-196	1.1E-192
	Ms4a4b	0.952	0.551	0.088	2.1E-41	3.2E-38		Snx5	1.077	0.986	0.545	5.5E-194	8.2E-191
	Gm12840	1.196	0.572	0.386	9.3E-39	1.4E-35		Tubb5	2.638	0.927	0.597	1.1E-193	1.6E-190
	Gimap7	0.743	0.566	0.222	1.6E-32	2.4E-29		Hmgn1	1.810	0.970	0.649	2.7E-191	4.0E-188
	Klk8	0.546	0.598	0.493	8.8E-32	1.3E-28		Atad2	1.082	0.929	0.479	9.4E-191	1.4E-187
	Rexo2	0.515	0.636	0.637	1.1E-25	1.6E-22		Ppp1r14b	1.888	0.981	0.660	1.3E-189	1.9E-186
	Zbtb20	0.641	0.604	0.540	1.0E-24	1.5E-21		Lgals1	1.754	0.982	0.574	1.6E-188	2.4E-185
	Evl	0.589	0.582	0.337	5.4E-18	8.2E-15		Slc25a4	1.447	0.961	0.533	1.2E-185	1.8E-182
	Las1l	0.388	0.576	0.490	5.6E-17	8.4E-14		Ccnb2	1.586	0.846	0.228	4.4E-185	6.7E-182
	Kcnq1ot1	0.582	0.619	0.658	8.6E-16	1.3E-12		Hebp1	1.259	0.989	0.644	2.7E-183	4.1E-180
	S1pr1	0.739	0.552	0.507	8.8E-16	1.3E-12		Ezh2	1.288	0.869	0.522	1.3E-180	2.0E-177
	Lef1	0.517	0.517	0.035	3.6E-14	5.4E-11		Crip1	1.624	0.982	0.504	1.2E-176	1.8E-173
	Gpr183	0.598	0.436	0.265	9.7E-11	1.5E-07		Tmem256	1.475	0.968	0.545	1.8E-173	2.7E-170
	Kcnn4	0.510	0.468	0.579	5.0E-10	7.6E-07		Prdx1	1.850	0.996	0.665	5.2E-173	7.7E-170
	Gm8369	0.566	0.443	0.091	1.8E-09	2.8E-06		Selenoh	1.849	0.871	0.469	1.9E-168	2.8E-165
	Tnfsf8	0.669	0.451	0.396	5.5E-09	8.3E-06		Cenpa	1.756	0.867	0.426	3.0E-166	4.4E-163
	Ramp3	0.410	0.540	0.413	1.2E-07	1.8E-04		Cenpx	1.309	0.959	0.664	6.9E-165	1.0E-161
	Ccr2	0.445	0.449	0.261	4.5E-07	6.8E-04		Rexo2	1.263	0.965	0.631	8.8E-164	1.3E-160
	Tmem160	0.367	0.600	0.584	5.6E-07	8.5E-04		Ndufa4	2.100	0.982	0.667	3.8E-158	5.8E-155
	Dapl1	0.839	0.526	0.394	4.6E-06	6.9E-03		Pycard	1.529	0.989	0.776	2.6E-157	4.0E-154
	Cblb	0.388	0.487	0.637	1.4E-04	2.1E-01		Smc4	1.764	0.924	0.614	5.8E-155	8.7E-152
	Odc1	0.426	0.573	0.569	1.2E-03	1.0E+00		Fabp5	1.449	0.993	0.803	1.1E-154	1.7E-151
	Tmem176b	0.675	0.581	0.569	5.8E-03	1.0E+00		Cks2	1.430	0.931	0.464	1.4E-152	2.2E-149
Mac 1	Apoe	3.645	0.999	0.776	0.0E+00	0.0E+00		Nap1l1	1.688	0.954	0.558	1.7E-148	2.5E-145
	Ctss	3.156	1.000	0.646	0.0E+00	0.0E+00		Hspa9	1.285	0.938	0.643	9.9E-148	1.5E-144
	Fn1	3.070	0.961	0.389	0.0E+00	0.0E+00		Nme1	1.906	0.965	0.712	1.0E-146	1.5E-143
	Lyz2	2.912	1.000	0.750	0.0E+00	0.0E+00		Prdx2	1.788	0.940	0.640	2.6E-141	3.9E-138
	Trem2	2.398	0.999	0.563	0.0E+00	0.0E+00		Rpl3	1.645	0.952	0.712	2.0E-140	3.0E-137
	Lgals1	2.386	1.000	0.559	0.0E+00	0.0E+00		Rps2	1.458	0.940	0.894	2.3E-130	3.5E-127
	Spp1	2.356	0.996	0.780	0.0E+00	0.0E+00		Spp1	1.101	0.991	0.788	3.2E-128	4.8E-125
	Mafb	2.251	0.977	0.576	0.0E+00	0.0E+00		Tubb4b	1.816	0.977	0.715	3.8E-128	5.6E-125
	C1qa	2.202	0.980	0.573	0.0E+00	0.0E+00		Cybb	1.037	0.947	0.519	8.9E-128	1.3E-124
	Fabp5	2.165	0.994	0.796	0.0E+00	0.0E+00		Vim	1.633	0.988	0.644	2.4E-125	3.5E-122
	C1qb	2.126	0.982	0.493	0.0E+00	0.0E+00		Mcm7	1.071	0.851	0.556	1.5E-124	2.2E-121
	Psap	2.095	1.000	0.747	0.0E+00	0.0E+00		Ybx3	1.869	0.865	0.599	1.9E-123	2.8E-120
	Ctsl	2.035	0.999	0.840	0.0E+00	0.0E+00		Siva1	1.363	0.931	0.730	6.4E-120	9.6E-117
	C1qc	2.002	0.983	0.633	0.0E+00	0.0E+00		Pgls	1.338	0.950	0.632	5.3E-119	8.0E-116
	Gpnmb	1.975	0.994	0.642	0.0E+00	0.0E+00		Ptms	1.038	0.988	0.620	2.7E-116	4.1E-113
	Vim	1.894	0.998	0.631	0.0E+00	0.0E+00		Fkbp2	1.125	0.931	0.533	4.2E-114	6.3E-111
	Ms4a6c	1.887	0.981	0.393	0.0E+00	0.0E+00		Tyms	1.094	0.796	0.470	1.6E-111	2.5E-108
	Emp3	1.866	0.993	0.440	0.0E+00	0.0E+00		Lamtor4	1.288	0.982	0.702	9.9E-107	1.5E-103
	Plin2	1.859	1.000	0.843	0.0E+00	0.0E+00		Hist1h4d	1.284	0.839	0.676	1.0E-105	1.5E-102
	Cd68	1.847	0.999	0.699	0.0E+00	0.0E+00		Dbi	1.394	0.936	0.644	2.0E-103	3.0E-100
	F13a1	1.817	0.892	0.611	0.0E+00	0.0E+00		Top2a	2.140	0.749	0.304	1.5E-100	2.3E-97
	Lgmn	1.795	0.994	0.615	0.0E+00	0.0E+00		mt-Nd1	1.535	0.881	0.672	2.2E-98	3.2E-95
	Grn	1.771	1.000	0.840	0.0E+00	0.0E+00		Birc5	2.119	0.756	0.487	3.7E-96	5.6E-93
	S100a4	1.755	0.940	0.486	0.0E+00	0.0E+00		Hsp90b1	1.288	0.991	0.786	4.3E-96	6.5E-93
	Lrp1	1.691	0.995	0.503	0.0E+00	0.0E+00		Cdca3	1.395	0.733	0.222	6.4E-91	9.6E-88
	Ms4a7	1.620	0.981	0.421	0.0E+00	0.0E+00		Reep5	1.089	0.966	0.713	1.3E-90	2.0E-87
	mt-Nd1	1.606	0.996	0.658	0.0E+00	0.0E+00		Gm26917	1.427	0.839	0.566	1.8E-88	2.7E-85
	Hexa	1.594	0.999	0.688	0.0E+00	0.0E+00		Aprt	1.160	0.943	0.737	1.0E-83	1.6E-80
	Npc2	1.576	1.000	0.885	0.0E+00	0.0E+00		Gzma	1.044	0.791	0.294	5.1E-75	7.7E-72
	Hexb	1.575	0.998	0.741	0.0E+00	0.0E+00		C1qbp	1.452	0.809	0.661	1.8E-71	2.7E-68
	Crip1	1.546	0.994	0.486	0.0E+00	0.0E+00		Ranbp1	1.666	0.798	0.645	3.8E-71	5.8E-68
	Lamp1	1.530	1.000	0.856	0.0E+00	0.0E+00		Cdc20	1.193	0.713	0.484	2.7E-70	4.1E-67
	Saa3	1.523	0.868	0.613	0.0E+00	0.0E+00		Tmed3	1.101	0.873	0.617	4.5E-69	6.7E-66
	Mgst1	1.502	0.992	0.589	0.0E+00	0.0E+00		Pdia6	1.130	0.973	0.783	2.8E-67	4.2E-64
	Syngr1	1.501	0.994	0.759	0.0E+00	0.0E+00		Cenpf	1.498	0.697	0.197	9.5E-65	1.4E-61
	Ctsz	1.495	1.000	0.786	0.0E+00	0.0E+00		Calr	1.114	0.973	0.770	1.3E-59	1.9E-56
	Ctsb	1.482	1.000	0.942	0.0E+00	0.0E+00		Ramp1	1.043	0.756	0.421	6.4E-56	9.5E-53
	Ccl9	1.476	0.919	0.528	0.0E+00	0.0E+00		Atp5g1	1.539	0.749	0.648	3.7E-50	5.5E-47
	C3ar1	1.475	0.992	0.552	0.0E+00	0.0E+00		Hspd1	1.695	0.731	0.563	1.7E-49	2.6E-46
	Pycard	1.449	0.984	0.769	0.0E+00	0.0E+00		Igkc	2.677	0.216	0.301	7.5E-49	1.1E-45
	Ctsd	1.430	1.000	0.964	0.0E+00	0.0E+00		Igha	1.754	0.694	0.385	6.0E-45	9.0E-42
	Smpdl3a	1.420	0.995	0.611	0.0E+00	0.0E+00		Hspe1	1.292	0.779	0.675	1.7E-44	2.6E-41
	Anxa5	1.419	0.999	0.669	0.0E+00	0.0E+00		Dtymk	1.346	0.694	0.574	2.7E-43	4.1E-40

	Cybb	1.397	0.993	0.501	0.0E+00	0.0E+00
	Ctsa	1.395	0.999	0.689	0.0E+00	0.0E+00
	Fcgr2b	1.362	0.991	0.641	0.0E+00	0.0E+00
	Ms4a6d	1.355	0.957	0.726	0.0E+00	0.0E+00
	Ctsc	1.326	0.970	0.634	0.0E+00	0.0E+00
	Rpl3	1.324	0.999	0.701	0.0E+00	0.0E+00
	Tmem256	1.321	0.978	0.530	0.0E+00	0.0E+00
	Erp29	1.320	0.994	0.701	0.0E+00	0.0E+00
	Lrpap1	1.315	0.993	0.571	0.0E+00	0.0E+00
	Gpx1	1.307	1.000	0.828	0.0E+00	0.0E+00
	Prdx1	1.306	0.998	0.653	0.0E+00	0.0E+00
	Selenop	1.301	0.939	0.505	0.0E+00	0.0E+00
	Ccl6	1.287	0.993	0.618	0.0E+00	0.0E+00
	Itgb5	1.270	0.995	0.664	0.0E+00	0.0E+00
	Snx5	1.244	0.989	0.529	0.0E+00	0.0E+00
	Gusb	1.240	0.981	0.609	0.0E+00	0.0E+00
	Aprt	1.235	0.992	0.727	0.0E+00	0.0E+00
	Dbi	1.213	0.986	0.631	0.0E+00	0.0E+00
	Rps2	1.206	0.998	0.889	0.0E+00	0.0E+00
	Cst3	1.200	0.999	0.812	0.0E+00	0.0E+00
	Atp5g1	1.188	0.996	0.631	0.0E+00	0.0E+00
	Plekho1	1.164	0.955	0.538	0.0E+00	0.0E+00
	Myof	1.160	0.994	0.484	0.0E+00	0.0E+00
	Abca1	1.158	0.989	0.723	0.0E+00	0.0E+00
	Mpeg1	1.121	0.999	0.603	0.0E+00	0.0E+00
	Creg1	1.120	0.999	0.654	0.0E+00	0.0E+00
	Irf8	1.119	0.934	0.623	0.0E+00	0.0E+00
	Cd93	1.117	0.916	0.618	0.0E+00	0.0E+00
	Lamtor4	1.117	0.985	0.692	0.0E+00	0.0E+00
	Pdia6	1.103	0.993	0.775	0.0E+00	0.0E+00
	Fam20c	1.100	0.997	0.755	0.0E+00	0.0E+00
	Hebp1	1.091	0.971	0.633	0.0E+00	0.0E+00
	Hspe1	1.089	0.996	0.660	0.0E+00	0.0E+00
	Fam96a	1.086	0.958	0.547	0.0E+00	0.0E+00
	Tubb5	1.084	0.991	0.582	0.0E+00	0.0E+00
	Sash1	1.076	0.988	0.700	0.0E+00	0.0E+00
	Msr1	1.069	0.965	0.286	0.0E+00	0.0E+00
	Nme1	1.065	0.992	0.702	0.0E+00	0.0E+00
	Fkbp2	1.048	0.993	0.516	0.0E+00	0.0E+00
	Tmem160	1.046	0.970	0.564	0.0E+00	0.0E+00
	Gyg	1.041	0.960	0.639	0.0E+00	0.0E+00
	Gatm	1.037	0.904	0.510	0.0E+00	0.0E+00
	Anxa4	1.008	0.987	0.484	0.0E+00	0.0E+00
	Pgls	1.005	0.988	0.619	0.0E+00	0.0E+00
	Pid1	1.002	0.863	0.576	0.0E+00	0.0E+00
	Ppp1r14b	1.000	0.991	0.648	0.0E+00	0.0E+00
	Ucp2	0.994	0.999	0.719	0.0E+00	0.0E+00
	Aldh2	0.986	0.970	0.496	0.0E+00	0.0E+00
	Tuba1b	0.983	0.991	0.583	0.0E+00	0.0E+00
	Timp2	0.980	0.994	0.767	0.0E+00	0.0E+00
	Tmed3	0.973	0.994	0.602	0.0E+00	0.0E+00
	Zeb2	0.969	0.991	0.611	0.0E+00	0.0E+00
	Sgk1	0.967	0.986	0.632	0.0E+00	0.0E+00
	Lat2	0.960	0.968	0.664	0.0E+00	0.0E+00
	Hal	0.960	0.984	0.673	0.0E+00	0.0E+00
	Ccr2	0.957	0.715	0.248	2.0E-241	3.0E-238
	Ccl2	1.048	0.587	0.454	4.3E-39	6.5E-36
Macs 2	Chil3	4.719	0.975	0.671	0.0E+00	0.0E+00
	Gpnmb	3.826	1.000	0.645	0.0E+00	0.0E+00
	Lpl	3.697	0.989	0.496	0.0E+00	0.0E+00
	Ctsk	3.692	0.959	0.550	0.0E+00	0.0E+00
	Mmp12	3.321	0.870	0.537	0.0E+00	0.0E+00
	Lyz2	3.173	1.000	0.752	0.0E+00	0.0E+00
	Psap	3.172	1.000	0.749	0.0E+00	0.0E+00
	Cybb	2.910	1.000	0.504	0.0E+00	0.0E+00
	Crip1	2.846	0.996	0.490	0.0E+00	0.0E+00
	Atp6v0d2	2.784	0.999	0.677	0.0E+00	0.0E+00
	Spp1	2.744	0.996	0.782	0.0E+00	0.0E+00
	Mfge8	2.720	0.895	0.672	0.0E+00	0.0E+00
	Ctss	2.600	0.999	0.649	0.0E+00	0.0E+00
	Fabp5	2.562	0.999	0.797	0.0E+00	0.0E+00
	Ctsl	2.553	0.996	0.841	0.0E+00	0.0E+00
	Ctsd	2.452	1.000	0.964	0.0E+00	0.0E+00
	Camp	4.266	0.267	0.373	3.4E-41	5.1E-38
	Hist1h2ap	1.712	0.662	0.481	8.0E-37	1.2E-33
	Erp29	1.042	0.758	0.715	5.1E-28	7.7E-25
	Ube2c	1.866	0.621	0.424	1.2E-24	1.7E-21
	Serpinb1a	1.100	0.363	0.542	1.4E-23	2.2E-20
	Ngp	3.416	0.294	0.366	1.9E-22	2.8E-19
	H2afx	1.423	0.598	0.441	1.4E-15	2.1E-12
	Prc1	1.160	0.595	0.429	2.0E-15	2.9E-12
	Hist1h2ae	1.473	0.600	0.599	3.2E-09	4.8E-06
	Hist1h1b	2.008	0.556	0.500	1.6E-06	2.4E-03
	Car2	1.424	0.451	0.501	5.3E-05	7.9E-02
	Smc2	1.419	0.545	0.391	1.3E-04	2.0E-01
	Jchain	1.375	0.566	0.380	9.6E-04	1.0E+00
Neu-5 IFN	Rsad2	3.882	0.893	0.683	2.2E-159	3.2E-156
	Isg15	2.862	0.914	0.683	9.1E-136	1.4E-132
	Ifitm3	2.426	0.937	0.699	9.8E-131	1.5E-127
	Gbp2	3.508	0.883	0.647	3.1E-123	4.6E-120
	Slfn4	3.032	0.848	0.564	3.0E-118	4.5E-115
	Ifi47	2.533	0.858	0.647	4.5E-108	6.7E-105
	Ifit2	1.494	0.827	0.689	1.6E-98	2.5E-95
	Rtp4	2.650	0.820	0.679	1.4E-96	2.1E-93
	Ifit1bl2	1.106	0.794	0.562	1.8E-92	2.6E-89
	Slfn5	2.500	0.787	0.570	5.6E-89	8.5E-86
	Ifit3b	2.020	0.698	0.421	5.4E-66	8.2E-63
	Ccl4	1.652	0.921	0.717	1.5E-61	2.2E-58
	Acod1	1.515	0.764	0.419	5.1E-59	7.7E-56
	Ifit1	2.933	0.693	0.445	1.8E-55	2.7E-52
	Isg20	2.176	0.731	0.572	2.0E-51	3.0E-48
	Cldn1	0.347	0.777	0.616	3.0E-47	4.4E-44
	Fcgr4	1.090	0.812	0.694	1.6E-45	2.3E-42
	Zbp1	1.271	0.789	0.633	5.8E-45	8.7E-42
	Cmpk2	1.335	0.647	0.457	6.9E-42	1.0E-38
	Wfdc17	0.879	0.916	0.778	1.7E-38	2.6E-35
	Oasl1	2.003	0.668	0.582	1.0E-34	1.5E-31
	Hcar2	0.498	0.830	0.679	1.6E-30	2.4E-27
	Gbp5	1.549	0.660	0.546	6.0E-30	9.0E-27
	Ifit3	2.987	0.612	0.399	9.5E-30	1.4E-26
	Gm4316	0.371	0.279	0.493	1.4E-29	2.1E-26
	Gm12840	0.275	0.201	0.399	4.9E-28	7.3E-25
	Retnlg	0.406	0.835	0.628	9.9E-28	1.5E-24
	G0s2	1.012	0.711	0.497	7.3E-27	1.1E-23
	Fyb	0.799	0.835	0.695	1.1E-26	1.6E-23
	Ffar2	0.272	0.701	0.484	2.4E-26	3.6E-23
	Cd274	1.280	0.736	0.593	5.4E-26	8.2E-23
	Bst2	1.457	0.657	0.508	1.2E-23	1.7E-20
	Egr1	0.572	0.756	0.554	1.1E-22	1.7E-19
	Ccl3	0.827	0.799	0.641	1.1E-22	1.7E-19
	Cxcl2	1.001	0.741	0.536	4.1E-22	6.2E-19
	Cxcl10	1.921	0.551	0.311	1.4E-21	2.2E-18
	Ier3	0.726	0.820	0.788	1.7E-21	2.5E-18
	Gm20234	0.309	0.609	0.491	1.1E-18	1.6E-15
	Ly6i	0.652	0.586	0.455	1.5E-18	2.2E-15
	Usp18	1.392	0.604	0.553	2.2E-18	3.4E-15
	Clec4a3	0.263	0.614	0.448	7.7E-17	1.1E-13
	Slpi	0.712	0.797	0.643	1.8E-16	2.6E-13
	Gm5483	0.695	0.728	0.616	2.9E-16	4.3E-13
	Olfm4	0.430	0.635	0.476	1.4E-15	2.1E-12
	Saa3	0.296	0.764	0.624	1.7E-15	2.6E-12
	Asprv1	0.545	0.734	0.588	2.1E-15	3.1E-12
	Gm19951	0.676	0.769	0.685	5.5E-15	8.3E-12
	Ifi202b	0.285	0.739	0.658	5.6E-15	8.4E-12
	Ifitm1	0.593	0.807	0.738	8.3E-15	1.2E-11
	Osgin1	0.663	0.678	0.588	7.4E-14	1.1E-10
	Fgd4	0.355	0.713	0.634	7.6E-14	1.1E-10
	Lcn2	0.607	0.683	0.610	1.0E-11	1.5E-08
	Cst3	0.478	0.858	0.821	2.9E-11	4.3E-08
	Fam20c	0.267	0.858	0.766	2.1E-10	3.2E-07
	Bcl2a1a	0.523	0.398	0.556	5.1E-10	7.6E-07
	Id2	0.498	0.881	0.780	1.8E-09	2.6E-06
	Wfdc21	0.437	0.713	0.653	1.8E-09	2.6E-06
	Il1f9	0.718	0.632	0.560	2.7E-09	4.0E-06
	Laptm5	0.349	0.812	0.739	3.7E-08	5.6E-05
	Id1	0.788	0.688	0.693	5.4E-08	8.1E-05

	Fabp4	2.405	0.976	0.611	0.0E+00	0.0E+00		Csf2rb	0.657	0.721	0.686	8.4E-08	1.3E-04
	Lipa	2.389	0.997	0.513	0.0E+00	0.0E+00		Bcl2a1b	0.643	0.751	0.631	3.8E-07	5.7E-04
	Mgll	2.382	0.973	0.587	0.0E+00	0.0E+00		Ddx60	1.401	0.528	0.488	5.3E-07	8.0E-04
	Trem2	2.379	0.995	0.566	0.0E+00	0.0E+00		Mpeg1	0.362	0.726	0.622	1.2E-06	1.7E-03
	Mpeg1	2.367	0.999	0.606	0.0E+00	0.0E+00		Tnfrsf23	0.333	0.741	0.702	5.0E-06	7.5E-03
	Vim	2.330	0.999	0.634	0.0E+00	0.0E+00		Osm	0.260	0.475	0.334	5.3E-06	8.0E-03
	Sgk1	2.323	0.999	0.634	0.0E+00	0.0E+00		Ifi27l2a	2.007	0.553	0.533	5.5E-06	8.2E-03
	mt-Nd1	2.303	0.998	0.660	0.0E+00	0.0E+00		Cdc42ep3	0.290	0.622	0.527	7.5E-06	1.1E-02
	S100a1	2.291	0.994	0.634	0.0E+00	0.0E+00		Il18bp	0.429	0.508	0.450	1.3E-05	2.0E-02
	Ccl6	2.274	0.994	0.621	0.0E+00	0.0E+00		Irf7	0.399	0.642	0.654	2.9E-05	4.4E-02
	Abcg1	2.256	0.997	0.645	0.0E+00	0.0E+00		Lrg1	0.382	0.668	0.699	2.1E-04	3.1E-01
	Mrc1	2.227	0.894	0.408	0.0E+00	0.0E+00		Cd300c2	0.587	0.657	0.660	2.3E-04	3.4E-01
	Myof	2.219	0.995	0.488	0.0E+00	0.0E+00		Hk2	0.508	0.497	0.587	2.8E-04	4.2E-01
	Selenop	2.137	0.991	0.506	0.0E+00	0.0E+00		Steap4	0.298	0.586	0.487	3.4E-04	5.1E-01
	Pld3	2.132	0.995	0.574	0.0E+00	0.0E+00		Ifi209	0.898	0.563	0.599	4.8E-04	7.3E-01
	Plin2	2.121	0.999	0.844	0.0E+00	0.0E+00		Ly6c2	1.077	0.482	0.398	5.2E-04	7.8E-01
	Apoe	2.006	0.979	0.778	0.0E+00	0.0E+00		Chil1	0.308	0.429	0.495	7.0E-04	1.0E+00
	Anxa5	1.983	0.999	0.671	0.0E+00	0.0E+00		Il18	0.297	0.556	0.516	8.5E-04	1.0E+00
	Cd68	1.963	0.998	0.702	0.0E+00	0.0E+00		Ly6g	0.309	0.497	0.449	1.5E-03	1.0E+00
	Aig1	1.926	0.981	0.665	0.0E+00	0.0E+00		Rgs1	0.948	0.627	0.632	1.9E-03	1.0E+00
	Mgst1	1.906	0.996	0.592	0.0E+00	0.0E+00		Unc93b1	0.563	0.569	0.521	2.0E-03	1.0E+00
	Slc7a2	1.859	0.953	0.593	0.0E+00	0.0E+00		Hist1h1c	0.327	0.497	0.617	2.6E-03	1.0E+00
	Ear2	1.849	0.881	0.305	0.0E+00	0.0E+00		Ifitm6	0.346	0.391	0.472	4.6E-03	1.0E+00
	Sh3bgrl	1.816	0.991	0.540	0.0E+00	0.0E+00	**Eryth.**	Hbb-bs	9.669	1.000	0.782	0.0E+00	0.0E+00
	Lrp1	1.810	0.995	0.507	0.0E+00	0.0E+00		Hba-a1	8.916	1.000	0.499	0.0E+00	0.0E+00
	Hexa	1.807	0.999	0.690	0.0E+00	0.0E+00		Hbb-bt	8.788	0.996	0.481	0.0E+00	0.0E+00
	Gns	1.748	1.000	0.684	0.0E+00	0.0E+00		Hba-a2	8.609	1.000	0.450	0.0E+00	0.0E+00
	Abhd12	1.739	0.990	0.418	0.0E+00	0.0E+00		Bpgm	4.001	0.837	0.481	0.0E+00	0.0E+00
	Ahnak2	1.738	0.981	0.542	0.0E+00	0.0E+00		Alas2	3.365	0.939	0.531	0.0E+00	0.0E+00
	Creg1	1.723	0.999	0.657	0.0E+00	0.0E+00		Snca	2.876	0.949	0.366	0.0E+00	0.0E+00
	Prdx1	1.712	0.996	0.656	0.0E+00	0.0E+00		Fech	2.293	0.957	0.604	0.0E+00	0.0E+00
	Lgals1	1.693	0.991	0.563	0.0E+00	0.0E+00		Fam46c	1.861	0.916	0.610	0.0E+00	0.0E+00
	Lgmn	1.687	0.991	0.618	0.0E+00	0.0E+00		Rsad2	1.161	0.865	0.679	0.0E+00	0.0E+00
	Gstm1	1.679	0.977	0.546	0.0E+00	0.0E+00		Gypa	0.702	0.791	0.028	0.0E+00	0.0E+00
	Trf	1.674	0.974	0.490	0.0E+00	0.0E+00		Slc4a1	0.430	0.640	0.027	0.0E+00	0.0E+00
	Gm26917	1.673	0.905	0.556	0.0E+00	0.0E+00		Prdx2	1.533	0.891	0.636	2.0E-288	3.0E-285
	Gusb	1.658	0.988	0.611	0.0E+00	0.0E+00		Fam213a	0.874	0.916	0.568	2.3E-282	3.5E-279
	Lamp1	1.650	0.999	0.858	0.0E+00	0.0E+00		Isg20	1.050	0.910	0.561	2.0E-245	2.9E-242
	Acp5	1.634	0.995	0.601	0.0E+00	0.0E+00		Ncoa4	0.766	0.907	0.558	3.4E-228	5.0E-225
	Vat1	1.632	0.981	0.642	0.0E+00	0.0E+00		Aldh1a1	0.377	0.748	0.376	5.6E-212	8.4E-209
	F7	1.632	0.925	0.406	0.0E+00	0.0E+00		Car2	0.406	0.781	0.489	6.8E-212	1.0E-208
	Axl	1.612	0.892	0.422	0.0E+00	0.0E+00		Ube2c	0.553	0.642	0.419	4.5E-87	6.8E-84
	Ctsb	1.608	1.000	0.943	0.0E+00	0.0E+00		Gpx1	0.918	0.898	0.834	2.7E-17	4.0E-14
	Ctsz	1.605	1.000	0.787	0.0E+00	0.0E+00	**Macs 3**	Lyz2	3.103	0.994	0.755	0.0E+00	0.0E+00
	Snx5	1.602	0.992	0.532	0.0E+00	0.0E+00		Atp6v0d2	2.835	0.929	0.683	0.0E+00	0.0E+00
	Ctsa	1.599	0.999	0.692	0.0E+00	0.0E+00		Fabp5	2.818	0.976	0.801	0.0E+00	0.0E+00
	Dusp3	1.564	0.986	0.628	0.0E+00	0.0E+00		Fabp4	2.446	0.907	0.618	0.0E+00	0.0E+00
	Cd36	1.561	0.877	0.480	0.0E+00	0.0E+00		Trem2	2.287	0.948	0.573	0.0E+00	0.0E+00
	Myo5a	1.560	0.983	0.491	0.0E+00	0.0E+00		Mmp12	2.260	0.889	0.540	0.0E+00	0.0E+00
	Aplp2	1.550	0.995	0.630	0.0E+00	0.0E+00		Vim	2.236	0.943	0.640	0.0E+00	0.0E+00
	Il11ra1	1.532	0.958	0.470	0.0E+00	0.0E+00		Gpnmb	2.203	0.955	0.651	0.0E+00	0.0E+00
	Kcnq1ot1	1.510	0.945	0.642	0.0E+00	0.0E+00		Ftl1	1.976	1.000	0.956	0.0E+00	0.0E+00
	Sirpa	1.506	0.996	0.609	0.0E+00	0.0E+00		C1qa	1.299	0.907	0.583	0.0E+00	0.0E+00
	Itgax	1.499	0.986	0.527	0.0E+00	0.0E+00		Il11ra1	1.068	0.868	0.479	1.4E-302	2.1E-299
	Anxa4	1.494	0.988	0.487	0.0E+00	0.0E+00		Lgals1	2.459	0.899	0.571	2.8E-293	4.2E-290
	Fstl1	1.486	0.862	0.466	0.0E+00	0.0E+00		C1qb	1.319	0.890	0.505	4.2E-288	6.2E-285
	Dnmt3a	1.473	0.946	0.462	0.0E+00	0.0E+00		Lpl	2.532	0.875	0.506	1.6E-278	2.4E-275
	Cdo1	1.466	0.918	0.461	0.0E+00	0.0E+00		Cdkn2a	0.952	0.852	0.657	1.9E-278	2.9E-275
	Shtn1	1.463	0.978	0.464	0.0E+00	0.0E+00		Pld3	1.832	0.903	0.582	6.5E-275	9.7E-272
	Laptm5	1.462	0.999	0.728	0.0E+00	0.0E+00		Crip1	2.187	0.866	0.500	1.9E-269	2.8E-266
	Grn	1.460	0.996	0.841	0.0E+00	0.0E+00		Serpinb6a	2.298	0.917	0.672	1.5E-268	2.3E-265
	Mertk	1.458	0.955	0.387	0.0E+00	0.0E+00		Spp1	2.531	0.948	0.786	4.3E-264	6.4E-261
	Slc6a6	1.456	0.997	0.490	0.0E+00	0.0E+00		Prdx1	2.470	0.877	0.664	4.4E-258	6.7E-255
	Smpdl3a	1.454	0.996	0.614	0.0E+00	0.0E+00		Sdc3	1.041	0.862	0.567	9.7E-254	1.5E-250
	Il18	1.438	0.916	0.498	0.0E+00	0.0E+00		S100a1	2.732	0.862	0.643	1.9E-248	2.8E-245
	Abcc5	1.434	0.946	0.408	0.0E+00	0.0E+00		Myof	1.428	0.860	0.499	6.7E-247	1.0E-243
	Colgalt1	1.434	0.980	0.501	0.0E+00	0.0E+00		Ctsk	2.393	0.836	0.559	2.3E-238	3.5E-235

	Ucp2	1.423	0.999	0.721	0.0E+00	0.0E+00		Mt2	1.490	0.817	0.645	2.6E-238	3.8E-235
	Serpinb6a	1.419	0.997	0.665	0.0E+00	0.0E+00		Ccl6	2.295	0.913	0.628	1.9E-236	2.9E-233
	Itgb2	1.419	0.996	0.577	0.0E+00	0.0E+00		Cd63	2.069	0.968	0.778	4.8E-228	7.2E-225
	Cd63	1.419	0.999	0.774	0.0E+00	0.0E+00		Apoe	1.530	0.947	0.782	7.2E-227	1.1E-223
	Dbi	1.415	0.987	0.634	0.0E+00	0.0E+00		Chil3	2.328	0.881	0.677	1.7E-224	2.5E-221
	Tgfbr2	1.413	0.988	0.488	0.0E+00	0.0E+00		C1qc	1.093	0.861	0.644	9.6E-215	1.4E-211
	Sdc3	1.412	0.957	0.559	0.0E+00	0.0E+00		Lgmn	1.340	0.917	0.625	6.9E-209	1.0E-205
	Npc2	1.410	1.000	0.886	0.0E+00	0.0E+00		Plin2	1.944	0.957	0.847	9.8E-201	1.5E-197
	Dhrs3	1.394	0.995	0.661	0.0E+00	0.0E+00		Mfge8	2.225	0.887	0.675	2.6E-200	3.9E-197
	Serpine1	1.356	0.860	0.281	0.0E+00	0.0E+00		Gngt2	2.023	0.880	0.639	1.5E-198	2.2E-195
	Syngr1	1.354	0.971	0.762	0.0E+00	0.0E+00		Cd36	1.210	0.816	0.487	1.8E-196	2.6E-193
	Atp13a2	1.353	0.978	0.468	0.0E+00	0.0E+00		Bhlhe41	1.075	0.805	0.561	8.0E-189	1.2E-185
	Tcf7l2	1.342	0.915	0.455	0.0E+00	0.0E+00		Syngr1	1.161	0.875	0.768	9.8E-184	1.5E-180
	Sort1	1.301	0.946	0.559	0.0E+00	0.0E+00		Mt1	2.231	0.865	0.772	4.2E-183	6.3E-180
	Lrpap1	1.294	0.948	0.577	0.0E+00	0.0E+00		Psap	1.901	0.939	0.754	5.6E-181	8.4E-178
	Bhlhe41	1.284	0.943	0.552	0.0E+00	0.0E+00		Comt	1.663	0.818	0.624	8.2E-180	1.2E-176
	AU020206	1.254	0.941	0.692	0.0E+00	0.0E+00		Ucp2	1.750	0.878	0.729	1.1E-168	1.6E-165
Neu-4 classic	Retnlg	4.320	0.993	0.616	0.0E+00	0.0E+00		Ctsz	1.495	0.959	0.791	1.0E-166	1.5E-163
	Ifitm6	3.584	0.992	0.450	0.0E+00	0.0E+00		Vat1	1.214	0.850	0.651	4.9E-166	7.4E-163
	Lcn2	3.566	0.999	0.596	0.0E+00	0.0E+00		Ctss	1.571	0.856	0.658	2.9E-164	4.3E-161
	Wfdc21	3.439	0.999	0.640	0.0E+00	0.0E+00		Rps2	1.322	0.923	0.894	6.8E-152	1.0E-148
	Mmp8	2.882	0.971	0.602	0.0E+00	0.0E+00		Mgll	1.555	0.775	0.599	2.6E-149	3.9E-146
	Wfdc17	2.808	0.997	0.771	0.0E+00	0.0E+00		Lipa	1.354	0.858	0.524	4.6E-147	6.9E-144
	Ifitm1	2.636	0.992	0.728	0.0E+00	0.0E+00		Nme1	1.536	0.864	0.712	2.6E-139	3.8E-136
	Lrg1	2.580	0.992	0.687	0.0E+00	0.0E+00		Npc2	1.668	0.952	0.889	1.9E-138	2.9E-135
	Prok2	2.540	0.960	0.568	0.0E+00	0.0E+00		Cd68	1.715	0.860	0.710	4.7E-137	7.0E-134
	Ly6g	2.372	0.944	0.430	0.0E+00	0.0E+00		Ndufc2	1.120	0.806	0.620	1.0E-130	1.6E-127
	Slpi	1.882	0.978	0.632	0.0E+00	0.0E+00		Ctsd	1.460	0.982	0.965	5.3E-126	8.0E-123
	Ifitm3	1.752	0.989	0.691	0.0E+00	0.0E+00		Chchd10	0.992	0.770	0.640	1.8E-116	2.7E-113
	Stfa2	1.639	0.909	0.508	0.0E+00	0.0E+00		Acp5	1.333	0.859	0.610	1.3E-111	2.0E-108
	Cd177	1.499	0.907	0.482	0.0E+00	0.0E+00		Blvra	1.204	0.765	0.688	3.1E-107	4.6E-104
	Chil1	1.440	0.942	0.477	0.0E+00	0.0E+00		Ckb	1.006	0.730	0.512	4.7E-105	7.1E-102
	Anxa1	1.274	0.997	0.792	0.0E+00	0.0E+00		Lrpap1	1.029	0.784	0.587	1.6E-100	2.4E-97
	Steap4	1.122	0.940	0.470	0.0E+00	0.0E+00		Marco	1.092	0.638	0.382	1.4E-99	2.1E-96
	Ggt1	1.101	0.897	0.480	0.0E+00	0.0E+00		Hebp1	1.673	0.752	0.647	4.2E-98	6.3E-95
	Il1f9	0.835	0.940	0.545	3.3E-294	4.9E-291		Mrc1	1.060	0.678	0.421	4.6E-96	6.8E-93
	Slfn4	0.805	0.912	0.554	3.6E-286	5.4E-283		Creg1	1.335	0.866	0.665	2.1E-95	3.1E-92
	Tgm1	0.511	0.865	0.592	3.6E-260	5.4E-257		Mpeg1	1.104	0.872	0.615	1.0E-91	1.5E-88
	Ngp	1.375	0.786	0.348	1.6E-249	2.3E-246		Rpl3	1.021	0.848	0.712	2.1E-91	3.2E-88
	Gm5483	1.224	0.916	0.606	2.1E-249	3.2E-246		Ear2	1.521	0.627	0.320	7.5E-87	1.1E-83
	Gbp2	0.381	0.899	0.640	3.9E-247	5.9E-244		Gpx1	1.184	0.891	0.835	1.3E-82	2.0E-79
	BC100530	2.269	0.877	0.550	4.7E-247	7.0E-244		Ctsl	1.931	0.937	0.845	3.9E-82	5.8E-79
	Tgfbi	0.991	0.922	0.598	1.6E-246	2.5E-243		Anxa4	1.516	0.722	0.503	2.2E-78	3.2E-75
	Flna	0.907	0.875	0.483	5.7E-215	8.5E-212		Gyg	1.106	0.792	0.651	6.1E-76	9.1E-73
	Csf2rb	0.767	0.972	0.676	1.4E-214	2.1E-211		Akr1b3	1.361	0.704	0.519	2.5E-74	3.7E-71
	Hacd4	1.020	0.822	0.508	3.9E-214	5.8E-211		Abcg1	1.286	0.825	0.655	1.8E-73	2.7E-70
	Ccl6	0.890	0.959	0.624	1.5E-213	2.3E-210		Cybb	1.621	0.701	0.520	1.8E-71	2.7E-68
	Gyg	0.741	0.863	0.647	1.3E-200	2.0E-197		Anxa5	1.578	0.758	0.684	1.8E-70	2.7E-67
	Stfa2l1	1.303	0.835	0.467	2.0E-193	2.9E-190		Il18	1.245	0.662	0.512	9.3E-69	1.4E-65
	Pi16	0.851	0.785	0.460	4.3E-188	6.4E-185		Ftl1-ps1	0.990	0.663	0.422	6.5E-67	9.7E-64
	Tceal9	0.260	0.937	0.666	1.7E-185	2.6E-182		Lamtor4	1.225	0.821	0.703	5.3E-66	7.9E-63
	Id1	0.309	0.894	0.685	8.3E-174	1.2E-170		Mgst1	1.663	0.691	0.607	2.6E-64	4.0E-61
	Syne1	0.622	0.810	0.599	1.2E-162	1.8E-159		Hexa	1.098	0.839	0.699	4.3E-62	6.4E-59
	F630028O10Ri	0.753	0.828	0.534	8.0E-158	1.2E-154		Sh3bgrl	1.604	0.671	0.556	1.4E-58	2.1E-55
	Mgst1	0.476	0.870	0.599	2.7E-148	4.1E-145		Cndp2	1.101	0.673	0.547	2.4E-57	3.5E-54
	Gadd45a	0.597	0.832	0.616	9.7E-141	1.5E-137		Lmna	1.256	0.730	0.630	2.9E-50	4.4E-47
	Tuba1a	0.562	0.780	0.518	2.4E-137	3.7E-134		Gstm1	1.617	0.640	0.563	2.5E-49	3.7E-46
	Napsa	0.305	0.855	0.579	6.0E-121	9.0E-118		Ptms	1.387	0.727	0.623	3.7E-49	5.5E-46
	Adam8	0.628	0.807	0.586	3.7E-118	5.5E-115		Sept9	1.139	0.627	0.473	6.6E-45	9.8E-42
	Ly6c2	0.635	0.708	0.387	1.9E-116	2.9E-113		Lamp1	0.986	0.887	0.863	7.9E-42	1.2E-38
	Arhgap25	0.285	0.808	0.494	8.0E-109	1.2E-105		Nenf	0.948	0.658	0.522	8.2E-42	1.2E-38
	Fgd4	0.382	0.790	0.629	7.6E-99	1.1E-95		Selenop	1.239	0.639	0.523	4.1E-40	6.2E-37
	Lmo4	0.595	0.715	0.404	6.3E-96	9.5E-93		Ctsb	1.179	0.945	0.945	9.1E-39	1.4E-35
	Smpdl3a	0.448	0.826	0.623	7.2E-91	1.1E-87		Dbi	1.285	0.650	0.649	5.4E-32	8.1E-29
	Itgb2	0.339	0.867	0.585	4.4E-86	6.6E-83		Ccl9	1.120	0.623	0.545	1.0E-31	1.5E-28
	Acvrl1	0.628	0.673	0.488	1.1E-76	1.7E-73		Ctsa	0.950	0.810	0.702	4.3E-31	6.5E-28
	Saa3	0.352	0.854	0.617	1.3E-74	2.0E-71		Camk1	1.023	0.632	0.532	6.6E-31	9.9E-28
	Sirpa	0.296	0.858	0.617	5.0E-72	7.5E-69		Hspe1	1.301	0.691	0.676	9.4E-31	1.4E-27
	Olfm4	1.468	0.683	0.470	6.3E-67	9.5E-64		Smpdl3a	0.946	0.721	0.628	2.8E-25	4.3E-22
	Asprv1	0.875	0.706	0.585	2.1E-58	3.2E-55		Pgls	1.000	0.682	0.636	5.1E-23	7.6E-20

	Olfm4	1.468	0.683	0.470	6.3E-67	9.5E-64		Smpdl3a	0.946	0.721	0.628	2.8E-25	4.3E-22
	Asprv1	0.875	0.706	0.585	2.1E-58	3.2E-55		Pgls	1.000	0.682	0.636	5.1E-23	7.6E-20
	Camp	0.968	0.597	0.362	2.9E-50	4.4E-47		Atp5g1	1.239	0.649	0.649	5.3E-21	8.0E-18
	Serpinb1a	0.640	0.616	0.536	9.8E-38	1.5E-34		Trf	0.948	0.589	0.509	6.0E-18	9.0E-15
	Cfp	0.367	0.625	0.445	1.9E-37	2.9E-34		Fam96a	0.940	0.409	0.573	6.5E-15	9.8E-12
	Stfa3	0.514	0.382	0.548	5.2E-34	7.8E-31		Ppp1r14b	1.198	0.602	0.668	1.6E-10	2.4E-07
	Abcd2	0.264	0.621	0.524	2.9E-28	4.3E-25		Rexo2	1.352	0.558	0.640	1.2E-09	1.8E-06
	Dgat2	0.299	0.683	0.628	9.4E-26	1.4E-22		Aig1	1.010	0.561	0.683	5.7E-03	1.0E+00
	Rab27a	0.295	0.545	0.430	4.6E-11	6.8E-08							
	Osm	0.446	0.514	0.328	4.6E-06	7.0E-03							

Supplemental Table 3: GSEA on scRNAseq Populations, related to Figure 4.18A
NES=Normalized Enrichment Score, FDR=False Discovery Rate

		Combo vs aPD1								
		Macs/Dend			Neus			Tumor		
Group	MSigDB Signature Name	NES	FDR q	-Log(q)	NES	FDR q	-Log(q)	NES	FDR q	-Log(q)
DNA Replication and Damage	REACTOME_G1_S_DNA_DAMAGE_CHECKPOINTS.v2022.1.Hs.grp	1.64	0.02	1.65	1.30	0.18	0.74	1.46	0.03	1.57
	REACTOME_ORC1_REMOVAL_FROM_CHROMATIN.v2022.1.Hs.grp	1.51	0.04	1.36	1.64	0.04	1.39	1.49	0.02	1.68
	REACTOME_SWITCHING_OF_ORIGINS_TO_A_POST_REPLICATIVE_STATE.v2022.1.Hs.grp	1.42	0.07	1.15	1.59	0.05	1.33	1.43	0.03	1.46
	REACTOME_CDT1_ASSOCIATION_WITH_THE_CDC6_ORC_ORIGIN_COMPLEX.v2022.1.Hs.grp	1.55	0.03	1.46	1.69	0.04	1.40	1.41	0.04	1.36
	REACTOME_SYNTHESIS_OF_DNA.v2022.1.Hs.grp	1.37	0.10	1.01	1.63	0.04	1.39	1.37	0.06	1.23
	REACTOME_APC_C_MEDIATED_DEGRADATION_OF_CELL_CYCLE_PROTEINS.v2022.1.Hs.grp	1.45	0.06	1.24	1.52	0.07	1.18	1.40	0.05	1.34
Protein and RNA Processing	KEGG_RIBOSOME.v2022.1.Hs.grp	2.56	0.00	4.00	1.61	0.04	1.37	-2.28	0.00	4.00
	REACTOME_EUKARYOTIC_TRANSLATION_ELONGATION.v2022.1.Hs.grp	2.56	0.00	4.00	1.52	0.07	1.17	-2.42	0.00	4.00
	Hs.grp	2.54	0.00	4.00	1.64	0.04	1.39	-2.02	0.00	2.85
	REACTOME_RESPONSE_OF_EIF2AK4_GCN2_TO_AMINO_ACID_DEFICIENCY.v2022.1.Hs.grp	2.41	0.00	4.00	1.36	0.14	0.84	-2.12	0.00	3.34
	REACTOME_EUKARYOTIC_TRANSLATION_INITIATION.v2022.1.Hs.grp	2.40	0.00	4.00	1.25	0.22	0.65	-2.11	0.00	3.37
	REACTOME_INFLUENZA_INFECTION.v2022.1.Hs.grp	2.40	0.00	4.00	1.27	0.21	0.67	-2.19	0.00	3.84
	GOBP_CYTOPLASMIC_TRANSLATION.v2022.1.Hs.grp	2.24	0.00	4.00	1.04	0.45	0.34	-1.94	0.00	2.60
	REACTOME_TRANSLATION.v2022.1.Hs.grp	2.01	0.00	3.05	1.23	0.24	0.61	-1.62	0.02	1.69
	REACTOME_SELENOAMINO_ACID_METABOLISM.v2022.1.Hs.grp	2.38	0.00	4.00	1.51	0.07	1.17	-2.38	0.00	4.00
	REACTOME_CELLULAR_RESPONSE_TO_STARVATION.v2022.1.Hs.grp	2.30	0.00	4.00	1.04	0.45	0.35	-1.80	0.01	2.14
	REACTOME_METABOLISM_OF_AMINO_ACIDS_AND_DERIVATIVES.v2022.1.Hs.grp	1.98	0.00	2.99	1.22	0.25	0.61	-1.56	0.03	1.54
	REACTOME_NONSENSE_MEDIATED_DECAY_NMD.v2022.1.Hs.grp	2.48	0.00	4.00	1.42	0.11	0.96	-2.21	0.00	4.00
	REACTOME_RRNA_PROCESSING.v2022.1.Hs.grp	2.19	0.00	4.00	1.40	0.12	0.91	-2.01	0.00	2.79
Oxidative Phosphorylation	GOBP_AEROBIC_RESPIRATION.v2022.1.Hs.grp	1.77	0.01	2.11	2.53	0.00	4.00	1.63	0.01	2.28
	GOBP_OXIDATIVE_PHOSPHORYLATION.v2022.1.Hs.grp	1.95	0.00	2.80	2.62	0.00	4.00	1.72	0.00	2.67
	GOBP_ATP_SYNTHESIS_COUPLED_ELECTRON_TRANSPORT.v2022.1.Hs.grp	2.02	0.00	3.01	2.64	0.00	4.00	1.62	0.01	2.22
	GOBP_RESPIRATORY_ELECTRON_TRANSPORT_CHAIN.v2022.1.Hs.grp	1.89	0.00	2.60	2.48	0.00	4.00	1.67	0.00	2.42
	REACTOME_RESPIRATORY_ELECTRON_TRANSPORT_ATP_SYNTHESIS_BY_CHEMIOSMOTIC_COUP									
	LING_AND_HEAT_PRODUCTION_BY_UNCOUPLING_PROTEINS.v2022.1.Hs.grp	1.81	0.01	2.27	2.69	0.00	4.00	1.74	0.00	2.77
	GOBP_ATP_BIOSYNTHETIC_PROCESS.v2022.1.Hs.grp	1.76	0.01	2.05	2.08	0.00	3.19	1.66	0.00	2.38
	Hs.grp	1.54	0.04	1.44	2.31	0.00	4.00	1.60	0.01	2.16
	GOBP_ELECTRON_TRANSPORT_CHAIN.v2022.1.Hs.grp	1.59	0.03	1.52	2.30	0.00	4.00	1.72	0.00	2.69
	REACTOME_RESPIRATORY_ELECTRON_TRANSPORT.v2022.1.Hs.grp	1.83	0.00	2.36	2.53	0.00	4.00	1.62	0.01	2.22
	KEGG_OXIDATIVE_PHOSPHORYLATION.v2022.1.Hs.grp	1.85	0.00	2.41	2.31	0.00	4.00	1.69	0.00	2.57
	REACTOME_COMPLEX_I_BIOGENESIS.v2022.1.Hs.grp	1.83	0.00	2.37	2.13	0.00	3.23	1.58	0.01	2.10
Myeloid Migration	GOBP_NEUTROPHIL_MIGRATION.v2022.1.Hs.grp	2.02	0.00	3.03	-0.94	0.81	0.09	1.97	0.00	4.00
	GOBP_MYELOID_LEUKOCYTE_MIGRATION.v2022.1.Hs.grp	1.99	0.00	2.98	-0.95	0.83	0.08	1.84	0.00	3.20
	GOBP_NEUTROPHIL_CHEMOTAXIS.v2022.1.Hs.grp	1.99	0.00	3.00	0.88	0.72	0.14	2.12	0.00	4.00
	GOBP_GRANULOCYTE_MIGRATION.v2022.1.Hs.grp	1.97	0.00	2.99	1.08	0.42	0.38	1.94	0.00	4.00
	GOBP_LEUKOCYTE_CHEMOTAXIS.v2022.1.Hs.grp	1.90	0.00	2.61	-0.94	0.79	0.10	1.73	0.00	2.68
	GOBP_GRANULOCYTE_CHEMOTAXIS.v2022.1.Hs.grp	1.90	0.00	2.59	1.06	0.43	0.37	2.07	0.00	4.00
	GOBP_CELL_CHEMOTAXIS.v2022.1.Hs.grp	1.89	0.00	2.61	1.05	0.44	0.35	1.72	0.00	2.68
	GOBP_LEUKOCYTE_MIGRATION.v2022.1.Hs.grp	1.81	0.01	2.26	-1.04	0.76	0.12	1.68	0.00	2.45
	GOBP_TAXIS.v2022.1.Hs.grp	1.69	0.01	1.85	1.04	0.45	0.34	1.62	0.01	2.22
Myeloid Activation	GOBP_GRANULOCYTE_ACTIVATION.v2022.1.Hs.grp	1.47	0.06	1.26	1.16	0.31	0.50	1.52	0.02	1.79
	GOBP_POSITIVE_REGULATION_OF_MYELOID_CELL_DIFFERENTIATION.v2022.1.Hs.grp	1.53	0.04	1.39	1.03	0.47	0.33	1.49	0.02	1.69
	GOBP_REGULATION_OF_MYELOID_LEUKOCYTE_MEDIATED_IMMUNITY.v2022.1.Hs.grp	0.91	0.64	0.19	-0.80	0.92	0.03	1.48	0.02	1.65
	GOBP_LEUKOCYTE_MEDIATED_CYTOTOXICITY.v2022.1.Hs.grp	1.29	0.15	0.82	-0.85	0.89	0.05	1.88	0.00	3.52
	GOBP_FC_RECEPTOR_SIGNALING_PATHWAY.v2022.1.Hs.grp	1.12	0.33	0.48	-0.99	0.80	0.09	1.39	0.05	1.30
	GOBP_REGULATION_OF_LEUKOCYTE_MEDIATED_CYTOTOXICITY.v2022.1.Hs.grp	1.16	0.28	0.55	-1.03	0.73	0.14	1.72	0.00	2.66
Inflammation	GOBP_RESPONSE_TO_CHEMOKINE.v2022.1.Hs.grp	1.75	0.01	2.02	-1.26	0.38	0.42	1.69	0.00	2.57
	KEGG_CYTOKINE_CYTOKINE_RECEPTOR_INTERACTION.v2022.1.Hs.grp	1.56	0.04	1.46	-1.40	0.24	0.62	1.52	0.02	1.79
	HALLMARK_IL6_JAK_STAT3_SIGNALING.v2022.1.Hs.grp	1.55	0.04	1.45	-1.48	0.17	0.77	1.48	0.02	1.63
	GOBP_POSITIVE_REGULATION_OF_TUMOR_NECROSIS_FACTOR_SUPERFAMILY_CYTOKINE_PRODU									
	CTION.v2022.1.Hs.grp	1.57	0.03	1.47	-1.26	0.37	0.44	1.59	0.01	2.12
	GOBP_NEGATIVE_REGULATION_OF_VIRAL_GENOME_REPLICATION.v2022.1.Hs.grp	1.93	0.00	2.72	1.53	0.06	1.20	1.35	0.07	1.17
	GOBP_TUMOR_NECROSIS_FACTOR_SUPERFAMILY_CYTOKINE_PRODUCTION.v2022.1.Hs.grp	1.81	0.01	2.26	0.97	0.56	0.25	1.56	0.01	1.98
	HALLMARK_TNFA_SIGNALING_VIA_NFKB.v2022.1.Hs.grp	1.61	0.03	1.58	-2.35	0.00	4.00	1.44	0.03	1.49
	REACTOME_INTERFERON_ALPHA_BETA_SIGNALING.v2022.1.Hs.grp	1.96	0.00	2.88	1.87	0.01	2.14	1.58	0.01	2.09
	HALLMARK_INTERFERON_ALPHA_RESPONSE.v2022.1.Hs.grp	2.17	0.00	3.82	1.79	0.02	1.76	1.57	0.01	2.06
	HALLMARK_INTERFERON_GAMMA_RESPONSE.v2022.1.Hs.grp	2.04	0.00	3.09	0.92	0.64	0.19	1.47	0.03	1.60
	GOBP_ACUTE_INFLAMMATORY_RESPONSE.v2022.1.Hs.grp	2.02	0.00	2.99	1.41	0.12	0.93	1.76	0.00	2.79
	HALLMARK_ALLOGRAFT_REJECTION.v2022.1.Hs.grp	1.72	0.01	1.92	-0.92	0.80	0.10	1.59	0.01	2.11
	HALLMARK_INFLAMMATORY_RESPONSE.v2022.1.Hs.grp	1.97	0.00	2.96	-1.51	0.15	0.82	1.49	0.02	1.67

Supplemental Table 3 Continued: GSEA on scRNAseq Populations, related to Figure 4.18A

NES=Normalized Enrichment Score, FDR=False Discovery Rate

		Combo vs GSK								
		Macs/Dend			Neus			Tumor		
Group	MSigDB Signature Name	NES	FDR q	-Log(q)	NES	FDR q	-Log(q)	NES	FDR q	-Log(q)
DNA Replication and Damage	REACTOME_G1_S_DNA_DAMAGE_CHECKPOINTS.v2022.1.Hs.grp	1.72	0.01	2.20	1.09	0.39		1.30	0.12	0.92
	REACTOME_ORC1_REMOVAL_FROM_CHROMATIN.v2022.1.Hs.grp	1.76	0.00	2.38	1.29	0.20	0.69	1.27	0.14	0.84
	REACTOME_SWITCHING_OF_ORIGINS_TO_A_POST_REPLICATIVE_STATE.v2022.1.Hs.grp	1.65	0.01	1.96	1.20	0.26	0.58	1.23	0.18	0.75
	REACTOME_CDT1_ASSOCIATION_WITH_THE_CDC6_ORC_ORIGIN_COMPLEX.v2022.1.Hs.grp	1.76	0.00	2.37	1.30	0.20	0.69	1.21	0.19	0.71
	REACTOME_SYNTHESIS_OF_DNA.v2022.1.Hs.grp	1.62	0.01	1.84	1.18	0.29	0.54	1.20	0.20	0.69
	REACTOME_APC_C_MEDIATED_DEGRADATION_OF_CELL_CYCLE_PROTEINS.v2022.1.Hs.grp	1.66	0.01	2.00	1.22	0.25	0.60	1.20	0.20	0.69
Protein and RNA Processing	KEGG_RIBOSOME.v2022.1.Hs.grp	2.59	0.00	4.00	-1.30	0.31	0.50	-2.15	0.00	3.86
	REACTOME_EUKARYOTIC_TRANSLATION_ELONGATION.v2022.1.Hs.grp	2.61	0.00	4.00	-1.43	0.28	0.55	-2.28	0.00	4.00
	REACTOME_SRP_DEPENDENT_COTRANSLATIONAL_PROTEIN_TARGETING_TO_MEMBRANE.v2022.1.	2.51	0.00	4.00	-1.25	0.33	0.48	-2.12	0.00	3.70
	REACTOME_RESPONSE_OF_EIF2AK4_GCN2_TO_AMINO_ACID_DEFICIENCY.v2022.1.Hs.grp	2.63	0.00	4.00	-1.40	0.33	0.49	-2.27	0.00	4.00
	REACTOME_EUKARYOTIC_TRANSLATION_INITIATION.v2022.1.Hs.grp	2.52	0.00	4.00	-1.38	0.27	0.57	-2.09	0.00	3.48
	REACTOME_INFLUENZA_INFECTION.v2022.1.Hs.grp	2.53	0.00	4.00	-1.40	0.30	0.52	-2.18	0.00	3.76
	GOBP_CYTOPLASMIC_TRANSLATION.v2022.1.Hs.grp	2.41	0.00	4.00	-1.46	0.25	0.60	-2.18	0.00	3.81
	REACTOME_TRANSLATION.v2022.1.Hs.grp	2.29	0.00	4.00	-1.29	0.33	0.48	-2.02	0.00	3.36
	REACTOME_SELENOAMINO_ACID_METABOLISM.v2022.1.Hs.grp	2.56	0.00	4.00	-1.36	0.29	0.54	-2.24	0.00	4.00
	REACTOME_CELLULAR_RESPONSE_TO_STARVATION.v2022.1.Hs.grp	2.39	0.00	4.00	-1.59	0.24	0.61	-2.05	0.00	3.31
	REACTOME_METABOLISM_OF_AMINO_ACIDS_AND_DERIVATIVES.v2022.1.Hs.grp	2.21	0.00	4.00	-1.09	0.54	0.27	-1.66	0.01	1.85
	REACTOME_NONSENSE_MEDIATED_DECAY_NMD.v2022.1.Hs.grp	2.58	0.00	4.00	-1.34	0.32	0.49	-2.14	0.00	3.90
	REACTOME_RRNA_PROCESSING.v2022.1.Hs.grp	2.39	0.00	4.00	-1.38	0.28	0.55	-2.13	0.00	3.67
Oxidative Phosphorylation	GOBP_AEROBIC_RESPIRATION.v2022.1.Hs.grp	2.05	0.00	3.93	1.93	0.09	1.06	1.82	0.00	3.70
	GOBP_OXIDATIVE_PHOSPHORYLATION.v2022.1.Hs.grp	2.14	0.00	4.00	1.90	0.06	1.26	1.92	0.00	3.82
	GOBP_ATP_SYNTHESIS_COUPLED_ELECTRON_TRANSPORT.v2022.1.Hs.grp	2.14	0.00	4.00	1.83	0.06	1.23	1.88	0.00	3.97
	GOBP_RESPIRATORY_ELECTRON_TRANSPORT_CHAIN.v2022.1.Hs.grp	2.06	0.00	3.91	1.81	0.05	1.28	1.88	0.00	3.94
	REACTOME_RESPIRATORY_ELECTRON_TRANSPORT_ATP_SYNTHESIS_BY_CHEMIOSMOTIC_COUP LING_AND_HEAT_PRODUCTION_BY_UNCOUPLING_PROTEINS.v2022.1.Hs.grp	2.07	0.00	3.88	1.78	0.06	1.19	1.96	0.00	4.00
	GOBP_ATP_BIOSYNTHETIC_PROCESS.v2022.1.Hs.grp	2.08	0.00	3.85	1.72	0.06	1.24	1.98	0.00	4.00
	REACTOME_THE_CITRIC_ACID_TCA_CYCLE_AND_RESPIRATORY_ELECTRON_TRANSPORT.v2022.1.	1.96	0.00	3.45	1.72	0.05	1.26	1.87	0.00	4.04
	GOBP_ELECTRON_TRANSPORT_CHAIN.v2022.1.Hs.grp	1.84	0.00	2.70	1.71	0.05	1.26	1.88	0.00	4.19
	REACTOME_RESPIRATORY_ELECTRON_TRANSPORT.v2022.1.Hs.grp	1.95	0.00	3.41	1.70	0.05	1.30	1.91	0.00	4.04
	KEGG_OXIDATIVE_PHOSPHORYLATION.v2022.1.Hs.grp	2.07	0.00	3.87	1.65	0.06	1.21	2.05	0.00	4.00
	REACTOME_COMPLEX_I_BIOGENESIS.v2022.1.Hs.grp	1.85	0.00	2.77	1.58	0.08	1.09	1.80	0.00	3.38
Myeloid Migration	GOBP_NEUTROPHIL_MIGRATION.v2022.1.Hs.grp	1.81	0.00	2.59	1.43	0.14	0.84	1.83	0.00	3.72
	GOBP_MYELOID_LEUKOCYTE_MIGRATION.v2022.1.Hs.grp	1.88	0.00	2.95	1.38	0.17	0.78	1.84	0.00	3.72
	GOBP_NEUTROPHIL_CHEMOTAXIS.v2022.1.Hs.grp	1.84	0.00	2.70	1.26	0.21	0.68	1.75	0.00	3.07
	GOBP_GRANULOCYTE_MIGRATION.v2022.1.Hs.grp	1.89	0.00	2.99	1.54	0.09	1.03	1.75	0.00	3.07
	GOBP_LEUKOCYTE_CHEMOTAXIS.v2022.1.Hs.grp	1.91	0.00	3.14	1.35	0.17	0.76	1.51	0.02	1.72
	GOBP_GRANULOCYTE_CHEMOTAXIS.v2022.1.Hs.grp	1.90	0.00	3.05	1.39	0.16	0.79	1.71	0.00	2.84
	GOBP_CELL_CHEMOTAXIS.v2022.1.Hs.grp	1.98	0.00	3.60	1.58	0.08	1.11	1.64	0.00	2.41
	GOBP_LEUKOCYTE_MIGRATION.v2022.1.Hs.grp	1.80	0.00	2.54	1.43	0.14	0.84	1.68	0.00	2.68
	GOBP_TAXIS.v2022.1.Hs.grp	1.76	0.00	2.38	1.50	0.12	0.91	1.62	0.01	2.29
Myeloid Activation	GOBP_GRANULOCYTE_ACTIVATION.v2022.1.Hs.grp	1.57	0.02	1.66	1.55	0.09	1.03	1.73	0.00	3.01
	GOBP_POSITIVE_REGULATION_OF_MYELOID_CELL_DIFFERENTIATION.v2022.1.Hs.grp	1.29	0.15	0.83	1.08	0.39	0.41	1.76	0.00	3.16
	GOBP_REGULATION_OF_MYELOID_LEUKOCYTE_MEDIATED_IMMUNITY.v2022.1.Hs.grp	1.39	0.08	1.10	1.19	0.28	0.55	1.79	0.00	3.35
	GOBP_LEUKOCYTE_MEDIATED_CYTOTOXICITY.v2022.1.Hs.grp	1.35	0.10	1.00	0.91	0.65	0.19	1.72	0.00	2.95
	GOBP_FC_RECEPTOR_SIGNALING_PATHWAY.v2022.1.Hs.grp	1.39	0.08	1.10	0.94	0.60	0.22	1.77	0.00	3.19
	GOBP_REGULATION_OF_LEUKOCYTE_MEDIATED_CYTOTOXICITY.v2022.1.Hs.grp	1.12	0.31	0.50	-0.69	0.99	0.00	1.79	0.00	3.39
Inflammation	GOBP_RESPONSE_TO_CHEMOKINE.v2022.1.Hs.grp	1.61	0.02	1.82	-0.90	0.79	0.10	1.73	0.00	3.00
	KEGG_CYTOKINE_CYTOKINE_RECEPTOR_INTERACTION.v2022.1.Hs.grp	1.62	0.01	1.83	0.84	0.78	0.11	1.64	0.00	2.37
	HALLMARK_IL6_JAK_STAT3_SIGNALING.v2022.1.Hs.grp	1.67	0.01	2.02	0.66	0.96	0.02	1.50	0.02	1.66
	GOBP_POSITIVE_REGULATION_OF_TUMOR_NECROSIS_FACTOR_SUPERFAMILY_CYTOKINE_PRODU CTION.v2022.1.Hs.grp	1.24	0.18	0.75	-1.12	0.48	0.32	1.89	0.00	4.15
	GOBP_NEGATIVE_REGULATION_OF_VIRAL_GENOME_REPLICATION.v2022.1.Hs.grp	1.52	0.03	1.51	1.66	0.06	1.26	1.83	0.00	3.70
	GOBP_TUMOR_NECROSIS_FACTOR_SUPERFAMILY_CYTOKINE_PRODUCTION.v2022.1.Hs.grp	1.38	0.08	1.09	-0.87	0.83	0.08	1.77	0.00	3.17
	HALLMARK_TNFA_SIGNALING_VIA_NFKB.v2022.1.Hs.grp	1.65	0.01	1.96	-1.33	0.32	0.49	1.38	0.06	1.20
	REACTOME_INTERFERON_ALPHA_BETA_SIGNALING.v2022.1.Hs.grp	1.67	0.01	2.01	1.12	0.35	0.46	1.73	0.00	3.01
	HALLMARK_INTERFERON_ALPHA_RESPONSE.v2022.1.Hs.grp	1.83	0.00	2.69	1.43	0.15	0.84	1.84	0.00	3.74
	HALLMARK_INTERFERON_GAMMA_RESPONSE.v2022.1.Hs.grp	1.98	0.00	3.57	1.30	0.20	0.70	1.78	0.00	3.28
	GOBP_ACUTE_INFLAMMATORY_RESPONSE.v2022.1.Hs.grp	1.85	0.00	2.74	1.68	0.06	1.24	1.71	0.00	2.83
	HALLMARK_ALLOGRAFT_REJECTION.v2022.1.Hs.grp	1.94	0.00	3.33	0.96	0.57	0.24	1.53	0.02	1.78
	HALLMARK_INFLAMMATORY_RESPONSE.v2022.1.Hs.grp	1.82	0.00	2.66	1.07	0.40	0.39	1.71	0.00	2.84

Supplemental Table 5: Genes Highly Expressed in Neutrophil Clusters, Related to Figure 4.18C

Log2FC= fold change between cluster and all others, pct=percentage of cells expressing

Cluster	Gene Symbol	Log2FC	pct.1	pct.2	P value	Adj P value	Cluster	Gene Symbol	Log2FC	pct.1	pct.2	P value	Adj P value
Neu-1	Cst3	2.050	0.929	0.784	0.0E+00	0.0E+00	**Neu-3**	Gadd45b	2.421	0.877	0.664	0.0E+00	0.0E+00
	Gngt2	1.920	0.812	0.557	0.0E+00	0.0E+00		Nceh1	2.367	0.856	0.760	0.0E+00	0.0E+00
	Hexb	1.393	0.794	0.754	0.0E+00	0.0E+00		Gpnmb	2.274	0.781	0.565	0.0E+00	0.0E+00
	Gpx1	1.277	0.869	0.823	0.0E+00	0.0E+00		Psap	2.244	0.852	0.718	0.0E+00	0.0E+00
	Ptgs1	1.126	0.772	0.702	0.0E+00	0.0E+00		Ifrd1	2.039	0.819	0.707	0.0E+00	0.0E+00
	Ms4a6d	0.881	0.805	0.780	0.0E+00	0.0E+00		Hilpda	2.038	0.836	0.799	0.0E+00	0.0E+00
	Gm19951	0.635	0.840	0.837	0.0E+00	0.0E+00		Ccl3	1.982	0.920	0.759	0.0E+00	0.0E+00
	Cenpx	0.430	0.745	0.593	0.0E+00	0.0E+00		Atp6v1c1	1.914	0.857	0.766	0.0E+00	0.0E+00
	Hist1h4d	0.351	0.793	0.747	0.0E+00	0.0E+00		Lamp1	1.832	0.885	0.784	0.0E+00	0.0E+00
	Ranbp1	0.333	0.704	0.546	0.0E+00	0.0E+00		Hcar2	1.829	0.884	0.824	0.0E+00	0.0E+00
	Card11	0.298	0.831	0.810	0.0E+00	0.0E+00		Ctsb	1.789	0.977	0.916	0.0E+00	0.0E+00
	Hist1h1d	0.297	0.697	0.506	0.0E+00	0.0E+00		Cd63	1.786	0.936	0.864	0.0E+00	0.0E+00
	Dmkn	0.263	0.794	0.646	0.0E+00	0.0E+00		Zeb2	1.742	0.829	0.553	0.0E+00	0.0E+00
	Cpt1a	0.256	0.724	0.482	0.0E+00	0.0E+00		Ctsz	1.678	0.936	0.850	0.0E+00	0.0E+00
	H1f0	0.809	0.700	0.554	4.0E-279	5.9E-276		Ftl1	1.590	1.000	0.999	0.0E+00	0.0E+00
	Laptm5	0.807	0.829	0.784	8.0E-255	1.2E-251		F10	1.513	0.863	0.864	0.0E+00	0.0E+00
	Asah1	0.427	0.666	0.444	2.5E-208	3.7E-205		Gas2l3	1.194	0.818	0.737	0.0E+00	0.0E+00
	Atp1a1	1.115	0.779	0.714	3.2E-204	4.8E-201		Dock10	1.193	0.783	0.789	0.0E+00	0.0E+00
	Pmaip1	0.631	0.787	0.697	2.3E-202	3.5E-199		Lhfpl2	1.059	0.784	0.606	0.0E+00	0.0E+00
	Hist1h1e	0.525	0.794	0.723	2.0E-201	2.9E-198		P2rx7	0.743	0.760	0.628	0.0E+00	0.0E+00
	Atp5g1	0.535	0.667	0.503	3.9E-197	5.8E-194		Pdxk	0.707	0.726	0.490	0.0E+00	0.0E+00
	Ltc4s	0.855	0.644	0.562	2.4E-193	3.5E-190		Gstm1	0.948	0.697	0.537	5.0E-285	7.5E-282
	Ptma	1.199	0.760	0.667	4.4E-184	6.5E-181		Tst	0.523	0.688	0.501	9.7E-282	1.5E-278
	Reep5	0.947	0.749	0.636	1.4E-175	2.1E-172		Hexa	1.286	0.839	0.735	4.4E-268	6.5E-265
	Fam96a	0.381	0.589	0.440	2.4E-164	3.7E-161		Atp6v0d2	0.978	0.752	0.684	3.5E-267	5.3E-264
	Cd81	0.475	0.278	0.442	2.2E-155	3.3E-152		Dhfr	0.859	0.789	0.859	3.2E-265	4.7E-262
	Rps2	0.817	0.873	0.819	8.0E-152	1.2E-148		Chka	0.492	0.738	0.529	2.2E-261	3.2E-258
	Chil3	1.278	0.842	0.760	4.3E-130	6.4E-127		Plcxd2	0.704	0.728	0.788	1.7E-250	2.5E-247
	Agap1	0.711	0.586	0.439	4.9E-117	7.3E-114		Fcgr2b	0.662	0.838	0.714	5.9E-241	8.8E-238
	Cd302	0.256	0.296	0.474	2.5E-116	3.8E-113		Gns	1.455	0.782	0.705	7.0E-240	1.1E-236
	Cd300c2	0.778	0.716	0.616	2.5E-111	3.8E-108		Ctsd	0.702	0.987	0.976	1.2E-220	1.8E-217
	Lrp1	0.630	0.529	0.374	2.7E-108	4.0E-105		Atf3	1.518	0.679	0.486	1.4E-214	2.2E-211
	Krt19	0.266	0.659	0.814	1.1E-103	1.7E-100		Npc1	1.184	0.749	0.753	6.1E-211	9.1E-208
	Hebp1	0.441	0.646	0.524	5.1E-103	7.6E-100		Aprt	1.030	0.820	0.695	1.5E-210	2.3E-207
	Ccnd2	0.297	0.487	0.674	3.5E-88	5.2E-85		Cd68	1.480	0.714	0.531	1.7E-208	2.6E-205
	Ssbp4	0.336	0.596	0.543	6.5E-87	9.8E-84		Canx	0.895	0.769	0.640	1.5E-207	2.3E-204
	Tcf4	0.262	0.442	0.288	1.4E-86	2.1E-83		Cd274	1.443	0.725	0.671	2.9E-205	4.3E-202
	Dpep2	0.452	0.652	0.764	1.9E-86	2.8E-83		Plekhm2	1.059	0.785	0.766	4.3E-197	6.4E-194
	Grn	0.508	0.869	0.830	2.0E-84	2.9E-81		Prdx1	1.174	0.673	0.462	6.6E-191	9.9E-188
	Calr	0.613	0.710	0.613	1.3E-82	1.9E-79		Tpp1	1.030	0.716	0.620	1.2E-185	1.8E-182
	B930036N10Ri	0.429	0.642	0.682	1.8E-82	2.7E-79		Naglu	0.956	0.616	0.469	3.1E-165	4.6E-162
	Naaa	0.466	0.655	0.600	1.6E-81	2.4E-78		H2-Eb1	0.929	0.683	0.729	7.5E-150	1.1E-146
	Pgls	0.322	0.607	0.512	2.7E-81	4.0E-78		Dhrs3	0.764	0.674	0.525	6.6E-145	9.9E-142
	Id2	0.400	0.925	0.882	1.7E-75	2.6E-72		Dnmt1	0.341	0.626	0.526	3.8E-137	5.7E-134
	Bcl2a1b	0.796	0.640	0.563	8.2E-75	1.2E-71		Npc2	1.027	0.875	0.886	1.8E-132	2.7E-129
	Ctsa	0.531	0.744	0.686	2.7E-68	4.0E-65		Tmem86a	0.556	0.724	0.748	2.4E-128	3.5E-125
	Manf	0.354	0.814	0.794	6.8E-68	1.0E-64		Gadd45g	1.393	0.634	0.509	5.6E-122	8.4E-119
	Cybb	0.303	0.519	0.409	4.6E-65	6.8E-62		Id2	0.969	0.874	0.904	4.8E-121	7.2E-118
	Gm26917	0.282	0.585	0.474	1.5E-61	2.2E-58		Hpgds	0.522	0.680	0.724	9.2E-119	1.4E-115
	Ndufa4	0.667	0.623	0.564	1.9E-60	2.9E-57		Inhba	0.874	0.622	0.511	6.6E-114	9.9E-111
	Hist1h1c	0.752	0.664	0.572	3.1E-58	4.7E-55		Tcirg1	1.016	0.670	0.594	1.6E-112	2.5E-109
	Bcl2a1a	0.768	0.592	0.516	3.8E-58	5.7E-55		Lgmn	0.951	0.627	0.518	1.4E-111	2.1E-108
	Gm2a	0.892	0.637	0.616	1.3E-56	2.0E-53		Ccnf	0.540	0.662	0.781	5.7E-109	8.6E-106
	Phlda1	0.268	0.391	0.530	1.3E-55	1.9E-52		Creg1	1.377	0.702	0.577	1.2E-106	1.9E-103
	Mt1	0.286	0.750	0.734	4.5E-55	6.8E-52		Myo5a	0.533	0.480	0.319	2.3E-99	3.5E-96
	Hist1h4i	0.880	0.646	0.592	5.1E-54	7.6E-51		Mpeg1	0.803	0.701	0.585	5.7E-99	8.5E-96

	Nap1l1	0.311	0.514	0.434	7.4E-52	1.1E-48		Ccl4	1.163	0.868	0.935	3.7E-95	5.6E-92
	Ccng1	0.519	0.520	0.461	1.5E-51	2.2E-48		Syngr1	0.793	0.721	0.791	7.6E-92	1.1E-88
	Unc93b1	0.566	0.570	0.493	1.8E-51	2.6E-48		Aplp2	0.334	0.718	0.588	7.3E-91	1.1E-87
	Pycard	0.298	0.870	0.846	2.1E-51	3.1E-48		Hmox1	1.205	0.790	0.778	9.1E-85	1.4E-81
	P2ry6	0.379	0.710	0.721	1.9E-50	2.9E-47		Hspa9	0.589	0.651	0.663	2.2E-81	3.4E-78
	Tubb5	0.364	0.356	0.505	2.0E-50	3.0E-47		Hspa5	0.742	0.800	0.740	2.0E-80	2.9E-77
	Tubb4b	0.403	0.662	0.575	5.7E-48	8.6E-45		Dpp7	0.502	0.624	0.692	1.0E-72	1.5E-69
	Pdia6	0.555	0.775	0.771	7.2E-48	1.1E-44		Hsp90b1	0.441	0.736	0.690	3.7E-72	5.5E-69
	Gm20186	0.390	0.404	0.535	4.5E-47	6.7E-44		Rgs1	0.942	0.774	0.774	7.5E-70	1.1E-66
	Ucp2	0.715	0.743	0.739	8.8E-42	1.3E-38		Hk2	0.381	0.466	0.660	4.3E-69	6.4E-66
	Clec12a	0.455	0.481	0.424	1.0E-39	1.6E-36		Sqstm1	0.921	0.608	0.494	1.2E-67	1.8E-64
	Colgalt1	0.261	0.486	0.423	4.1E-39	6.1E-36		Emp1	0.827	0.723	0.773	6.3E-65	9.4E-62
	Cks2	0.955	0.534	0.469	1.2E-36	1.8E-33		Rps2	0.628	0.867	0.830	3.3E-63	4.9E-60
	Rpn1	0.256	0.347	0.457	3.6E-31	5.3E-28		Hspa1b	0.866	0.659	0.604	4.8E-63	7.2E-60
	Id1	0.318	0.832	0.819	1.9E-28	2.8E-25		Fam20c	0.379	0.847	0.869	2.1E-60	3.1E-57
	Fam20c	0.332	0.792	0.904	6.0E-27	9.0E-24		Slc37a2	0.582	0.609	0.576	3.5E-55	5.3E-52
	Ctsc	0.283	0.661	0.629	8.2E-26	1.2E-22		Ctsl	0.651	0.807	0.742	5.6E-54	8.4E-51
	Lamtor4	0.498	0.641	0.610	1.3E-25	2.0E-22		Fabp5	0.488	0.626	0.784	3.1E-49	4.6E-46
	Csf1r	0.363	0.280	0.375	2.1E-25	3.2E-22		Ctsa	0.516	0.748	0.695	6.2E-49	9.3E-46
	Rhoc	0.353	0.529	0.648	1.6E-24	2.4E-21		Hsp90aa1	1.357	0.762	0.791	1.2E-48	1.8E-45
	Cdc42ep3	0.331	0.512	0.462	5.0E-23	7.5E-20		Timp2	1.159	0.724	0.658	9.5E-47	1.4E-43
	Krt18	0.259	0.611	0.616	1.1E-21	1.7E-18		Hal	0.601	0.514	0.776	7.5E-29	1.1E-25
	Rgs1	0.444	0.650	0.843	6.1E-21	9.2E-18		Cldn1	0.594	0.582	0.669	4.4E-28	6.6E-25
	H2afz	0.536	0.744	0.728	1.6E-19	2.5E-16		Jdp2	0.437	0.670	0.653	2.7E-25	4.0E-22
	Rpl3	0.306	0.538	0.517	1.6E-16	2.4E-13		Acod1	0.845	0.548	0.530	8.1E-24	1.2E-20
	Hist1h2ap	0.291	0.508	0.492	1.7E-16	2.5E-13		Slc7a11	0.925	0.565	0.555	1.8E-23	2.7E-20
	Mpeg1	0.501	0.595	0.621	2.6E-16	3.8E-13		Grn	0.382	0.873	0.835	1.8E-21	2.8E-18
	Cfp	0.260	0.543	0.504	1.5E-15	2.2E-12		Vegfa	0.831	0.495	0.452	1.0E-20	1.6E-17
	Tubb6	0.260	0.394	0.341	4.6E-14	7.0E-11		Gm26870	0.478	0.567	0.719	2.0E-19	3.0E-16
	Erp29	0.740	0.600	0.627	1.3E-13	2.0E-10		Gusb	0.335	0.618	0.634	2.3E-19	3.5E-16
	Fyb	0.264	0.751	0.780	2.7E-10	4.0E-07		Cd300c2	0.375	0.675	0.645	4.3E-19	6.5E-16
	Spp1	0.341	0.831	0.843	3.7E-09	5.5E-06		Hspe1	0.432	0.639	0.663	1.4E-15	2.1E-12
	Atad2	0.270	0.495	0.481	4.1E-09	6.2E-06		Slc43a3	0.361	0.577	0.707	1.5E-15	2.3E-12
	Bcl2a1d	0.651	0.380	0.413	7.1E-08	1.1E-04		Abcg1	0.435	0.571	0.559	2.1E-15	3.2E-12
	S100a10	0.397	0.513	0.610	3.7E-07	5.6E-04		Syne1	0.692	0.511	0.667	2.2E-14	3.3E-11
	Ctss	0.529	0.679	0.716	6.8E-07	1.0E-03		Rps6ka2	0.368	0.521	0.558	4.6E-14	6.8E-11
	Apoe	0.328	0.748	0.737	8.0E-06	1.2E-02		Ftl1-ps1	0.479	0.338	0.347	1.7E-11	2.5E-08
	Tnf	0.345	0.327	0.311	8.5E-06	1.3E-02		C3	0.346	0.632	0.634	4.3E-11	6.5E-08
	Gm12840	1.062	0.321	0.302	6.5E-05	9.7E-02		Thbs1	1.191	0.451	0.593	1.1E-09	1.6E-06
	Pou2f2	0.584	0.387	0.411	7.3E-04	1.0E+00		Hbb-bs	0.414	0.804	0.812	3.3E-09	5.0E-06
	Aprt	0.360	0.639	0.770	1.4E-03	1.0E+00		Rpl3	0.505	0.532	0.522	5.9E-09	8.8E-06
	Abca1	0.524	0.768	0.829	4.0E-03	1.0E+00		Acp5	0.601	0.473	0.461	1.5E-03	1.0E+00
	Tgfbi	0.309	0.586	0.654	5.9E-03	1.0E+00		Hspa1a	0.817	0.527	0.564	1.7E-03	1.0E+00
	Acp5	0.644	0.451	0.471	7.0E-03	1.0E+00		Spp1	1.001	0.762	0.862	5.5E-03	1.0E+00
Neu-2	BC100530	1.757	0.815	0.739	0.0E+00	0.0E+00	**Neu-5-IFN**	Isg15	3.959	0.914	0.574	8.6E-166	1.3E-162
	Gm5483	1.712	0.938	0.789	0.0E+00	0.0E+00		Rsad2	3.922	0.893	0.799	5.5E-153	8.3E-150
	Wfdc17	1.379	0.993	0.891	0.0E+00	0.0E+00		Ifi47	2.686	0.858	0.765	3.1E-121	4.7E-118
	Cxcl2	1.173	0.951	0.703	0.0E+00	0.0E+00		Ifitm3	2.227	0.937	0.742	1.4E-114	2.1E-111
	Ifitm1	1.111	0.963	0.776	0.0E+00	0.0E+00		Gbp2	3.371	0.883	0.701	2.0E-112	3.0E-109
	Lrg1	0.856	0.929	0.751	0.0E+00	0.0E+00		Ifit2	1.589	0.827	0.776	2.5E-109	3.8E-106
	Egr1	0.840	0.912	0.633	0.0E+00	0.0E+00		Rtp4	2.640	0.820	0.711	1.3E-94	1.9E-91
	Retnlg	0.817	0.960	0.812	0.0E+00	0.0E+00		Slfn4	2.454	0.848	0.736	8.9E-90	1.3E-86
	Wfdc21	0.764	0.945	0.788	0.0E+00	0.0E+00		Slfn5	2.495	0.787	0.619	1.1E-87	1.7E-84
	Ccl6	0.733	0.910	0.693	0.0E+00	0.0E+00		Ifit1bl2	0.982	0.794	0.613	2.2E-77	3.3E-74
	Lcn2	0.710	0.911	0.736	0.0E+00	0.0E+00		Isg20	2.415	0.731	0.518	3.4E-64	5.1E-61
	Cxcl3	0.666	0.840	0.353	0.0E+00	0.0E+00		Ifit1	3.118	0.693	0.425	1.5E-61	2.2E-58
	Tceal9	0.526	0.888	0.729	0.0E+00	0.0E+00		Zbp1	1.428	0.789	0.729	2.5E-60	3.7E-57
	Slfn4	0.469	0.942	0.649	0.0E+00	0.0E+00		Ifi202b	0.654	0.739	0.617	3.0E-57	4.5E-54
	Id1	0.277	0.915	0.784	4.8E-284	7.2E-281		Ifit3b	2.094	0.698	0.535	7.2E-57	1.1E-53
	Slpi	0.579	0.904	0.662	4.9E-284	7.3E-281		Oasl1	2.280	0.668	0.414	6.9E-56	1.0E-52
	Dgat2	0.449	0.795	0.605	5.1E-282	7.6E-279		Ifit3	3.099	0.612	0.263	4.7E-39	7.0E-36
	Adam8	1.014	0.729	0.463	8.4E-262	1.3E-258		Cldn1	0.258	0.777	0.646	1.1E-38	1.6E-35
	Prok2	0.277	0.790	0.700	4.3E-239	6.4E-236		Bst2	1.698	0.657	0.525	6.1E-38	9.1E-35
	Vim	0.636	0.831	0.556	1.3E-219	2.0E-216		Ctss	1.414	0.764	0.701	7.1E-37	1.1E-33
	G0s2	0.703	0.819	0.568	3.6E-170	5.3E-167		Fcgr4	0.876	0.812	0.699	1.1E-32	1.6E-29
	Glrx	0.709	0.678	0.390	5.3E-170	7.9E-167		Cmpk2	1.332	0.647	0.692	9.6E-30	1.4E-26

	F630028O10Rik	0.557	0.798	0.542	6.6E-167	9.8E-164
	Ier3	0.594	0.972	0.826	5.5E-157	8.2E-154
	Steap4	0.560	0.732	0.674	8.3E-127	1.2E-123
	Gadd45a	0.551	0.731	0.616	2.4E-122	3.6E-119
	Stfa2l1	1.367	0.682	0.553	2.0E-118	3.0E-115
	Csf2rb	0.259	0.921	0.714	1.3E-114	1.9E-111
	Stfa2	0.989	0.680	0.704	2.8E-87	4.2E-84
	Il1f9	0.250	0.718	0.540	2.8E-75	4.3E-72
	Asprv1	0.555	0.707	0.722	3.9E-33	5.8E-30
	Saa3	0.387	0.748	0.691	3.2E-27	4.7E-24
	Tacstd2	0.305	0.584	0.468	3.7E-24	5.5E-21
	Osm	0.506	0.460	0.331	1.0E-09	1.6E-06
	Hacd4	0.294	0.496	0.406	4.6E-03	1.0E+00
Neu-4-classic	Retnlg	3.329	0.993	0.845	0.0E+00	0.0E+00
	Ifitm6	3.306	0.992	0.478	0.0E+00	0.0E+00
	Lcn2	2.827	0.999	0.771	0.0E+00	0.0E+00
	Wfdc21	2.632	0.999	0.822	0.0E+00	0.0E+00
	Mmp8	2.622	0.971	0.633	0.0E+00	0.0E+00
	Ly6g	2.187	0.944	0.567	0.0E+00	0.0E+00
	Anxa1	2.167	0.997	0.716	0.0E+00	0.0E+00
	Prok2	2.127	0.960	0.707	0.0E+00	0.0E+00
	Lrg1	1.793	0.992	0.789	0.0E+00	0.0E+00
	Ifitm3	1.588	0.989	0.726	0.0E+00	0.0E+00
	Cd177	1.349	0.907	0.656	0.0E+00	0.0E+00
	Ggt1	1.045	0.897	0.603	0.0E+00	0.0E+00
	Glul	0.436	0.853	0.387	0.0E+00	0.0E+00
	Gyg	0.996	0.863	0.596	8.3E-285	1.2E-281
	Wfdc17	1.832	0.997	0.916	2.1E-279	3.1E-276
	Chil1	0.973	0.942	0.592	8.9E-269	1.3E-265
	Steap4	0.716	0.940	0.670	1.5E-254	2.2E-251
	Stfa2	1.185	0.909	0.678	2.8E-254	4.2E-251
	Tgm1	0.493	0.865	0.635	2.0E-252	3.0E-249
	Mgst1	0.981	0.870	0.580	2.4E-243	3.6E-240
	Flna	0.955	0.875	0.433	4.9E-242	7.4E-239
	Ngp	1.645	0.786	0.355	7.6E-234	1.1E-230
	Slpi	1.162	0.978	0.715	2.2E-232	3.3E-229
	Hacd4	1.004	0.822	0.400	5.4E-230	8.1E-227
	Ifitm1	1.769	0.992	0.819	1.3E-203	2.0E-200
	Ccl6	1.106	0.959	0.742	2.3E-188	3.5E-185
	Smpdl3a	0.852	0.826	0.558	3.0E-187	4.5E-184
	Tuba1a	0.578	0.780	0.474	1.3E-175	1.9E-172
	Vim	0.919	0.966	0.611	2.8E-175	4.1E-172
	Syne1	0.469	0.810	0.615	7.0E-163	1.1E-159
	Tgfbi	0.673	0.922	0.604	6.7E-159	1.0E-155
	Glrx	0.596	0.853	0.445	1.3E-157	2.0E-154
	Tacstd2	0.565	0.812	0.476	1.1E-141	1.7E-138
	Pi16	0.611	0.785	0.543	5.7E-120	8.6E-117
	Lyz2	0.426	0.978	0.755	2.3E-116	3.4E-113
	Lmo4	0.573	0.715	0.315	5.2E-112	7.9E-109
	Ly6c2	0.617	0.708	0.439	1.4E-109	2.1E-106
	BC100530	1.364	0.877	0.752	3.0E-94	4.5E-91
	Aldh2	0.324	0.698	0.433	2.9E-86	4.3E-83
	Stfa2l1	0.440	0.835	0.571	5.3E-68	7.9E-65
	Ceacam1	0.277	0.709	0.530	2.0E-64	3.0E-61
	Plac8	0.327	0.668	0.476	5.6E-64	8.4E-61
	Acvrl1	0.598	0.673	0.666	1.5E-62	2.3E-59
	Camp	1.496	0.597	0.402	1.9E-49	2.9E-46
	Serpinb1a	0.774	0.616	0.519	1.8E-45	2.7E-42
	Abcd2	0.289	0.621	0.535	1.2E-40	1.8E-37
	Stfa3	0.395	0.382	0.646	1.5E-34	2.3E-31
	Sept9	0.260	0.546	0.375	1.8E-28	2.7E-25
	Olfm4	0.922	0.683	0.609	5.7E-22	8.6E-19
	Asprv1	0.255	0.706	0.718	2.2E-13	3.3E-10
	C130026I21Rik	0.253	0.399	0.417	2.3E-11	3.5E-08
	Clec4a3	0.377	0.614	0.450	1.1E-28	1.6E-25
	Acod1	0.910	0.764	0.528	9.0E-26	1.3E-22
	Il18	0.463	0.556	0.366	4.8E-23	7.2E-20
	Fxyd3	0.255	0.571	0.443	7.7E-23	1.2E-19
	Irf7	1.505	0.642	0.564	5.3E-21	7.9E-18
	Il18bp	0.433	0.508	0.318	7.1E-20	1.1E-16
	Cxcl10	1.827	0.551	0.388	8.9E-20	1.3E-16
	Lair1	0.305	0.609	0.516	8.0E-19	1.2E-15
	Gm4316	0.443	0.279	0.343	1.0E-17	1.5E-14
	Npc2	0.571	0.904	0.883	1.2E-17	1.9E-14
	Gbp5	1.547	0.660	0.801	1.3E-17	1.9E-14
	AW112010	0.469	0.520	0.370	1.3E-17	1.9E-14
	Cd274	0.977	0.736	0.682	3.9E-16	5.9E-13
	Hes1	0.375	0.358	0.549	4.7E-16	7.0E-13
	Ifi207	0.258	0.655	0.691	6.5E-15	9.7E-12
	Usp18	1.418	0.604	0.700	7.7E-15	1.2E-11
	Abcg1	0.446	0.701	0.558	1.4E-13	2.2E-10
	Fyb	0.553	0.835	0.768	1.2E-12	1.8E-09
	Bcl2a1b	0.420	0.751	0.586	9.3E-11	1.4E-07
	Cxcl9	0.426	0.736	0.737	1.9E-08	2.8E-05
	Ifi27l2a	2.036	0.553	0.506	1.4E-07	2.1E-04
	Cybb	0.284	0.546	0.446	3.7E-07	5.5E-04
	Ly6i	0.647	0.586	0.648	9.8E-07	1.5E-03
	Plac8	1.572	0.533	0.491	1.0E-06	1.6E-03
	Mpeg1	0.339	0.726	0.608	2.2E-06	3.4E-03
	Emp3	0.292	0.447	0.314	2.4E-06	3.5E-03
	Gm20234	0.310	0.609	0.679	2.7E-06	4.1E-03
	Cst3	0.308	0.858	0.835	9.4E-06	1.4E-02
	Ddx60	1.381	0.528	0.576	2.6E-05	3.9E-02
	Ifi209	1.094	0.563	0.675	6.0E-05	9.0E-02
	Unc93b1	0.390	0.569	0.519	6.2E-05	9.3E-02
	Hba-a1	0.963	0.429	0.553	1.2E-04	1.7E-01
	Lyz2	0.310	0.838	0.771	1.9E-03	1.0E+00
	Ccl4	0.628	0.921	0.920	2.1E-03	1.0E+00
	Ly6c2	1.048	0.482	0.460	3.0E-03	1.0E+00

REFERENCES

1. Siegel, R.L., et al., *Cancer statistics, 2023.* CA Cancer J Clin, 2023. 73(1): p. 17-48.
2. Brainson, C.F., et al., *Description of a Lung Cancer Hotspot: Disparities in Lung Cancer Histology, Incidence, and Survival in Kentucky and Appalachian Kentucky.* Clin Lung Cancer, 2021. 22(6): p. e911-e920.
3. Christian, W.J., et al., *Exploring geographic variation in lung cancer incidence in Kentucky using a spatial scan statistic: elevated risk in the Appalachian coal-mining region.* Public Health Rep, 2011. 126(6): p. 789-96.
4. Christian, W.J., et al., *Spatiotemporal Analysis of Lung Cancer Histological Types in Kentucky, 1995-2014.* Cancer Control, 2019. 26(1): p. 1073274819845873.
5. Unrine, J.M., et al., *A case-control study of trace-element status and lung cancer in Appalachian Kentucky.* PLoS One, 2019. 14(2): p. e0212340.
6. Rudin, C.M., et al., *Small-cell lung cancer.* Nat Rev Dis Primers, 2021. 7(1): p. 3.
7. Thai, A.A., et al., *Lung cancer.* Lancet, 2021. 398(10299): p. 535-554.
8. Chen, Z., et al., *Non-small-cell lung cancers: a heterogeneous set of diseases.* Nat Rev Cancer, 2014. 14(8): p. 535-46.
9. Thai, A.A., et al., *Lung cancer.* The Lancet, 2021. 398(10299): p. 535-554.
10. Ramalingam, S.S., et al., *Overall Survival with Osimertinib in Untreated, EGFR-Mutated Advanced NSCLC.* N Engl J Med, 2020. 382(1): p. 41-50.
11. Juric, D., et al., *Phosphatidylinositol 3-Kinase alpha-Selective Inhibition With Alpelisib (BYL719) in PIK3CA-Altered Solid Tumors: Results From the First-in-Human Study.* J Clin Oncol, 2018. 36(13): p. 1291-1299.
12. Nakajima, E.C., et al., *FDA Approval Summary: Sotorasib for KRAS G12C-Mutated Metastatic NSCLC.* Clin Cancer Res, 2022. 28(8): p. 1482-1486.
13. Campbell, J.D., et al., *Distinct patterns of somatic genome alterations in lung adenocarcinomas and squamous cell carcinomas.* Nat Genet, 2016. 48(6): p. 607-16.
14. Sauer, B., *Inducible gene targeting in mice using the Cre/lox system.* Methods, 1998. 14(4): p. 381-92.
15. DuPage, M., A.L. Dooley, and T. Jacks, *Conditional mouse lung cancer models using adenoviral or lentiviral delivery of Cre recombinase.* Nat Protoc, 2009. 4(7): p. 1064-72.
16. Ji, H., et al., *LKB1 modulates lung cancer differentiation and metastasis.* Nature, 2007. 448(7155): p. 807-10.
17. Jackson, E.L., et al., *The differential effects of mutant p53 alleles on advanced murine lung cancer.* Cancer Res, 2005. 65(22): p. 10280-8.
18. Chen, F., et al., *EZH2 inhibition confers PIK3CA-driven lung tumors enhanced sensitivity to PI3K inhibition.* Cancer Lett, 2022. 524: p. 151-160.
19. Chen, F., et al., *Cellular Origins of EGFR-Driven Lung Cancer Cells Determine Sensitivity to Therapy.* Adv Sci (Weinh), 2021. 8(22): p. e2101999.
20. Xu, C., et al., *Loss of Lkb1 and Pten leads to lung squamous cell carcinoma with elevated PD-L1 expression.* Cancer Cell, 2014. 25(5): p. 590-604.
21. Mollaoglu, G., et al., *The Lineage-Defining Transcription Factors SOX2 and NKX2-1 Determine Lung Cancer Cell Fate and Shape the Tumor Immune Microenvironment.* Immunity, 2018. 49(4): p. 764-779 e9.
22. Ferone, G., et al., *SOX2 Is the Determining Oncogenic Switch in Promoting Lung Squamous Cell Carcinoma from Different Cells of Origin.* Cancer Cell, 2016. 30(4): p. 519-532.

23. Bracken, A.P. and K. Helin, *Polycomb group proteins: navigators of lineage pathways led astray in cancer.* Nat Rev Cancer, 2009. 9(11): p. 773-84.
24. Zhang, H., et al., *Oncogenic Deregulation of EZH2 as an Opportunity for Targeted Therapy in Lung Cancer.* Cancer Discov, 2016. 6(9): p. 1006-21.
25. Ennishi, D., et al., *Molecular and Genetic Characterization of MHC Deficiency Identifies EZH2 as Therapeutic Target for Enhancing Immune Recognition.* Cancer Discov, 2019. 9(4): p. 546-563.
26. Dubois, S., et al., *Immunohistochemical and genomic profiles of diffuse large B-cell lymphomas: implications for targeted EZH2 inhibitor therapy?* Oncotarget, 2015. 6(18): p. 16712-24.
27. Gargiulo, G., E. Citterio, and M. Serresi, *Polycomb and lung cancer: When the dosage makes the (kind of) poison.* Mol Cell Oncol, 2016. 3(3): p. e1152345.
28. Chen, F., et al., *Polycomb deficiency drives a FOXP2-high aggressive state targetable by epigenetic inhibitors.* Nat Commun, 2023. 14(1): p. 336.
29. Zhang, H., et al., *Lkb1 inactivation drives lung cancer lineage switching governed by Polycomb Repressive Complex 2.* Nat Commun, 2017. 8: p. 14922.
30. Chen, Z., et al., *Non-small-cell lung cancers: a heterogeneous set of diseases (vol 14, pg 535, 2014).* Nature Reviews Cancer, 2015. 15(4).
31. Ping, Q., et al., *Cancer-associated fibroblasts: overview, progress, challenges, and directions.* Cancer Gene Ther, 2021. 28(9): p. 984-999.
32. Galon, J. and D. Bruni, *Tumor Immunology and Tumor Evolution: Intertwined Histories.* Immunity, 2020. 52(1): p. 55-81.
33. Hiam-Galvez, K.J., B.M. Allen, and M.H. Spitzer, *Systemic immunity in cancer.* Nat Rev Cancer, 2021. 21(6): p. 345-359.
34. De Kleer, I., et al., *Ontogeny of myeloid cells.* Front Immunol, 2014. 5: p. 423.
35. Klebanoff, S.J., *Myeloperoxidase: friend and foe.* J Leukoc Biol, 2005. 77(5): p. 598-625.
36. Mantovani, A., et al., *Neutrophils in the activation and regulation of innate and adaptive immunity.* Nat Rev Immunol, 2011. 11(8): p. 519-531.
37. Murdoch, C., et al., *The role of myeloid cells in the promotion of tumour angiogenesis.* Nat Rev Cancer, 2008. 8(8): p. 618-31.
38. Pillay, J., et al., *Immune suppression by neutrophils and granulocytic myeloid-derived suppressor cells: similarities and differences.* Cell Mol Life Sci, 2013. 70(20): p. 3813-27.
39. Murray, P.J., *Macrophage Polarization.* Annu Rev Physiol, 2017. 79: p. 541-566.
40. Schupp, J., et al., *Targeting myeloid cells in the tumor sustaining microenvironment.* Cell Immunol, 2019. 343: p. 103713.
41. Canton, J., *Macropinocytosis: New Insights Into Its Underappreciated Role in Innate Immune Cell Surveillance.* Front Immunol, 2018. 9: p. 2286.
42. Fridlender, Z.G., et al., *Polarization of Tumor-Associated Neutrophil Phenotype by TGFb: "N1" versus "N2" TAN.* Cancer Cell, 2009. 16(3): p. 183-194.
43. Yunna, C., et al., *Macrophage M1/M2 polarization.* Eur J Pharmacol, 2020. 877: p. 173090.
44. Jaillon, S., et al., *Neutrophil diversity and plasticity in tumour progression and therapy.* Nat Rev Cancer, 2020. 20(9): p. 485-503.
45. Nagarsheth, N., M.S. Wicha, and W. Zou, *Chemokines in the cancer microenvironment and their relevance in cancer immunotherapy.* Nat Rev Immunol, 2017. 17(9): p. 559-572.
46. Nagarsheth, N., et al., *PRC2 Epigenetically Silences Th1-Type Chemokines to Suppress Effector T-Cell Trafficking in Colon Cancer.* Cancer Res, 2016. 76(2): p. 275-82.

47. Zilionis, R., et al., *Single-Cell Transcriptomics of Human and Mouse Lung Cancers Reveals Conserved Myeloid Populations across Individuals and Species.* Immunity, 2019. 50(5): p. 1317-1334.e10.
48. Tang, K.H., et al., *Combined Inhibition of SHP2 and CXCR1/2 Promotes Antitumor T-cell Response in NSCLC.* Cancer Discovery, 2022. 12(1): p. 47-61.
49. Zhang, N. and M.J. Bevan, *CD8(+) T cells: foot soldiers of the immune system.* Immunity, 2011. 35(2): p. 161-8.
50. Zou, W., *Regulatory T cells, tumour immunity and immunotherapy.* Nat Rev Immunol, 2006. 6(4): p. 295-307.
51. Wan, Y.Y. and R.A. Flavell, *How diverse--CD4 effector T cells and their functions.* J Mol Cell Biol, 2009. 1(1): p. 20-36.
52. Lee, H.E., et al., *Increased Plasma Cells and Decreased B-cells in Tumor Infiltrating Lymphocytes are Associated with Worse Survival in Lung Adenocarcinomas.* J Clin Cell Immunol, 2020. 11(1).
53. Chen, L. and D.B. Flies, *Molecular mechanisms of T cell co-stimulation and co-inhibition.* Nat Rev Immunol, 2013. 13(4): p. 227-42.
54. Wieczorek, M., et al., *Major Histocompatibility Complex (MHC) Class I and MHC Class II Proteins: Conformational Plasticity in Antigen Presentation.* Front Immunol, 2017. 8: p. 292.
55. Shenoy, A.T., et al., *Antigen presentation by lung epithelial cells directs CD4(+) T(RM) cell function and regulates barrier immunity.* Nat Commun, 2021. 12(1): p. 5834.
56. Hasegawa, K., et al., *Fraction of MHCII and EpCAM expression characterizes distal lung epithelial cells for alveolar type 2 cell isolation.* Respir Res, 2017. 18(1): p. 150.
57. van den Elsen, P.J., et al., *Regulation of MHC class I and II gene transcription: differences and similarities.* Immunogenetics, 1998. 48(3): p. 208-21.
58. Abualrous, E.T., J. Sticht, and C. Freund, *Major histocompatibility complex (MHC) class I and class II proteins: impact of polymorphism on antigen presentation.* Curr Opin Immunol, 2021. 70: p. 95-104.
59. Mollaoglu, G., et al., *The Lineage-Defining Transcription Factors SOX2 and NKX2-1 Determine Lung Cancer Cell Fate and Shape the Tumor Immune Microenvironment.* Immunity, 2018. 49(4): p. 764-779.e9.
60. Xu, C., et al., *Loss of Lkb1 and Pten Leads to Lung Squamous Cell Carcinoma with Elevated PD-L1 Expression.* Cancer Cell, 2014. 25(5): p. 590-604.
61. Kargl, J., et al., *Neutrophils dominate the immune cell composition in non-small cell lung cancer.* Nature Communications, 2017. 8: p. 14381.
62. Cupp, M.A., et al., *Neutrophil to lymphocyte ratio and cancer prognosis: an umbrella review of systematic reviews and meta-analyses of observational studies.* BMC Med, 2020. 18(1): p. 360.
63. Johnson, D.B., et al., *Melanoma-specific MHC-II expression represents a tumour-autonomous phenotype and predicts response to anti-PD-1/PD-L1 therapy.* Nat Commun, 2016. 7: p. 10582.
64. Garcia-Diaz, A., et al., *Interferon Receptor Signaling Pathways Regulating PD-L1 and PD-L2 Expression.* Cell Reports, 2017. 19(6): p. 1189-1201.
65. Burr, M.L., et al., *An Evolutionarily Conserved Function of Polycomb Silences the MHC Class I Antigen Presentation Pathway and Enables Immune Evasion in Cancer.* Cancer Cell, 2019. 36(4): p. 385-401 e8.
66. Ribas, A. and J.D. Wolchok, *Cancer immunotherapy using checkpoint blockade.* Science, 2018. 359(6382): p. 1350-1355.

67. He, X. and C. Xu, *Immune checkpoint signaling and cancer immunotherapy.* Cell Res, 2020. 30(8): p. 660-669.
68. Horn, L., et al., *Nivolumab Versus Docetaxel in Previously Treated Patients With Advanced Non-Small-Cell Lung Cancer: Two-Year Outcomes From Two Randomized, Open-Label, Phase III Trials (CheckMate 017 and CheckMate 057).* J Clin Oncol, 2017. 35(35): p. 3924-3933.
69. Borghaei, H., et al., *Five-Year Outcomes From the Randomized, Phase III Trials CheckMate 017 and 057: Nivolumab Versus Docetaxel in Previously Treated Non-Small-Cell Lung Cancer.* J Clin Oncol, 2021. 39(7): p. 723-733.
70. Aguilar, E.J., et al., *Outcomes to first-line pembrolizumab in patients with non-small-cell lung cancer and very high PD-L1 expression.* Ann Oncol, 2019. 30(10): p. 1653-1659.
71. Palmeri, M., et al., *Real-world application of tumor mutational burden-high (TMB-high) and microsatellite instability (MSI) confirms their utility as immunotherapy biomarkers.* ESMO Open, 2022. 7(1): p. 100336.
72. Xie, N., et al., *Neoantigens: promising targets for cancer therapy.* Signal Transduct Target Ther, 2023. 8(1): p. 9.
73. Paz-Ares, L., et al., *A Randomized, Placebo-Controlled Trial of Pembrolizumab Plus Chemotherapy in Patients With Metastatic Squamous NSCLC: Protocol-Specified Final Analysis of KEYNOTE-407.* J Thorac Oncol, 2020. 15(10): p. 1657-1669.
74. DuPage, M., et al., *The chromatin-modifying enzyme Ezh2 is critical for the maintenance of regulatory T cell identity after activation.* Immunity, 2015. 42(2): p. 227-238.
75. Wang, D., et al., *Targeting EZH2 Reprograms Intratumoral Regulatory T Cells to Enhance Cancer Immunity.* Cell Rep, 2018. 23(11): p. 3262-3274.
76. Goswami, S., et al., *Modulation of EZH2 expression in T cells improves efficacy of anti-CTLA-4 therapy.* J Clin Invest, 2018. 128(9): p. 3813-3818.
77. Hoy, S.M., *Tazemetostat: First Approval.* Drugs, 2020. 80(5): p. 513-521.
78. Jackson, E.L., et al., *The Differential Effects of Mutant p53 Alleles on Advanced Murine Lung Cancer.* Cancer Research, 2005. 65(22): p. 10280-10288.
79. Chen, F., et al., *Polycomb deficiency drives a FOXP2-high aggressive state targetable by epigenetic inhibitors.* Nature Communications, 2023. 14(1): p. 336.
80. Zhang, H., et al., *Lkb1 inactivation drives lung cancer lineage switching governed by Polycomb Repressive Complex 2.* Nature communications, 2017. 8: p. 14922-14922.
81. Han, X., et al., *Transdifferentiation of lung adenocarcinoma in mice with Lkb1 deficiency to squamous cell carcinoma.* Nat Commun, 2014. 5.
82. Sachs, N., et al., *Long-term expanding human airway organoids for disease modeling.* The EMBO Journal, 2019. 38(4): p. e100300.
83. McLean, C.Y., et al., *GREAT improves functional interpretation of cis-regulatory regions.* Nature Biotechnology, 2010. 28(5): p. 495-501.
84. Stuart, T., et al., *Comprehensive Integration of Single-Cell Data.* Cell, 2019. 177(7): p. 1888-1902 e21.
85. McInnes, L., et al., *UMAP: Uniform Manifold Approximation and Projection.* Journal of Open Source Software, 2018. 3(29): p. 1.
86. Finak, G., et al., *MAST: a flexible statistical framework for assessing transcriptional changes and characterizing heterogeneity in single-cell RNA sequencing data.* Genome Biol, 2015. 16: p. 278.
87. Bolger, A.M., M. Lohse, and B. Usadel, *Trimmomatic: a flexible trimmer for Illumina sequence data.* Bioinformatics, 2014. 30(15): p. 2114-20.

88. Li, B. and C.N. Dewey, *RSEM: accurate transcript quantification from RNA-Seq data with or without a reference genome.* BMC Bioinformatics, 2011. 12: p. 323.
89. Robinson, M.D., D.J. McCarthy, and G.K. Smyth, *edgeR: a Bioconductor package for differential expression analysis of digital gene expression data.* Bioinformatics, 2010. 26(1): p. 139-40.
90. Herbst, R.S., D. Morgensztern, and C. Boshoff, *The biology and management of non-small cell lung cancer.* Nature, 2018. 553(7689): p. 446-454.
91. Chen, Z., et al., *Non-small-cell lung cancers: a heterogeneous set of diseases.* Nat Rev Cancer, 2014. 14(8): p. 535-546.
92. Stankovic, B., et al., *Immune Cell Composition in Human Non-small Cell Lung Cancer.* Front Immunol, 2018. 9: p. 3101.
93. Kadota, K., et al., *Prognostic Impact of Immune Microenvironment in Lung Squamous Cell Carcinoma.* Journal of Thoracic Oncology, 2015. 10(9): p. 1301-1310.
94. Wang, C., et al., *The heterogeneous immune landscape between lung adenocarcinoma and squamous carcinoma revealed by single-cell RNA sequencing.* Signal Transduction and Targeted Therapy, 2022. 7(1): p. 289.
95. Koppensteiner, L., et al., *Cancer Associated Fibroblasts - An Impediment to Effective Anti-Cancer T Cell Immunity.* Front Immunol, 2022. 13: p. 887380.
96. Baker, A.T., et al., *Cancer-Associated Fibroblasts and T Cells: From Mechanisms to Outcomes.* J Immunol, 2021. 206(2): p. 310-320.
97. Aarts, C.E.M., et al., *Activated neutrophils exert myeloid-derived suppressor cell activity damaging T cells beyond repair.* Blood Adv, 2019. 3(22): p. 3562-3574.
98. Rodriguez, P.C., et al., *Arginase I production in the tumor microenvironment by mature myeloid cells inhibits T-cell receptor expression and antigen-specific T-cell responses.* Cancer Res, 2004. 64(16): p. 5839-49.
99. Jin, J., et al., *Association of the neutrophil to lymphocyte ratio and clinical outcomes in patients with lung cancer receiving immunotherapy: a meta-analysis.* BMJ Open, 2020. 10(6): p. e035031.
100. Campbell, J.D., et al., *Distinct patterns of somatic genome alterations in lung adenocarcinomas and squamous cell carcinomas.* Nat Genet, 2016. 48(6): p. 607-616.
101. Wang, D.-H., et al., *Progression of EGFR-Mutant Lung Adenocarcinoma is Driven By Alveolar Macrophages.* Clinical Cancer Research, 2017. 23(3): p. 778-788.
102. Koyama, S., et al., *STK11/LKB1 Deficiency Promotes Neutrophil Recruitment and Proinflammatory Cytokine Production to Suppress T-cell Activity in the Lung Tumor Microenvironment.* Cancer Research, 2016. 76(5): p. 999-1008.
103. Pfirschke, C., et al., *Tumor-Promoting Ly-6G(+) SiglecF(high) Cells Are Mature and Long-Lived Neutrophils.* Cell Rep, 2020. 32(12): p. 108164.
104. Nagaraj, A.S., et al., *Cell of Origin Links Histotype Spectrum to Immune Microenvironment Diversity in Non-small-Cell Lung Cancer Driven by Mutant Kras and Loss of Lkb1.* Cell Reports, 2017. 18(3): p. 673-684.
105. Moffitt, J.R., E. Lundberg, and H. Heyn, *The emerging landscape of spatial profiling technologies.* Nat Rev Genet, 2022. 23(12): p. 741-759.
106. Li, R., et al., *Characterization of the Tumor Immune Microenvironment in Lung Squamous Cell Carcinoma Using Imaging Mass Cytometry.* Front Oncol, 2021. 11: p. 620989.
107. van Maldegem, F., et al., *Characterisation of tumour microenvironment remodelling following oncogene inhibition in preclinical studies with imaging mass cytometry.* Nature Communications, 2021. 12(1): p. 5906.

108. Jackson, E.L., et al., *Analysis of lung tumor initiation and progression using conditional expression of oncogenic K-ras.* Genes & Development, 2001. 15(24): p. 3243-3248.
109. Ji, H., et al., *LKB1 modulates lung cancer differentiation and metastasis.* Nature, 2007. 448(7155): p. 807-810.
110. Socinski, M.A., et al., *Clinicopathologic Features of Advanced Squamous NSCLC.* J Thorac Oncol, 2016. 11(9): p. 1411-22.
111. Luo, W., et al., *Immunotherapy in non-small cell lung cancer: rationale, recent advances and future perspectives.* Precision Clinical Medicine, 2021. 4(4): p. 258-270.
112. Borghaei, H., L. Paz-Ares, and L. Horn, *Nivolumab versus docetaxel in advanced nonsquamous non-small-cell lung cancer.* N Engl J Med, 2015. 373.
113. Bracken, A.P. and K. Helin, *Polycomb group proteins: navigators of lineage pathways led astray in cancer.* Nature Reviews Cancer, 2009. 9: p. 773.
114. Italiano, A., et al., *Tazemetostat, an EZH2 inhibitor, in relapsed or refractory B-cell non-Hodgkin lymphoma and advanced solid tumours: a first-in-human, open-label, phase 1 study.* The Lancet Oncology, 2018. 19(5): p. 649-659.
115. McCabe, M.T., et al., *EZH2 inhibition as a therapeutic strategy for lymphoma with EZH2-activating mutations.* Nature, 2012. 492(7427): p. 108-112.
116. Kargl, J., et al., *Neutrophil content predicts lymphocyte depletion and anti-PD1 treatment failure in NSCLC.* JCI Insight, 2019. 4(24).
117. Piunti, A., et al., *Immune activation is essential for the antitumor activity of EZH2 inhibition in urothelial carcinoma.* 2022. 8(40): p. eabo8043.
118. Zhou, L., et al., *Targeting EZH2 Enhances Antigen Presentation, Antitumor Immunity, and Circumvents Anti-PD-1 Resistance in Head and Neck Cancer.* Clin Cancer Res, 2020. 26(1): p. 290-300.
119. Burr, M.L., et al., *An Evolutionarily Conserved Function of Polycomb Silences the MHC Class I Antigen Presentation Pathway and Enables Immune Evasion in Cancer.* Cancer Cell, 2019. 36(4): p. 385-401.e8.
120. Zingg, D., et al., *The Histone Methyltransferase Ezh2 Controls Mechanisms of Adaptive Resistance to Tumor Immunotherapy.* Cell Reports, 2017. 20(4): p. 854-867.
121. Tian, R., et al., *ALOX15 as a suppressor of inflammation and cancer: Lost in the link.* Prostaglandins & Other Lipid Mediators, 2017. 132: p. 77-83.
122. Zhang, J. and N. Veeramachaneni, *Targeting interleukin-1β and inflammation in lung cancer.* Biomark Res, 2022. 10(1): p. 5.
123. Kargl, J., et al., *Neutrophils dominate the immune cell composition in non-small cell lung cancer.* Nat Commun, 2017. 8: p. 14381.
124. Kurebayashi, Y., et al., *Comprehensive Immune Profiling of Lung Adenocarcinomas Reveals Four Immunosubtypes with Plasma Cell Subtype a Negative Indicator.* Cancer Immunol Res, 2016. 4(3): p. 234-47.
125. Colling, R., et al., *Artificial intelligence in digital pathology: a roadmap to routine use in clinical practice.* J Pathol, 2019. 249(2): p. 143-150.
126. Acs, B. and J. Hartman, *Next generation pathology: artificial intelligence enhances histopathology practice.* J Pathol, 2020. 250(1): p. 7-8.

VITA

EDUCATION

University of Kentucky, Lexington, KY

August 2017 – Present

Degree: Doctor of Philosophy

Discipline: Toxicology and Cancer Biology

University of Louisiana at Lafayette, Lafayette, LA

August 2005 – December 2016 Degree: Bachelor of Science

Major: Biology

Concentration: Microbiology Minor: Chemistry

AWARDS

2014 & 2016 President's List

2015 Dean's List

2020 – 2022 Department of Toxicology and Cancer Biology T32

RESEARCH EXPERIENCE

University of Louisiana at Lafayette May 2015 – May 2017

Department of Biology, Advisor: Dr. Don Ennis

Virulence mechanisms of Mycobacterium marinum in Japanese Medaka.

University of Kentucky July 2017 – August 2017

Department of Molecular and Cellular Biochemistry, Advisor: Dr. Kathleen O'Connor

Integrin signaling of the integrin α6β4 and its role in breast cancer metastasis.

University of Kentucky August 2017 - October 2017

Department of Microbiology, Immunology & Molecular Genetics, Advisor: Dr. Erin Garcia

Investigated contact dependent inhibition in Burkholderia species.

University of Kentucky October 2017 – December 2017

Department of Molecular and Cellular Biochemistry, Advisor: Dr. Tianyan Gao

Studied the role of the phosphatase PTPRF in colorectal cancer metastasis.

University of Kentucky January 2018 – March 2018

Department of Microbiology, Immunology & Molecular Genetics, Advisor: Dr. Brian Stevenson

Molecular genetics of Borrelia burgdorferi.

University of Kentucky March 2018 – Present

Department of Toxicology and Cancer Biology, Advisor: Dr. Christine Fillmore Brainson

Elucidating the role of EZH2 in antigen presentation to increase efficacy anti-PD-1 immunotherapy in lung squamous cell carcinoma.

PUBLICATIONS

Das, S., Pettersson, F., Behra, P. R., Mallick, A., Cheramie, M., Shirreff, L., DuCote, T…Kirsebom, L. (2018). Extensive genomic diversity among Mycobacterium marinum strains revealed by whole genome sequencing. (Scientific Reports) 8(1) 1-15 .

Behra, P. R. K., Das, S., Pettersson, B. F., Shirreff, L., DuCote, T., Jacobsson, K. G., ... & Kirsebom, L. A. (2019). Extended insight into the Mycobacterium chelonae-abscessus complex through whole genome sequencing of Mycobacterium salmoniphilum outbreak and Mycobacterium salmoniphilum-like strains. Scientific reports, 9(1), 1-15.

Myers-Morales, T., Sim, M. M., DuCote, T. J., & Garcia, E. C. (2021). Burkholderia multivorans requires species-specific GltJK for entry of a contact-dependent growth inhibition system protein. Molecular Microbiology, 116(3), 957-973.

Chen, F., Liu, J., Song, X., DuCote, T. J., Byrd, A. L., Wang, C., & Brainson, C. F. (2022). EZH2 inhibition confers PIK3CA-driven lung tumors enhanced sensitivity to PI3K inhibition. Cancer Letters, 524, 151-160.

Chen, F., Byrd, A. L, Liu, J., Flight, R.M., DuCote, T.J., Naughton, K.J., Song, X., Edgin, A.R., Lukyanchuk, A., Dixon, D., Gosser C.M., Esoe D.P., Jayswal, R.D., Orkin, S.H., Moseley, H.N.B., Wang, C., Brainson, C.F. (2023). Polycomb Deficiency Drives a FOXP2-high Aggressive State Targetable by Epigenetic Inhibitors. Nature Communications, Jan 20;14(1):336.

Byrd, A.L., Qu, X., Lukyanchuk, A., Liu, J., Chen, F., Naughton, K.J., DuCote, T.J., Song, X., Zhao Y., Edgin, A.R., Wang, C., Liu, J., Brainson C.F. (2022)/ Dysregulated Polycomb Repressive Complex 2 contributes to chronic obstructive pulmonary disease by rewiring stem cell fate. Stem Cell Reports, Dec 6;S2213-6711(22)00542-2.

DuCote, T.J., Naughton, K.J., Skaggs, E., Bocklage, T.J., Allison, D.B., Brainson, C.F. Using artificial intelligence to identify tumor heterogeneity in non-small cell lung cancers. Laboratory Investigations. (in revision)

DuCote, T.J., Song, X., Naughton, K.J., Chen, F., Plaugher, D., Childress, A., Edgin, A.R., Qu, X., Liu, J., Liu, J., Li, F., Wong, K.K., Brainson, C.F. EZH2 inhibition promotes tumor immunogenicity in lung squamous cell carcinoma. (in preparation)

PRESENTATIONS

DuCote, T., Brainson, C.F., Song, X., Impact of EZH2 inhibitor on the tumor microenvironment of lung squamous cell carcinoma. Poster presented at: AACR Tumor Immunology and Immunotherapy; 2018 Nov. 27- 29; Miami, FL.

DuCote, T., Brainson, C.F., Song, X., Targeting squamous lung tumor heterogeneity with EZH2 inhibition to improve immunotherapy responses. Poster presented at: AACR Annual Meeting; 2019 Mar. 29th- Apr. 3rd; Atlanta, GA.

DuCote, T., Brainson, C.F., Song, X., Targeting squamous lung tumor heterogeneity with EZH2 inhibition to improve immunotherapy responses. Poster presented at: University of Kentucky Markey Cancer Center Research Day; 2019 May 7th; Lexington, KY.

DuCote, T., Brainson, C.F., Defining the Role of EZH2 in the Tumor Immune-microenvironment of Squamous Lung Cancer.Poster presented at: Cancer Biology Training Consortium (CABTRAC); 2021 October 25th, Nashville, T

DuCote, T., Song, X., Qu, X., Liu, J., Wong, K.K., Brainson, C.F., Defining the Role of EZH2 in the Tumor Immune-microenvironment. Poster presented at: AACR-JCA Translating Knowledge into Practice; 2022 December 14th, Maui, HI

OUTREACH

2018-2020	Fayette County Public Schools Science Fair Judge
2018-2020	Morton Middle School Science Fair Judge
2018-2019	Biobonanza Science Workshop for Children
2018	Girls Engineering, Mathematics and Science (GEMS) Symposium
2019-2021	Appalachian Careers in Training Oncology (ACTION) – Instructor
2021-2022	Markey STRONG - Instructor

2016 – 2017 University of Louisiana at Lafayette
Region VI Science and Engineering Fair

MEMBERSHIPS and SERVICE

2015 – 2016 American Society for Microbiology

2017 – 2020 Biomedical Graduate Student Organization

2018-2020 Outreach and Social Committees

Treasurer (2019 – 2020)

Outreach Committee Chair (2019 – 2020)

2018 –current American Association for Cancer Research

2019 –current Students Embracing Equity in Medical Sciences

2019 – 2021 Markey Cancer Center Molecular Tumor Board

2019 – 2021 Department of Toxicology and Cancer Biology Rules Committee

2020 –current Department of Toxicology and Cancer Biology Diversity, Equity, and Inclusion Committee

2020 – 2022 Markey Cancer Center Diversity, Equity, and Inclusion Committee